Optical Theory for the Advancement of Polarization Lidar

by

Matthew Hayman

B.S., University of Colorado, 2005

A thesis submitted to the

Faculty of the Graduate School of the

University of Colorado in partial fulfillment

of the requirements for the degree of

Doctor of Philosophy

Department of Electrical, Computer and Energy Enginneering

2011

This thesis entitled:
Optical Theory for the Advancement of Polarization Lidar
written by Matthew Hayman
has been approved for the Department of Electrical, Computer and Energy Enginneering

Jeffrey P. Thayer

Prof. Kelvin Wagner

Date

The final copy of this thesis has been examined by the signatories, and we find that both the content and the form meet acceptable presentation standards of scholarly work in the above mentioned discipline.

Hayman, Matthew (Ph.D., Electrical Engineering)

Optical Theory for the Advancement of Polarization Lidar

Thesis directed by Prof. Jeffrey P. Thayer

Determining the polarization scattering properties of sub micron size particles through interactions with transmitted visible wavelengths requires the capability to detect polarization effects on the order of a few percent. Such small changes in polarization can easily be overwhelmed by the intrinsic polarization properties of the instrument. When applied to lidar remote sensing techniques, additional environmental factors such as background noise, volume content of scatterers, range to the scatterer, and temporal variations in the scattering medium result in degradation of the instrument's SNR. Furthermore, present approaches in polarization lidar are often confined to measurement of a single parameter which provides no distinction between different scattering and instrumentation polarization effects, limiting the possible interpretations of the measurement. These issues confronting polarization lidar present an opportunity for a novel approach in lidar polarization studies through expansion of system measurement capabilities and instrument performance optimization.

In this work, I discuss how these issues may be addressed for the purpose of characterizing particle properties through polarization. Instrument retarding effects are reduced by measuring the optical system Mueller matrix and implementing a hardware polarization compensator which also increases system SNR by improving rejection of the polarized sky noise component. We have developed a calibration algorithm which then removes residual phase shifts, depolarization, and misalignment of transmitter and receiver polarization planes. These techniques are proven through polarization data from atmospheric aerosols measured by the ARCLITE lidar in Kangerlussuaq, Greenland.

By recognizing that a scattering phase matrix is a Mueller matrix, the polarization effects of scatterers can be decomposed and described as a combination of depolarizers, retarders, and

diattenuators. Furthermore, the polarization attributes of scatterers can be directly related to their physical properties. While it is well established that depolarizing effects can distinguish between thermodynamic phase of tropospheric clouds, diattenuation can be used as an indicator for the presence of horizontally oriented ice crystals which are known to impact Earth's radiative budget. We have developed techniques for making this new and novel polarization measurement in the atmosphere. A NOAA lidar has been designed to detect diattenuation in the troposphere and has begun a campaign to detect oriented scatterers over Summit Camp, Greenland. The lidar was tilted by 11° off zenith in late April 2011 and initial results of this campaign are shown. These results appear promising in demonstrating the lidar's ability to perform this novel measurement for detection of horizontally oriented ice crystals.

Dedication

For my wife, Sarah.

Acknowledgements

I would like to thank my research advisor, Prof. Jeffrey Thayer for his support and encouragement throughout my Ph.D. The list of instances where his advising has proven motivating and inspiring are too long to list here.

I would like to thank my committee. In addition to their general responsibilities on the committee, each has made unique contributions to my experience. Prof. Kelvin Wagner volunteered to act as second reader, and has shown great attention to detail in this work. Prof. Juliet Gopinath provided me an opportunity to serve as her TA. Prof. Robert McLeod acted as my advisor within the Optics/EE department when I first started my research. Prof. Xinzhao Chu heads a lidar group at the university with whom we often collaborate, communicate and share equipment.

I would like to thank my fellow graduate students. Ryan Neely is my collaborator on CAPABL. Steve Mitchell is the graduate student responsible for INPHAMIS and I greatly appreciate the opportunity to contribute to his project. Katrina Bossert has assisted in understanding existing lidar techniques for detecting oriented scatterers by analyzing CALIPSO data and Robert Stillwell has done a great amount of work on characterizing CAPABL's detector response. Katelynn Greer ran ARCLITE for many weeks in Greenland to acquire PMC data. Sean Quirin is generally regarded as a lunatic.

Thank you to Mike Hardesty, Scott Spuler, Bruce Morely, and Gary Gimmestad and my friends and family for their support and encouragement.

Finally, I would like to thank the National Science Foundation for its financial support under Grant No. ATM-0454999.

Contents

Chapter

Tables

Table

Figures

Figure

Chapter 1

Polarization In Lidar

Changes in electro-magnetic waves imposed by the atmosphere are used in remote sensing to determine the properties of the propagation medium. These changes may include the wave's propagation direction, frequency, phase or polarization. In atmospheric Light Detection and Ranging (lidar) an optical wave is transmitted, scattered, received and analyzed. The most basic form of lidar measures only total backscatter intensity which provides the most basic information about atmospheric density and the presence of aerosol scatterers. By adding wavelength sensitivity, the lidar may be used to measure the concentrations of certain species [29], wind and temperature [79]. The introduction of polarization measurements is a logical extension to existing lidar designs, conceptually only requiring the addition of a polarizer or polarizing beam splitter to quantify how scatterers change polarization. This polarization information provides another data product, adding further accuracy to the "signature" of clouds and aerosols for identification, classification, and characterization.

1.1 Polarization Characterization of Scatterers

The first lidar polarization measurements of the atmosphere were published in 1971 [76]. These measurements were an analog to polarization radar measurements of the time. Unlike radar, however, tropospheric aerosols and hydrometeors are too large to be strictly described by Rayleigh scattering [71]. As a result, the extremely small depolarizations caused by particle asphericity at radar wavelengths proved to be substantial in lidar [70]. Because of the large polarization changes

observed, lidar instruments were easily designed and adapted to resolve atmospheric depolarization. Since 1971, polarization has become a common, useful and nearly standard lidar parameter along with backscatter and extinction for aerosol characterization studies ranging from the troposphere to the mesopause. Studies have included measurement of water phase, dust characterization, polar stratospheric cloud studies, polar mesospheric cloud studies, volcanic ash detection and quantification, detection of oriented ice crystals and many other applications.

Owing to the fact that liquid water drops are spherical, their single backscattering matrix preserves the incident polarization [71]. By contrast, ice crystals are highly aspherical and their backscattered signals scramble the polarization causing it to be significantly depolarized. Thus polarization lidar can characterize the thermodynamic phase of clouds [71, 16]. Characterization of liquid and solid phase clouds continues to be a major application of polarization lidar. It is this mission that was the primary driver for the deployment of a new lidar system called CAPABL (see Chapter 7) to Summit Camp, Greenland.

Storms over large deserts are known to distribute dust over large regions [36], providing nuclei for formation of cirrus cloud ice crystals [37] and impacting radiative balance. Depolarization is a useful tool for identifying dust due to the sharp edged crystalline shape of the particles that have a size parameter on the order of one [57, 73]. The particle size parameter defines the relative size of a particle to the optical wavelength and is written [87]

$$x = \frac{2\pi a}{\lambda}, \tag{1.1}$$

where x is the size parameter, a is the particle radius and λ is the incident wavelength. Generally Rayleigh scattering is an acceptable approximation for describing particle wave interaction when $x \ll 1$.

Polar stratospheric clouds (PSC) come in two varieties, differing in chemical makeup. Type I clouds are made up of nitric acid trihydrate, while Type II are composed of water [24]. These two cloud types can be distinguished based on their relative backscatter intensities [60]. However, Type I clouds are further classified into Type Ia where particles are spherical with radii near $0.5\mu m$

and Ib where particles are aspherical with volume equivalent radii near $1.0\mu m$ [86]. The distinction between these two clouds are related to ambient temperature and cooling rates. Classifying Type I PSCs is commonly done by detecting the depolarizing properties of the cloud. If depolarization is large, aspherical particles must be present and the cloud is classified as Type Ib.

Polar mesospheric clouds (PMC) are high altitude clouds that form in the summer months at the high latitudes. These clouds form at a centroid altitude of 83 km and are made up of ice particles [34] with radii on the order of 50nm [89]. The particle shape impacts the surface-area-to-volume ratio, and therefore the fall rate of the ice particles through the region of supersaturation where growth occurs [64]. Particle shape has important implications for microphysical models that attempt to explain the behavior of these high altitude clouds. Polarization measurements are sensitive to particle shape and have been used to determine if PMC particles are spherical [7].

Volcanic ash consists of aspherical minerals that come in a variety of sizes. The largest of these quickly settle out of the atmosphere while leaving behind other products of volcanic eruption, such as SO_2 in the stratosphere, that can linger for weeks. In the troposphere, these ashes have been shown to pose a threat to aircraft [48], highlighting the importance of identifying the presence of such atmospheric scatterers. Polarization lidar has been used to detect the depolarizing volcanic ash [74]. Advances in polarization techniques have improved the ability of scientists to evaluate air travel safety following volcanic eruptions.

When ice crystals orient within a common plane, they can cause an increase in planetary albedo [17, 83]. Scanning polarization lidar has been applied to detect oriented ice crystals [56]. Oriented ice crystals, unlike randomly oriented, have very low apparent depolarization if the lidar operates along zenith. However, when the lidar is tilted off zenith, apparent depolarization occurs. Thus, through this scanning polarization technique, the presence of oriented scatterers is marked by a sudden decrease in depolarization when the lidar is tilted near zenith. We will discuss how polarization characteristics of oriented scatterers are different from their randomly oriented counterparts in Chapter 3. This difference in polarization properties can then be exploited for the purpose of identifying oriented scatterers with a new polarization lidar technique introduced in Chapter 4.

The above descriptions of polarization lidar applications are by no means exhaustive. Other applications have included detection of honey bees [78], bioaersol plumes [45], drop size from multiple scattering signals [65] and fish detection [21].

1.2 Conventional Lidar Theory

Direct detection lidar generally operates by transmitting a laser pulse and collecting the resulting backscattered light. Since the speed of light in a vacuum is known, the range of a particular backscattered signal can be determined using time of flight [47]

$$R = \frac{c}{2\Delta t}, \tag{1.2}$$

where Δt is the time of flight and c is the speed of light in a vacuum. In the optical regime where the atmosphere is the medium of propagation and range resolution is on the order of meters (time resolution is on the order of several ns), the index of refraction may be regarded as 1. This ranging technique requires that optical signals under consideration are only attributable to single scattering. In most atmospheric cases, this is a valid assumption. However, in the case of optically dense clouds, multiple scattering cannot be ignored [12], causing inaccuracy in ranging through time of flight. Photons that are multiply scattered may traverse paths substantially longer than that of the single scattering event. In such cases, it becomes difficult to determine what attributes imposed on the wave correspond to a particular range.

Conventional non-polarization lidar is described through the Scalar Lidar Equation, which relates the transmitted and received intensity or photons through the atmospheric medium [47]

$$N_S(R,\lambda_s) = N_L(\lambda_i)\left[\beta(\lambda_i,\lambda_s,R)\Delta R\right]\frac{A}{R^2}T(\lambda_s)T(\lambda_i)\left[\eta_{RX}\eta_{TX}G(R)\right] + N_B, \tag{1.3}$$

where $N_S(R,\lambda)$ is the number of received photons at range R and wavelength λ, $N_L(\lambda)$ is the number of transmitted photons at wavelength λ, $\beta(\lambda_i,\lambda_s,R)$ is the total volume backscatter coefficient from incident wavelength λ_i into scattered wavelength λ_s, ΔR is the range bin resolution, A is the receiver effective aperture, R is the range to the scattering target, $T(\lambda)$ is the transmission of

the atmosphere at wavelength λ, η_{TX} and η_{RX} are the transmitter and receiver system efficiencies respectively, *G(R)* is the geometrical overlap accounting for low altitude returns that may not pass through the receiver field stop with the same efficiency as high altitude returns, and $N_B(\lambda)$ is the background noise at wavelength λ.

For most lidar applications, Eq. (1.3) provides sufficient free variables to give full description to system operation. Because all terms are scalars, their grouping is arbitrary.

Absolute backscatter signals N_S are often difficult to calibrate and quantify. This is due, in part, to uncertainty in system efficiencies. The make-up and extinction of the troposphere is subject to frequent variation, further complicating the exact meaning of absolute backscatter. Instead we often quantify backscatter using a ratio to molecular returns. This is defined [20]

$$R_{BS} \equiv \frac{\beta^{tot}}{\beta^{mol}}, \tag{1.4}$$

where β^{tot} is the total volume backscatter coefficient and β^{mol} is only the molecular volume backscatter coefficient. The volume backscatter coefficients are proportional to the received background subtracted photon counts, so the backscatter ratio is determined from lidar signals using

$$R_{BS} = \frac{N_S^{tot} - N_B^{tot}}{N_S^{mol} - N_B^{mol}}, \tag{1.5}$$

where the superscript denotes the photon counts attributed to the total medium backscatter or molecular backscatter. The actual process of determining molecular backscatter components varies depending on system capability. In some cases the system can spectrally separate molecular and aerosol returns [80, 30]. Raman returns can also be used to determine molecular density as a function of altitude [3]. Often Rayleigh lidar use higher altitude signals attributed strictly to molecular returns to seed a numerical inversion that solves for the backscatter ratio [40].

1.2.1 Polarization Lidar Conventions

The theory developed for conventional polarization lidar can be traced to radiative transfer theory using modified Stokes vectors and Mueller matrices [26]. Over time however, polarization

lidar convention has lost this connection and is typically described using two independent scalar lidar equations. The vast majority of polarization lidars operate by transmitting a single polarization and measuring the subsequent return power parallel and perpendicular to the original polarization [71]. Because this optical technique cannot measure phase, it does not fully characterize a the received polarization. As a result, this measurement cannot provide a general connection to the scattering phase (or Mueller) matrix. This measurement technique gives description to how much the polarization changed, but it is ambiguous as to how the polarization changed.

Conventional polarization lidar theory strictly conforms to the polarization technique described above. Thus the description for photons detected on the channel parallel to the transmitted polarization is nearly identical to Eq. (1.3), except that the volume backscatter coefficient now only describes the propensity of the scatterer to maintain the original polarization and is written $\beta_{\|}$ [71]. A second scalar equation is then used to describe the perpendicular channel. In this equation, the backscatter coefficient describes the propensity of the scatterer to couple optical power into the orthogonal polarization mode and is written $\beta_{\perp}$. To reflect the possibility that atmospheric transmission may be polarization dependent, the return atmospheric transmission term in the perpendicular equation is given the $\perp$ subscript. Thus the two scalar equations describing the measured quantities of conventional polarization lidar systems are

$$\begin{aligned} N_{S||}(R) &= N_L \beta_{||}(R) \Delta R \frac{A}{R^2} T_{||}^2 \eta_{RX||} \eta_{TX} G(R) + N_{B||} \\ N_{S\perp}(R) &= N_L \beta_{\perp}(R) \Delta R \frac{A}{R^2} T_{||} T_{\perp} \eta_{RX\perp} \eta_{TX} G(R) + N_{B\perp}, \end{aligned} \tag{1.6}$$

where the dependence on wavelength has been dropped to assume that elastic scattering processes are detected. The perpendicular channel will read zero as long as the scattering processes in the atmosphere are polarization preserving ($\beta_{\perp} = 0$). A normalized measure of the polarization change in the atmosphere is then defined by the ratio of the two polarization backscatter coefficients and called the polarization ratio (sometimes depolarization ratio) [71]

$$\delta \equiv \frac{\beta_{\perp}}{\beta_{\|}}. \tag{1.7}$$

Note that the polarization ratio is very nearly the ratio of the two detection channel photon counts.

The polarization dependence of atmospheric transmission and system efficiency are folded into a single calibration constant to give the polarization ratio in terms of signal counts [75, 10, 46]

$$\delta = \frac{T_{||}\eta_{RX||}}{T_{\perp}\eta_{RX\perp}}\frac{N_{\perp}}{N_{||}} = K\frac{N_{\perp}}{N_{||}}. \tag{1.8}$$

The polarization ratio, based on Eq. (1.6), appears to give complete description to all polarization scattering processes. However, we shall see that conventional polarization lidar descriptions are based on the system's mode of operation, not actual scattering processes. While the polarization ratio gives complete description to polarization properties that can be ascertained via conventional operation, it by no means fully describes the polarization processes exhibited by all atmospheric scatterers.

Despite the fact that $\eta_{RX||}$ and $\eta_{RX\perp}$ are the only optical system effects described by Eq. (1.6), there have been additional relations suggested to account for other systematic error sources. The polarizer in the receiver may not perfectly align to the transmitted polarization, yet there is no description for this error or how it may impact polarization measurements [72]. The fact that this obvious source of system error has no description in the polarization lidar equation demonstrates the limiting nature of Eq. (1.6). Nevertheless, this polarization lidar equation has continued to be used with little modification.

1.3 New Polarization Lidar Developments

Conventional polarization lidar theory has recently received some criticism for its use of the polarization ratio as a complete description for atmospheric scattering [26]. In electro-magnetic theory, incoherent scattering is typically described by 16 element Mueller matrices [87, 52]. While these matrices can sometimes be reduced to scalar quantities ($\beta_{||}, \beta_{\perp}, \delta$) based on polarizations used in the lidar system, their exact values are a function of incident polarization [25].

Some researchers, in recognition of the complexities of scattering, have extended their polarization lidar capabilities to measure the full received Stokes vector [31]. While this work represents a definite step forward, the received Stokes vector is still a function of the transmitted polarization.

Unfortunately, the transmit polarization is often not reported, so relating measurements to the actual scatterer becomes difficult. It is important to note that a four element Stokes vector does not provide a complete characterization of the 16 element Mueller matrix, also called a scattering phase matrix, that describes the scattering volume.

In some of the most complete atmospheric polarization research to date, [39] fully measures all 16 elements of the scattering phase matrix for the purpose of studying oriented scatterers. The approach used in this lidar system is thorough, and provides a useful baseline for future polarization lidar design. The drawbacks largely come from practical issues. The Mueller matrices of oriented scatterers have a known form, where eight elements are zero. While physically measuring all terms is a useful exercise for validating scattering theory, signal integration time is better spent only measuring elements that may be non-zero. Also the complexity of these measurements may prove too much for widespread use, which require six intensity measurements for each of four transmit polarizations. In a research environment where study of oriented scatterers is only one of many mission objectives, full polarimetric capability may be too focused for common use.

1.3.1 Correction of System Effects

Polarization corrupting effects in the optical system, such as retardance, diattenuation and depolarization, present a concern for polarization data accuracy. For this reason, a number of techniques have been attempted to determine the polarization measurement accuracy of a lidar receiver. In [77], three methods are employed where the cross polarized rejection of the initially polarized input is measured: A laser is expanded to fill the telescope aperture but is not collimated, collimated lasers with narrow beams are directed into the telescope at a variety of points in the telescope aperture, and a sheet polarizer is placed on the telescope aperture thus polarizing the sky-light. Similar to the third technique, LCD monitors on laptops have also been used [Witt,personal communication, 2009] to measure cross polarized rejection of the receiver. From these rejection measurements, a baseline instrument error is assumed.

To calibrate out system effects, a number of techniques have been developed to determine the

calibration constant in Eq. (1.8) [75, 10, 46]. From Eq. (1.6) and (1.8) it would appear that the calibration constant accounts for all polarization corruption potential of the instrument. However in [72], with limited explanation and no derivation, an equation and technique are presented for correcting polarization misalignment of the transmitter and receiver by adding an additional term

$$\delta = K\frac{N_{\perp}}{N_{||}} - \chi. \tag{1.9}$$

It is difficult to know how the above correction was developed since polarization misalignment has no description in Eq. (1.6). Furthermore, it is not clear whether the authors are aware that this calibration technique is not accurate in the presence of non-depolarizing scatterers.

We will show how thorough polarization theory presents opportunities for instrument characterization and polarization lidar measurements even when optical system effects are substantial (see Chapter 5). Correction schemes using hardware and software have a demonstrated use at the Arctic Lidar Technology (ARCLITE) facility in Greenland for the purpose of studying PMCs, PSCs, stratospheric aerosols, and cirrus clouds. Furthermore, error sensitives of polarization lidar can be determined to greater accuracy through the use of optical polarization theory. This defines limitations on polarization accuracy of a system, and in some cases, allows polarization measurement techniques to be developed so they are entirely insensitive to the instrument's polarization effects.

1.3.2 Expanded Sensing Capabilities

The scattering phase matrix is the angle dependent Mueller matrix that fully describes the polarization attributes of the scattering volume. It is the only scattering description sufficiently general to encompass all polarization effects exhibited by atmospheric scatterers. The expanded use of Mueller matrices in polarization lidar descriptions opens the possibility of additional phase matrix measurement techniques. These techniques are developed for the purpose of augmenting lidar mission objectives through simple modifications that are practical for remote sensing campaigns with broad objectives.

For the purpose of identifying oriented scatterers I will present polarization methods I have developed to detect scattering matrix diattenuation. Randomly oriented scatterers cannot exhibit this polarization effect, making it a unique marker for oriented scatterers. The techniques developed for this purpose are specific to two lidar systems with different operating objectives, polarization effects and capabilities. While it is unlikely that detection of oriented scatterers is the only new opportunity in polarization sensing, it represents a significant step in the approach to polarization in lidar. Conventional techniques are neither rejected nor are they allowed to confine the approach and possibilities of lidar operation and design.

1.3.3 Lidar System Development

ARCLITE and CAPABL are the two lidar systems presented in Chapters 6 and 7 that have benefited from the polarization theory I have developed in this work. The ARCLITE lidar in Kangerlussuaq, Greenland ($67.0°N, 50.9°W$) has been in operation since 1992 with a research focus on the stratosphere and mesosphere [84]. This instrument has benefited substantially from my development of system polarization mitigation techniques including hardware compensation to cancel phase shifts in the optical system [33] thereby providing improved solar background rejection and SNR. Also post processing software correction was developed to remove residual retarding and depolarizing effects from polarization measurements [32]. Additional polarization capability has been suggested in the form of diattenuation measurements that have been designed and demonstrated on this system with very little modification.

The Cloud Aerosol Polarization and Backscatter Lidar (CAPABL) is a refurbished NOAA lidar system, with polarization redesign. It was deployed to Summit Camp, Greenland ($72.6°N$, $38.5°W$) in the spring of 2010 as part of the Integrated Characterization of Energy, Clouds, Atmospheric State, and Precipitation over Summit (ICECAPS) project. I collaborated with Ryan Neely III in redesigning the lidar to minimize polarization error from the instrument and expand its capability to identify oriented scatterers through a three-polarization detection scheme. For the past year, CAPABL has been operating in zenith pointing mode for the purpose of identifying

cloud and precipitating particle phase through depolarization measurements and exploring possible conditions of false positives in oriented scatterer detection. The lidar was tilted off zenith by 11° on April 23, 2011 to begin a campaign of identifying oriented scatterers above Summit Camp. After tilting the lidar, we have identified a number of lidar profiles that may be attributed to the presence of oriented scatterers in atmosphere.

Chapter 2

The Stokes Vector Lidar Equation

2.1 Framework for Polarization in Lidar

Because polarization lidar was initially developed as an extension of traditional lidar, researchers often incorrectly assume that its description should be derived from the lidar equation given by Eq. (1.3). However, a scalar description of electro-magnetic wave propagation only exists when polarization effects are irrelevant to measured quantities. Any instance where this is not the case mandates reversion to the more general vector description of wave propagation.

Likewise, Eq. (1.3) can be derived from the polarization lidar equation under the assumption that there is no polarization dependence in the total optical path (transmission to detection). The description of a polarization lidar must be developed from the traditional optical description of polarization. The polarization state of the electro-magnetic field is specified and fully propagated through the entire optical path to obtain a rigorous description for polarization lidar. Operators in the equation must also be described by polarization theory with effects more diverse and complicated than simply scaling the intensities in the two measured polarization modes. With this more fundamental description, polarization modes can be coupled, attenuated, and rotated in a variety of ways which may make parameters like the depolarization ratio appear disconnected from actual scattering theory. Some researchers have devoted some level of consideration to these polarization effects, but they have no derivable basis when using Eq. (1.6) as a system description.

We use Stokes vectors to represent the polarization state of an electro-magnetic field and Mueller matrices to describe their interactions with all elements along the optical path including

transmitter, scatterer and receiver. Generally atmospheric polarization lidars measure parameters of randomly distributed scatterers in a volume. The integration time of the lidar measurement exceeds the decorrelation time of the medium. Thus the light is regarded as incoherent and system descriptions are linear in intensity with light being fully, partially, or unpolarized [14]. Polarization lidar should be described more completely in a form called the Stokes Vector Lidar Equation (SVLE) which is written

$$\vec{S}_{RX} = \mathbf{M_{RX}} \left[\left(G(R) \frac{A}{R^2} \Delta R \right) \mathbf{T_{atm}}(\vec{k}_s, R) \mathbf{F}(\vec{k}_i, \vec{k}_s, R) \mathbf{T_{atm}}(\vec{k}_i, R) \mathbf{M_{TX}} \vec{S}_{TX} + \vec{S}_B \right], \qquad (2.1)$$

where $\vec{S}_{RX}$ is the received Stokes vector, $\vec{S}_{TX}$ is the Stokes vector describing the laser polarization state, $\mathbf{M_{TX}}$ is the Mueller matrix description of the transmitter, $\mathbf{T_{atm}}(\vec{k}_i, R)$ is the Mueller matrix description of the atmospheric transmission to the scatterer along incident wave vector $\vec{k}_i$ over the range R, $\mathbf{F}(\vec{k}_i, \vec{k}_s, R)$ is the scattering phase matrix (or Mueller matrix) of the scattering medium at range R for incident and scattered wave vectors $\vec{k}_i$ and $\vec{k}_s$ respectively, ΔR is the integration range bin, A is the collection aperture, *G(R)* is the geometrical overlap function, $\mathbf{M_{RX}}$ is the Mueller matrix description of the receiver, and $\vec{S}_B$ is the Stokes vector of the background at the input of the receiver. In all cases, the Stokes vectors and Mueller matrices are not normalized so that overall scattering and system efficiencies may be found in the (1,1) element of their respective Mueller matrix and intensity or photon counts is carried in the first element of the Stokes vector. Thus, we will be using the unmodified Stokes vector representation in this work.

The transmitted polarization is propagated through the entire optical path, allowing for interactions with multiple matrices before it is finally analyzed and measured in the receiver. This description is fully general for direct detection lidar and allows for complete analysis and understanding of polarization effects along the optical path that otherwise may not have description using conventional polarization lidar theory.

2.2 Mueller Matrix Decomposition

The possible descriptions of instrument and scatterer polarization effects described by a Mueller matrix are more diverse than those derived from the polarization lidar equation described in Eq. (1.6). A Mueller matrix will transform and couple polarization rather than simply attenuate modes corresponding to the measured channels.

The components of any realizable Mueller matrix can be described as a combination of retarders, diattenuators and depolarizers [42]. This description is not limited to matrices in the lidar instrument and can be extended to the atmospheric transmission and scattering phase matrices.

All three realizable components of a Mueller matrix have the capacity to couple polarization modes. Most often system effects are consolidated into a single error term in polarization ratio data. However, the ability to calibrate, compensate or ignore these effects strongly depends on which attributes both the lidar and scatterer exhibit.

In this section we will provide a brief description of the three passive Mueller matrix components.

2.2.1 Diattenuator

A diattenuator may conceptually be described as a weak polarizer. It is fully described by transmission of unpolarized light T_u and its diattenuation vector $\vec{D}$, taking the form [42],

$$\mathbf{M}_D = T_u \begin{bmatrix} 1 & \vec{D}^T \\ \vec{D} & \mathbf{m}_D \end{bmatrix}, \tag{2.2}$$

where $\vec{D}$ is the the diattenuation vector and describes the eigen polarization of the matrix and $\mathbf{m}_D$ is a 3x3 submatrix fully described by the diattenuation vector through [42]

$$\mathbf{m}_D = \sqrt{1-D^2}\mathbf{I} + \left(1-\sqrt{1-D^2}\right)\hat{D}\hat{D}^T, \tag{2.3}$$

where D is the magnitude of the diattenuation vector, $\hat{D}$ is the normalized diattenuation vector and $\mathbf{I}$ is a 3x3 identity matrix.

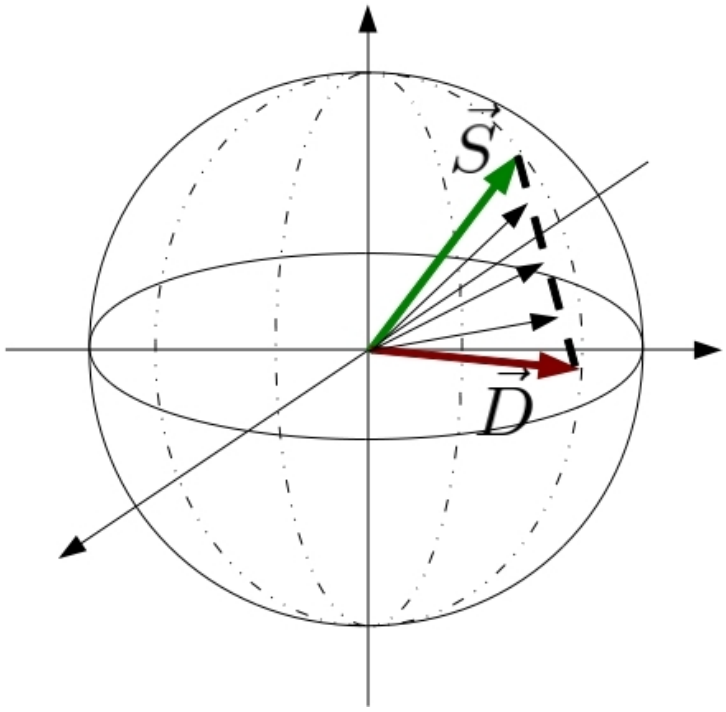

Figure 2.1: Graphical representation of a diattenuator in Poincaré space. The incident Stokes vector (Green) is shortened (decrease in intensity) and is projected toward the diattenuation vector (modifies the polarization state).

Each element of $\vec{D}$ describes the preferential efficiency of the system along horizontal/vertical, $\pm 45°$, and right/left hand circular polarizations. A value of zero indicates no preferential efficiency. A value of one in the first element indicates transmission of horizontal polarization and total rejection of vertical as in an ideal horizontal polarizer.

In Poincaré space, a diattenuator will project the incident Stokes vector onto the Diattenuation vector (see Figure 2.1). Unless the incident Stokes vector points the same direction as the diattenuator, this results in a shorter outgoing Stokes vector. However, the radius of the Poincaré sphere simultaneously decreases so there is no reduction in degree-of-polarization (DOP). The projection also results in a change in outgoing polarization state. The amount of change in intensity and polarization is dictated by the magnitude of the diattenuation vector. Larger $|\vec{D}|$ results in reduced transmission of input polarizations misaligned to $\vec{D}$ and exit polarizations states that more closely resemble the diattenuation vector.

Diattenuators tend to manifest themselves in filters with non-normal incidence angles, folding mirrors, beam samplers using Fresnel reflections, and polarizers. Because the diattenuation vector of most elements in a polarization lidar system are linear, one might assume that the system diattenuation vector always corresponds to linear polarizations. However, when a diattenuator is combined with retarding elements, the vector can point in any arbitrary direction within the three element Stokes vector subspace called the Poincaré Sphere, and often corresponds to elliptical polarizations.

A strict intensity description of diattenuation is polarization dependent efficiency, so it is the closest polarization effect to that originally described in Eq. (1.6) with system efficiencies $\eta_{RX||}$ and $\eta_{RX\perp}$. Though those efficiencies fail to fully account for the capacity of a diattenuator to modify both the polarized and unpolarized components of incident light, it means that many lidar designs have succeeded in reducing this effect in the optical system. In the scattering phase matrix, diattenuation is manifested in non backscattering, multiple scattering and oriented scatterer conditions.

2.2.2 Retarder

A retarder is a wave plate with an arbitrary fast axis that imposes a phase shift Γ on incident polarization modes. This causes a rotation of the Stokes vector on the Poincaré Sphere about retardance vector $\hat{R}$. Like the diattenuator, the retardance vector does not necessarily correspond to linear polarization.

The retarder Mueller matrix takes the form [42]

$$\mathbf{M}_R = \begin{bmatrix} 1 & \vec{0}^T \\ \vec{0} & \mathbf{m}_R \end{bmatrix}, \tag{2.4}$$

where $\vec{0}$ is a three element zero vector and $\mathbf{m}_R$ is a 3x3 submatrix of $\mathbf{M}_R$ acting as a rotation matrix of angle Γ about the axis of its eigenvector $\hat{R}$. This rotation matrix may be generally written [42]

$$\mathbf{m}_R = \delta_{ij}\cos\Gamma + \epsilon_{ijk}R_k\sin\Gamma + R_iR_j(1-\cos\Gamma), \tag{2.5}$$

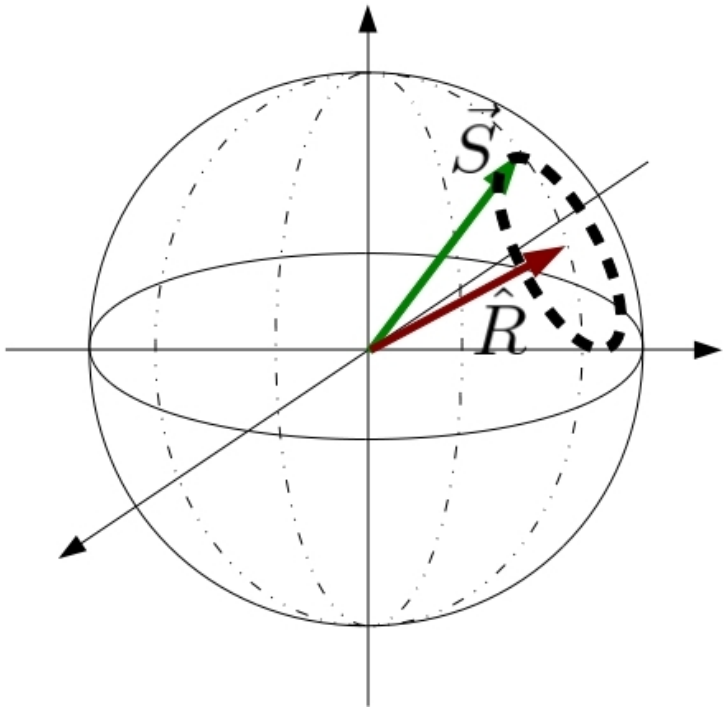

Figure 2.2: Graphical representation of a retarder in Poincaré space. The incident Stokes vector (Green) is rotated about the retarder fast axis (red). The angle of rotation is given by the phase shift between fast and slow axes of the retarder.

where δ_{ij} is the Kronecker delta, ϵ_{ijk} is the Levi-Cervitá permutation symbol, R_i is the ith element of the eigenvector $\hat{R}$ and Γ is the retarder phase delay.

The eigenvector of the Mueller matrix corresponds to the eigen polarization of the optic or system, where the total intensity may be scaled, but the polarization state is unchanged.

In Poincaré space, the retarder causes a rotation of the input Stokes vector about the retarder fast axis, $\hat{R}$ (see Figure 2.2). The angle of rotation is given by the retardance or phase shift between the fast and slow axes of the retarder.

In polarization lidar systems, retardance will modify the polarized state of incident light, but unlike the diattenuator, it will preserve the degree-of-polarization. Generally a retarder will convert linear polarizations into elliptical, making complete acceptance or rejection of polarization modes impossible with a linear polarizer. Such effects are incorrectly described as “depolarization” by some lidar researchers. A retarder is a fundamentally different operator than a depolarizer and

can be corrected in many instances.

Retardance commonly appears when lidar systems use folding mirrors to steer ray paths in their system. Newtonian telescopes are notorious for demonstrating this behavior due to the folding secondary mirror. Beam steering mirrors can also introduce retardance to transmit polarizations. Avoiding large angles of incidence on mirrors will reduce this effect in a polarization lidar system. Low phase shift mirrors can also be employed, but it is often difficult to obtain retardance specifications from suppliers. Wave plate configurations can be used to cancel these effects by imposing the opposite phase shift of the system (see Chapter 5). Such configurations are easily realized using techniques described in [82, 4]. For strictly depolarizing scatterers retardance in a lidar receiver can be removed in post processing via calibration techniques as long as there is negligible diattenuation in the system[32].

In a homogeneous Mueller matrix, the effects of diattenuation and retardance are indicated by non-zero positions in the matrix [19]

$$\begin{bmatrix} \square & a & b & c \\ a & \square & -f & -e \\ b & f & \square & -d \\ c & e & d & \square \end{bmatrix}, \tag{2.6}$$

where $\square$ represents matrix terms that are not attributable to a single polarization effect and the symmetric terms a, b, and c indicate diattenuation along horizontal/vertical, $\pm 45°$, and right and left circular polarizations respectively. The antisymmetric terms d, e, and f indicate retardance about horizontal/vertical, $\pm 45°$, and right/left circular polarizations respectively. Loss of symmetry in the diattenuation terms or loss of antisymmetry in retarding terms indicates the presence of depolarization or inhomogeneity.

2.2.3 Depolarizer

Depolarization matrices are Mueller matrices describing nondeterministic polarization systems [81]. Included in the general set of these matrices are what we would more commonly think

of as the depolarizers that decrease the degree-of-polarization of incident light. In simple instances, depolarizers take the form of a diagonalized matrix

$$\mathbf{M}_{\Delta} = \begin{bmatrix} 1 & 0 & 0 & 0 \\ 0 & a & 0 & 0 \\ 0 & 0 & b & 0 \\ 0 & 0 & 0 & c \end{bmatrix}, \tag{2.7}$$

where a, b, and c are the tendency of horizontal/vertical, $\pm 45°$, and right/left circular polarizations to remain polarized respectively. The backscattering matrix of randomly oriented axially symmetric particles strictly conforms to a depolarizing matrix of this form. If a matrix decomposition of non backscattering conditions is performed, the depolarization matrix will generally exhibit polarizance as well and may not necessarily be in a diagonalized form. Instead the most general form for a depolarizer is written

$$\mathbf{M}_{\Delta} = \begin{bmatrix} 1 & \vec{0}^{T} \\ \vec{P} & \mathbf{m}_{\Delta} \end{bmatrix}, \tag{2.8}$$

where $\vec{P}$ is the polarizance vector describing the exit polarization state of unpolarized incident light and $\mathbf{m}_{\Delta}$ is a 3x3 submatrix of the matrix $\mathbf{M}_{\Delta}$. In the most general case, a depolarizer has nine independent terms, making it difficult to generalize. Three terms define the polarizance vector. Three define the depolarization or eigen values of the submatrix $\mathbf{m}_{\Delta}$. Finally three terms define the 3-dimensional orthonormal basis set of the depolarization terms or eigen vectors of $\mathbf{m}_{\Delta}$.

In Poincaré space the $\mathbf{m}_{\Delta}$ terms of a depolarizer shorten the incident Stokes vector while maintaining a constant radius on the sphere. When all nonzero elements of $\mathbf{m}_{\Delta}$ are on the diagonal and equal, the depolarizer is isotropic and the remaining outgoing polarized light maintains the same state as the input (see Figure 2.3). However, more general anisotropic depolarization and the presence of polarizance $\vec{P}$ can cause the outgoing polarization state to change. Thus, the effect of a depolarizer is difficult to generalize.

Depolarization of the form in Eq. (2.7) can exist in optical systems such as a receiver where mirrors reflect a range of incident angles. This range of angles results in variation of phase shift

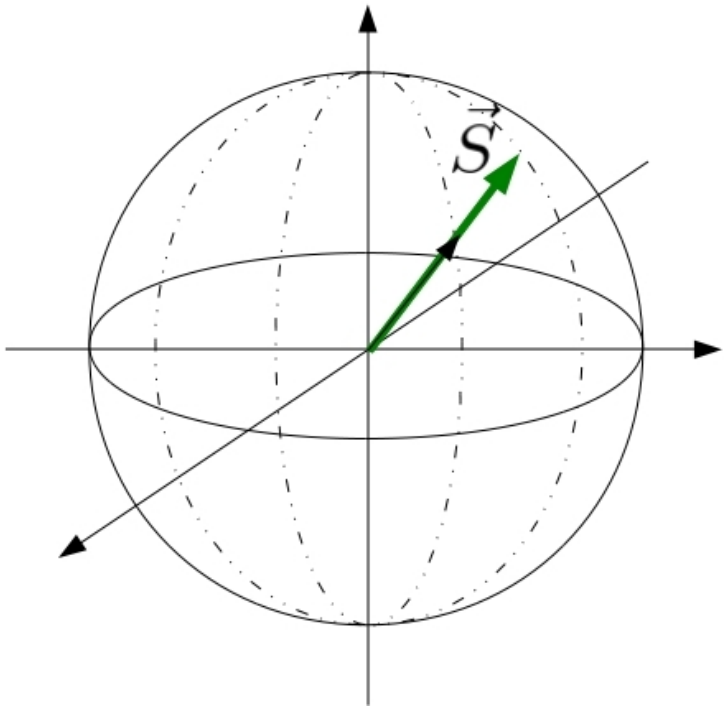

Figure 2.3: Graphical representation of an isotropic depolarizer in Poincaré space. The incident Stokes vector (Green) shortened while the surface of the sphere maintains constant radius. The outgoing light maintains the same polarized state, but some of the original power has been coupled into an unpolarized state.

upon reflection, and the detected light will have a distribution of polarization states. In these cases, the total received Stokes vector is the sum of all individual Stokes vectors and the degree of polarization will likely be reduced [18].

Depolarization in the optical system is much more difficult to remove with hardware than retardance. However, when the backscatter matrix under measurement is strictly depolarizing, and the optical system exhibits little or no diattenuation this effect can be removed in post processing [32].

2.3 The Scattering Medium

The scattering medium in the Stokes Vector Lidar Equation (SVLE) is described by a Mueller matrix called the scattering phase matrix. In the most general sense, this matrix is dependent on the incident and scattered wave vectors. However, when particles are much larger than a wavelength, the matrix is no longer dependent on wavelength. When particles are spherical, or randomly oriented, the medium is macroscopically isotropic so the specific incident and scattered directions are no longer needed. When both of these conditions are true, only the scattering angle between the two vectors is needed.

The scattering phase matrix contains information about both the scattering coefficient and the polarization properties of the medium. The (1,1) element of this matrix (where matrix indices begin at 1) is the volume scattering coefficient $\beta(\vec{k}_i, \vec{k}_s, R)$ from the scalar lidar equation. If this is factored out of $\mathbf{F}(\vec{k}_i, \vec{k}_s, R)$, the remaining normalized matrix strictly describes the polarization properties of the scattering medium. Very often we describe polarization data products in relation to the normalized scattering matrix, allowing us to remove the backscatter dependence of the medium.

Because the phase matrix describes the scatterer, it is this term in the SVLE that must be measured to characterize a scatterer. Often we do not fully measure this matrix. Assumptions about the form of the matrix allow us to assume certain terms are zero. In other cases, measuring additional polarization terms may not provide any additional information about the physical

attributes of the medium. The exact method employed to determine these elements inevitably depends on what assumptions can be made about the form of the scattering matrix. The specific forms of the scattering matrix will be described in more detail in Chapter 3.

2.4 The Lidar Instrument

The Stokes Vector Lidar Equation gives full consideration to the instrument's ability to modify polarization states. Otherwise benign optical elements such as mirrors and beam samplers are notorious for corrupting polarization states. In order to mitigate and minimize error sources, full consideration must be given to the optical effects exhibited by the system.

While specifications are often given by manufacturers for different reflectivity of s- and p-polarization modes, the phase shift upon reflection is rarely reported. As multiple mirrors are combined in an optical system, the more arbitrary the polarization effects become. Frequently after two or three mirrors the eigen polarization states of the optical system are no longer linear polarizations.

In Figures 2.4 and 2.5 the calculated diattenuation and phase shift of a typical aluminum mirror is plotted as a function of incidence angle. At incidence angles below 10° these effects are typically small enough they do not significantly alter the receiver polarization. However at high angles of incidence the effects, if unaccounted for, will skew polarization data.

Mirrors can also depolarize light when it is made up of multiple angular modes. The depolarization then depends on the angular width of the incident beam where the different polarization effects do not add constructively over all incidence angles. This will tend to cancel off diagonal elements in the Mueller matrix and reduce the diagonal elements.

Because the optical systems used to measure polarization in the atmosphere have the ability to modify polarization, they must be included in the polarization lidar description. The polarization effects introduced by instruments have the potential to be far more complicated than those described in conventional theory.

The impact of polarization effects on measurements techniques described in this work will be

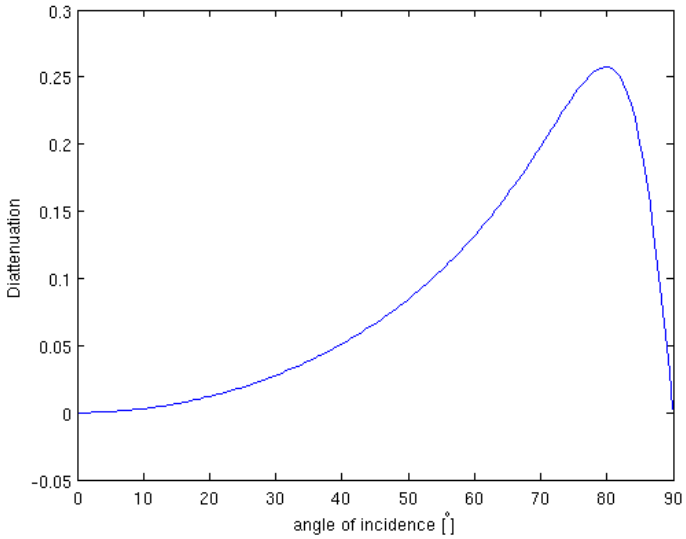

Figure 2.4: Simulated diattenuation of an aluminum mirror as a function of incidence angle.

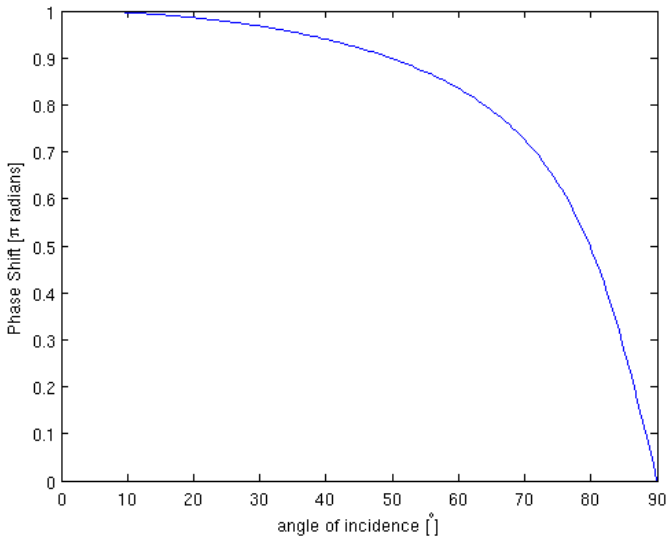

Figure 2.5: Simulated phase shift of an aluminum mirror as a function of incidence angle.

discussed in Chapter 5.

2.5 Transmit Polarization

The laser output is described by a Stokes vector with the form

$$\vec{S}_{TX} = \begin{bmatrix} S_0 \\ S_1 \\ S_2 \\ S_3 \end{bmatrix}, \tag{2.9}$$

where S_0 is the total total power, photons, or intensity, S_1 is the total power in the horizontal/vertical linear polarization, S_2 is the power in the $\pm 45^\circ$ linear polarization, and S_3 is the power in the circular polarizations. The relationship between all of these terms can also be written given in terms of physical parameters of the polarization

$$\vec{S}_{TX} = N_{TX} \begin{bmatrix} 1 \\ P_{TX} \cos 2\phi_{TX} \cos \Gamma_{TX} \\ P_{TX} \sin 2\phi_{TX} \cos \Gamma_{TX} \\ P_{TX} \sin \Gamma_{TX} \end{bmatrix}, \tag{2.10}$$

where N_{TX} is the total photons in the outgoing laser, P_{TX} is the laser degree-of-polarization (DOP), ϕ_{TX} is the linear rotation angle of the polarization, and Γ_{TX} is twice the ellipticity angle such that $\Gamma_{TX} = \frac{\pi}{2}$ makes $\vec{S}_{TX}$ left hand circularly polarized.

Knowing the detection technique's sensitivity to error in the outgoing polarization is often critical. Some issues may be corrected using software, while others will require wave plates or a polarizer in the transmitter system to clean up the outgoing beam.

After the laser is emitted, it must pass through a transmitter optical system $\mathbf{M_{TX}}$ often consisting of steering mirrors, wave plates and beam expanders. Some of the optical elements have the potential to corrupt the polarization state of the outgoing laser light. Thus it is often necessary to cancel the polarization effects or only operate in the eigen polarization of $\mathbf{M_{TX}}$.

2.6 Polarization Measurement

Stokes vectors cannot be measured directly, so the process of detecting the polarization $\vec{S}_{RX}$ requires the vector be projected onto various axes of the the Poincaré sphere. Each projection then generates a resultant photon counts or intensity that could be used to reconstruct $\vec{S}_{RX}$.

In order to determine the number of photon counts received on a projection channel, an output description must be formed to accommodate Eq. (2.1). Thus the full description of the measured photon counts would be given by

$$\vec{N} = \mathbf{OM_{RX}} \left[\left(G(R) \frac{A}{R^2} \Delta R \right) \mathbf{T}_{atm}(\vec{k}_s, R) \mathbf{F}(\vec{k}_i, \vec{k}_s, R) \mathbf{T}_{atm}(\vec{k}_i, R) \mathbf{M_{TX}} \vec{S}_{TX} + \vec{S}_B \right], \tag{2.11}$$

where all but the measurement terms are from Eq. (2.1) and

$$\vec{N} = \begin{bmatrix} N_1 \\ N_2 \\ \vdots \end{bmatrix}, \tag{2.12}$$

where N_n is the photon counts on the *nth* channel and $\mathbf{O}$ is the output projection matrix corresponding to those measurements (generally polarizer matrices) and written

$$\mathbf{O} = \mathbf{o} \begin{bmatrix} \mathbf{P_1} \\ \mathbf{P_2} \\ \vdots \end{bmatrix}, \tag{2.13}$$

where $\mathbf{P_n}$ is the *nth* projection corresponding to the *nth* channel and

$$\mathbf{o} = \begin{bmatrix} \eta_1 & 0 & 0 & 0 & 0 & 0 & 0 & 0 & \\ 0 & 0 & 0 & 0 & \eta_2 & 0 & 0 & 0 & \cdots \\ & & & & \vdots & & & & \end{bmatrix}, \tag{2.14}$$

where η_n is the *nth* channel detector efficiency. This matrix $\mathbf{o}$ denotes that after projection, only the first element of the Stokes vector is measured. For N measurements, $\mathbf{o}$ is Nx$4N$. In the case of scalar lidar, $\mathbf{O}$ simplifies to $\begin{bmatrix} \eta & 0 & 0 & 0 \end{bmatrix}$.

It is important to note that the scattering matrix is the term under investigation, not necessarily the received Stokes vector. For this reason, it is not always necessary to perform projections and characterize $\vec{S}_{RX}$. As will be shown later with the Alternating Cross Polarized technique, some phase matrix elements can be determined without polarization analysis of the received light by capturing phase matrix information in the S_0 element of the returned Stokes vector.

2.7 Atmospheric Transmission

For media where higher order scattering effects are weak, single scattering may be assumed so that the polarization state of the transmitted laser light is described by a single volume element between transmitter and scatterer

$$\mathbf{T_{atm}}(\vec{k}_i) = \mathbf{F_{col}}(\vec{k}, \vec{k}, R) + \left(\mathbf{I} - \mathbf{E_{col}}(\vec{k}, R)\right), \tag{2.15}$$

where $\mathbf{F_{col}}(\vec{k}, \vec{k}, R)$ is the column integrated volume forward scattering matrix of the propagation medium through distance R for wave vector $\vec{k}$, $\mathbf{E_{col}}(\vec{k}, R)$ is the column extinction matrix of the path to or from the scatterer and $\mathbf{I}$ is an identity Mueller matrix. For common atmospheric applications of single scattering where extinction is polarization independent and the forward scattering coefficient is small compared to the unextinguished light

$$f_{11}^{col}(\vec{k}, \vec{k}, R) \ll \left(1 - e_{11}^{col}(\vec{k}, R)\right), \tag{2.16}$$

the polarization effects of the atmosphere on the transmitted and received path may be ignored. This assumption is generally applied to most atmospheric applications [38] except optically dense clouds. This assumption will be generally applied to all applications discussed in this work.

In cases where we cannot assume the forward scattering coefficient of the column f_{11}^{col} is small, the transmission matrix from lidar to scatterer must be determined using two stream, polarized, radiative transfer [41]. This is done by solving a differential equation describing the population of forward and backward propagating photons within a volume. In this case, forward and backscattering may occur multiple times, and due to the extended propagation distance, the laser light

is further extinguished by the time it reaches the target. Also, due to the increased propagation distance, time of flight cannot be used to determine the range to a particular scattering event. If the radiative transfer solution from the lidar transmitter to target and back can be obtained, the resulting transmission matrices may be plugged into Eq. (2.1) as $\mathbf{T_{atm}}(\vec{k}_i)$ and $\mathbf{T_{atm}}(\vec{k}_s)$ to account for polarization effects in the propagation medium.

Chapter 3

Scattering Phase Matrix

In most atmospheric sensing applications, the scattering phase matrix contains the information desired for scatterer characterization. For this reason, knowing and understanding the form of the phase matrix is critical, both for understanding what physical information the matrix elements can provide and devising effective techniques for estimating these characteristics.

The number of independent parameters in a scattering matrix depends on what assumptions may be applied to the scattering medium. In the case of randomly oriented, axially symmetric scatterers, the backscatter matrix reduces to one independent term with only a depolarizing effect. Instances of oriented scatterers and multiple scattering will introduce additional independent terms with both retarding and diattenuating effects in addition to depolarization.

3.1 Randomly Oriented Particles

Due to a general lack of orienting forces and common presence of turbulence, the vast majority of particles in the atmosphere are randomly oriented. The volume backscatter coefficient relates the transmitted and total received intensity through the medium properties while, for these randomly oriented scatterers, depolarization gives how that intensity splits between polarization channels.

The scattering phase matrix is a Mueller matrix with elements that are dependent on the incident and scattered wave vectors. When the scattering medium consists of well mixed randomly oriented, axially symmetric scatterers, it is macroscopically isotropic so that the specific incident and scattered wave vectors are no longer uniquely needed to determine the phase matrix. Instead,

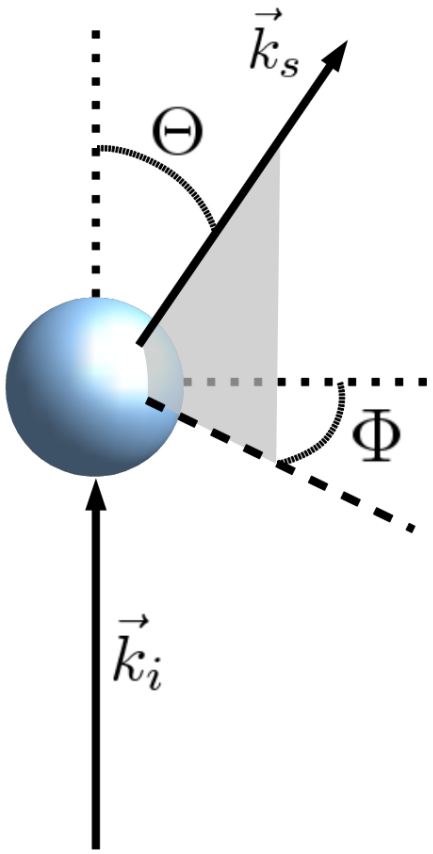

Figure 3.1: Scattering angle definitions for scattering in media that is macroscopically isotropic. The scattering angle Θ is the angle between the incident and scattered wave vectors and Φ is the azimuthal angle of the scattered wave vector in the defined coordinate system.

only the relative angles between the incident and scattered vectors are important. Figure 3.1 shows how the scattering angles Θ and Φ are defined in relation to the incident and scattered wave vectors. The scattering angle Θ is the angle between the two wave vectors, while Φ is an azimuthal scattering angle. Note that under backscattering conditions $\Theta = \pi$ and there is no dependence on Φ. In such cases Φ will be omitted from the argument of the scattering phase matrix. However, in the case of multiple scattering, this angle is an important quantity.

The phase matrix of randomly oriented, axially symmetric scatterers, may be written as a

function of the scattering angle [87]

$$\mathbf{F}(\Theta, \Phi = 0) = \begin{bmatrix} f_{11}(\Theta) & f_{12}(\Theta) & 0 & 0 \\ f_{12}(\Theta) & f_{22}(\Theta) & 0 & 0 \\ 0 & 0 & f_{33}(\Theta) & f_{34}(\Theta) \\ 0 & 0 & -f_{34}(\Theta) & f_{44}(\Theta) \end{bmatrix}. \tag{3.1}$$

If we decompose the above matrix, we find the total backscatter coefficient of the matrix is given by $f_{11}(\Theta)$, $f_{12}(\Theta)$ gives the linear diattenuation, and $f_{34}(\Theta)$ must contain a term related to linear retardance. All other elements may consist of a combination of retarding, diattenuating and depolarizing terms.

Because we assume single scattering we can arbitrarily choose any vector orthogonal to $\vec{k}_i$ from which to measure Φ. Thus for simplicity we choose this axis to lie in the plane with $\vec{k}_i$ and $\vec{k}_s$ so that the $\Phi = 0$. Generally we assume that atmospheric scatterers have axial symmetry. In such cases a particle is its own mirror resulting in a zero value for the (4,1) and (1,4) elements of the phase matrix [87].

Here we consider a monostatic lidar system (co-located transmitter and receiver) so the scattering angle is $\Theta = \pi$. In this case the following relations apply to the elements of the phase matrix[50]:

$$f_{22}(\pi) = -f_{33}(\pi), \tag{3.2}$$

$$f_{12}(\pi) = f_{34}(\pi) = 0, \tag{3.3}$$

$$f_{44}(\pi) = f_{11}(\pi) - 2f_{22}(\pi). \tag{3.4}$$

Applying the relationships in Eq. (3.2), (3.3), and (3.4) for $\Theta = \pi$ to Eq. (3.1) results in the following definition for the normalized backscatter phase matrix exhibited by randomly oriented

scatterers[25]

$$\mathbf{F}(\pi) = \begin{bmatrix} 1 & 0 & 0 & 0 \\ 0 & 1-d & 0 & 0 \\ 0 & 0 & d-1 & 0 \\ 0 & 0 & 0 & 2d-1 \end{bmatrix} \tag{3.5}$$

where d is referred to as the depolarization of the scattering medium. If the incident polarization is linear, d is the fraction of polarized light that is depolarized by the scattering process.

According to Mie theory, when a particle is spherical it does not depolarize in back or forward scattering ($d = 0$) [87]. If the medium is not optically dense (only single scattering occurs) measuring depolarization is an effective indicator of asphericity, refractive index, and size parameter of these particles [50]. This relationship between asphericity and depolarization is the basis of nearly all depolarization measurements in atmospheric lidar. While liquid droplets are very close to spherical, ice is highly aspherical. Thus liquid and solid phase clouds can be categorized by depolarization [16]. The attribute of shape is also shown to be connected to aerosol chemical composition in polar stratospheric clouds [86]. For the purpose of more definitively identifying aerosol make up, the species in question must have unique combinations of backscatter and depolarization. In this way, dust, ice and biological aerosols can be distinguished [71, 73, 45].

3.1.1 T-Matrix Method

For the purpose of simulating small, randomly oriented particles we use the T-Matrix method developed in and provided by [51, 52]. The basic concepts of this algorithm are reviewed here to provide clarity on how these scattering matrices are determined for randomly oriented particles in the Mie regime. Publicly available FORTRAN code is provided by Mishchenko on the web[1] . This code is later applied to simulate polar mesospheric cloud particles in Chapter 6 and determine the expected cloud particle depolarization and backscatter coefficient as a function of incident wavelength.

[1] http://www.giss.nasa.gov/∼crmim

The T-Matrix method is similar to Mie theory. Unlike Mie theory, however, the complex coefficients of the vector spherical wave functions (VSWF) used to describe the the electric field do not necessarily have analytic solutions. For each particle, there exists a matrix which relates the incident and scattered VSWF coefficients. This T-Matrix is determined numerically by equating boundary conditions on the particle.

The incident and scattered electric field of a single particle can be expanded into the vector spherical wave functions (VSWFs) [52]

$$\mathbf{E}^{inc}(\mathbf{R}) = \sum_{n=1}^{\infty} \sum_{m=-n}^{n} \left[a_{mn} Rg\mathbf{M}_{mn}(k\mathbf{R}) + b_{mn} Rg\mathbf{N}_{mn}(k\mathbf{R}) \right], \tag{3.6}$$

$$\mathbf{E}^{sca}(\mathbf{R}) = \sum_{n=1}^{\infty} \sum_{m=-n}^{n} \left[p_{mn} \mathbf{M}_{mn}(k\mathbf{R}) + q_{mn} \mathbf{N}_{mn}(k\mathbf{R}) \right], \tag{3.7}$$

where $\mathbf{M}_{mn}(k\mathbf{R})$ and $\mathbf{N}_{mn}(k\mathbf{R})$ are VSWFs defined in Appendix A, the expressions for $Rg\mathbf{M}_{mn}(k\mathbf{R})$ and $Rg\mathbf{N}_{mn}(k\mathbf{R})$ may be found by substituting the spherical Bessel function j_n for the spherical Hankel function $h_n^{(1)}$ in the respective equations for the $\mathbf{M}_{mn}(k\mathbf{R})$ and $\mathbf{N}_{mn}(k\mathbf{R})$ VSWFs defined in Appendix A, a_{mn} and b_{mn} are the complex VWSF coefficients of the incident field, and p_{mn} and q_{mn} are the complex VWSF coefficients of the scattered field.

When the incident field is a plane wave, the coefficients of the incident field are written [52]

$$a_{mn} = 4\pi(-1)^m i^n d_n \mathbf{C}^*_{mn}(\vartheta^{inc}) \mathbf{E}_0^{inc} \exp(-im\varphi^{inc}), \tag{3.8}$$

$$b_{mn} = 4\pi(-1)^m i^{n-1} d_n \mathbf{B}^*_{mn}(\vartheta^{inc}) \mathbf{E}_0^{inc} \exp(-im\varphi^{inc}), \tag{3.9}$$

where $\mathbf{C}_{mn}$ and $\mathbf{B}_{mn}$ are components of the VSWFs defined in Appendix A, ϑ^{inc} is the zenith angle and φ^{inc} is the azimuthal angle corresponding to the direction of incidence, and $\mathbf{E}_0^{inc}$ is the complex amplitude and polarization of the incident plane wave.

Due to the linearity of Maxwell's equations, the scattered fields may be described by a weighted sum of the incident fields. Thus a transformation matrix (or T matrix), between the incident field coefficients and the resulting scattered field coefficients may be developed. In [52] the

relationship is written

$$\begin{bmatrix} \mathbf{p} \\ \mathbf{q} \end{bmatrix} = \mathbf{T} \begin{bmatrix} \mathbf{a} \\ \mathbf{b} \end{bmatrix} = \begin{bmatrix} \mathbf{T}^{11} & \mathbf{T}^{12} \\ \mathbf{T}^{21} & \mathbf{T}^{22} \end{bmatrix} \begin{bmatrix} \mathbf{a} \\ \mathbf{b} \end{bmatrix} \tag{3.10}$$

which may also be written

$$p_{mn} = \sum_{n'=1}^{\infty} \sum_{m'=-n'}^{n'} \left[T^{11}_{mnm'n'} a_{m'n'} + T^{12}_{mnm'n'} b_{m'n'} \right], \tag{3.11}$$

$$q_{mn} = \sum_{n'=1}^{\infty} \sum_{m'=-n'}^{n'} \left[T^{21}_{mnm'n'} a_{m'n'} + T^{22}_{mnm'n'} b_{m'n'} \right]. \tag{3.12}$$

Note that an exact solution of the scattered field requires an infinite sum over an infinite series of incident field coefficients. In actual application of the T-Matrix method, this sum must be truncated at some value of n'. The number of coefficients required to accurately represent the scattered field depends on the asphericity and size of the particle in relation to the wavelength. Generally particles that are more aspherical or larger require more coefficients.

The sub matrix $\mathbf{T}^{11}$ relates the $Rg\mathbf{M}_{mn}$ modes to the corresponding scattered $\mathbf{M}_{mn}$ modes, $\mathbf{T}^{12}$ describes how $Rg\mathbf{M}_{mn}$ modes couple into $\mathbf{N}_{mn}$ modes, $\mathbf{T}^{21}$ describes how $Rg\mathbf{N}_{mn}$ modes couple into $\mathbf{M}_{mn}$ modes, and $\mathbf{T}^{22}$ relates the $Rg\mathbf{N}_{mn}$ modes to the corresponding scattered $\mathbf{N}_{mn}$ modes.

Since we are observing the scattered electric fields in the far field, we make the large argument approximation for the spherical Hankel function to obtain an expression for the scattering amplitude matrix[52].

$$\begin{aligned} \mathbf{S}(\mathbf{n^{sca}}, \mathbf{n^{inc}}) &= \frac{4\pi}{k} \sum_{mnm'n'} i^{n'-n-1} (-1)^{m+m'} d_n d_{n'} \exp\left[i(m\varphi^{sca} - m'\varphi^{inc}) \right] \\ &\times \quad \{ \left[T^{11}_{mnm'n'} \mathbf{C}_{mn}(\vartheta^{sca}) + T^{21}_{mnm'n'} i\mathbf{B}_{mn}(\vartheta^{sca}) \right] \mathbf{C}^{*}_{m'n'}(\vartheta^{inc}) \\ &+ \quad \left[T^{12}_{mnm'n'} \mathbf{C}_{mn}(\vartheta^{sca}) + T^{22}_{mnm'n'} i\mathbf{B}_{mn}(\vartheta^{sca}) \right] \mathbf{B}^{*}_{m'n'}(\vartheta^{inc})/i \}. \end{aligned} \tag{3.13}$$

where $\mathbf{S}$ is the amplitude scattering matrix, $\mathbf{n^{sca}}$ and $\mathbf{n^{inc}}$ are the unit vectors denoting the directions of scatter and incidence respectively.

The amplitude scattering matrix is a Jones matrix that relates the incident and scattered electric field for a particular incident and scattered k vector. Obtaining the phase matrix or Mueller matrix of the individual particle, which relates the incident and scattered intensity then becomes

relatively simple once the amplitude matrix is obtained. Here only the parameters relevant for the backscatter case are shown (see Eq. (3.50) or [52] Chapter 1 for total equations relating elements of the phase and amplitude matrices)

$$f_{11}^p = \frac{1}{2}\left(|S_{11}|^2 + |S_{12}|^2 + |S_{21}|^2 + |S_{22}|^2\right) \tag{3.14}$$

$$f_{22}^p = \frac{1}{2}\left(|S_{11}|^2 - |S_{12}|^2 - |S_{21}|^2 + |S_{22}|^2\right) \tag{3.15}$$

$$f_{33}^p = Re\left(S_{11}S_{22}^* + S_{12}S_{21}^*\right) \tag{3.16}$$

$$f_{44}^p = Re\left(S_{22}S_{11}^* - S_{12}S_{21}^*\right). \tag{3.17}$$

where f_{mn}^p and S_{mn} are the *mth* and *nth* terms in the particle scattering phase and amplitude matrices respectively.

If the scattering medium consists of randomly oriented particles, the total phase matrix is the average of the single particle phase matrix over all possible orientations. In this process, retarding and diattenuating terms average out and so the only remaining polarization effect is depolarization.

$$\mathbf{F}(\Theta) = \int_0^{2\pi}\int_0^{\pi}\int_0^{2\pi} \mathbf{F^P}(\Theta,\alpha,\beta,\gamma)d\alpha\sin\beta d\beta d\gamma \tag{3.18}$$

where α, β, and γ are the angles of orientation for the particle in a lab frame. In practice however, this integration is computationally intensive, as the phase matrix must be recalculated for each step of integration. The T-matrix, however, need only be rotated by the respective angles. Thus the T-matrix of the particulate constituents should be averaged over all orientations.

Any one element in the average T-matrix becomes [52]

$$\left\langle T_{mnm'n'}^{kl}\right\rangle = \frac{1}{8\pi^2}\int_0^{2\pi} d\alpha \int_0^{\pi} d\beta\sin\beta\int_0^{2\pi} d\gamma T_{mnm'n'}^{kl}(\alpha,\beta,\gamma) \tag{3.19}$$

where α, β, and γ are the angles representing the particle's orientation relative to the lab frame. We can then take advantage of an orthogonality property of the Wigner D functions[88] that make up the T-matrix elements (see Appendix A for Wigner D function definition and Chapter 6 in

[52] for a derivation of T-matrix orthogonality) to determine the orientationally averaged T-matrix without the requirement of full numerical integration

$$\left\langle T^{kl}_{mnm'n'} \right\rangle = \frac{1}{2n+1}\delta_{mm'}\delta_{nn'} \sum_{m_1=-n}^{n} T^{kl}_{m_1nm_1n} \tag{3.20}$$

where $T^{kl}_{m_1nm_1n}$ has no argument because it is defined in the particle's reference frame. The process of determining the phase matrix from the orientationally averaged T-matrix requires several intermediate coefficients to obtain the final result. These steps offer little insight for understanding scattering by nonspherical particles and have been omitted. Readers interested in algorithms for orientation averaging of axially symmetric scatterers are referred to [49].

3.2 Oriented Particles

Though randomly oriented scatterers are common, ice crystals are known to orient due to drag forces overcoming the forces of Brownian motion in the atmosphere [69]. These occurrences can sometimes be identified visually by the presence of sun dogs and sun pillars, which are only observable under conditions where scatterers have a preferential orientation. These oriented ice crystals are known to have different radiative transfer properties from their randomly oriented counterparts [17, 83]. More extensive data is needed on the occurrence frequency of such clouds and the conditions under which they form for accurate climate modeling.

The scattering matrix of oriented scatterers is fundamentally different from that of randomly oriented particles. While randomly oriented scatterers are strictly depolarizing, oriented particles, due to their common geometry also have diattenuating and retarding effects. Thus, by observing the different polarization properties of the atmosphere, we can identify the presence of oriented scatterers.

3.2.1 Oriented Scattering Matrix

Unlike their randomly oriented counterparts, oriented scatterers may exhibit a variety of polarization effects under backscattering conditions. The backscatter matrix of horizontally oriented

scatterers, such as those sometimes observed in cirrus clouds has the form [39]

$$\mathbf{F}(\vec{k}_i, -\vec{k}_i) = \begin{bmatrix} f_{11} & f_{12} & 0 & 0 \\ f_{12} & f_{22} & 0 & 0 \\ 0 & 0 & f_{33} & f_{34} \\ 0 & 0 & -f_{34} & f_{44} \end{bmatrix}, \tag{3.21}$$

where the scattering medium is not macroscopically isotropic so the backscattering matrix is a function of the incident wave vector. The scattering matrix shown above has the same form as Eq. (3.1) for randomly oriented particles of arbitrary scattering angle. The distinction here is that the backscatter matrix of oriented particles does not simplify to the diagonalized depolarizing matrix in Eq. (3.5).

The scattering matrix in Eq. (3.21) applies to any oriented scatterer including platelets, columns or bullets. If we assume particles will orient within the horizontal plane and the lidar is pointing along zenith/nadir ($\vec{k}_i$ is parallel to the vertical z-axis), scattering symmetry between all polarization planes gives a scattering matrix that simplifies to the depolarizing form in Eq. (3.5). In this case there is no distinction between the phase matrix form representing horizontally oriented scatterers and randomly oriented scatterers.

For a geometric representation of a tilted lidar with horizontally oriented scatterers, see Figure 3.2. The scatterers are aligned with the horizontal plane depicted. In this work, all linear polarization angles, ϕ_f, are measured with reference to the s-polarization (the linear polarization that is in the horizontal plane). The directional cosine between the vertical z-axis and the incident wave vector $\vec{k}_i$ is the lidar tilt angle α.

With the scattering matrix expressed in Eq. (3.21), the circular polarization ratio takes the form

$$\delta_c = \frac{f_{11} - f_{44}}{f_{11} + f_{44}}. \tag{3.22}$$

An arbitrary linear transmit polarization is described

$$\vec{S}_{TX} = S_0 \begin{bmatrix} 1 & \cos 2\phi_f & \sin 2\phi_f & 0 \end{bmatrix}^T \tag{3.23}$$

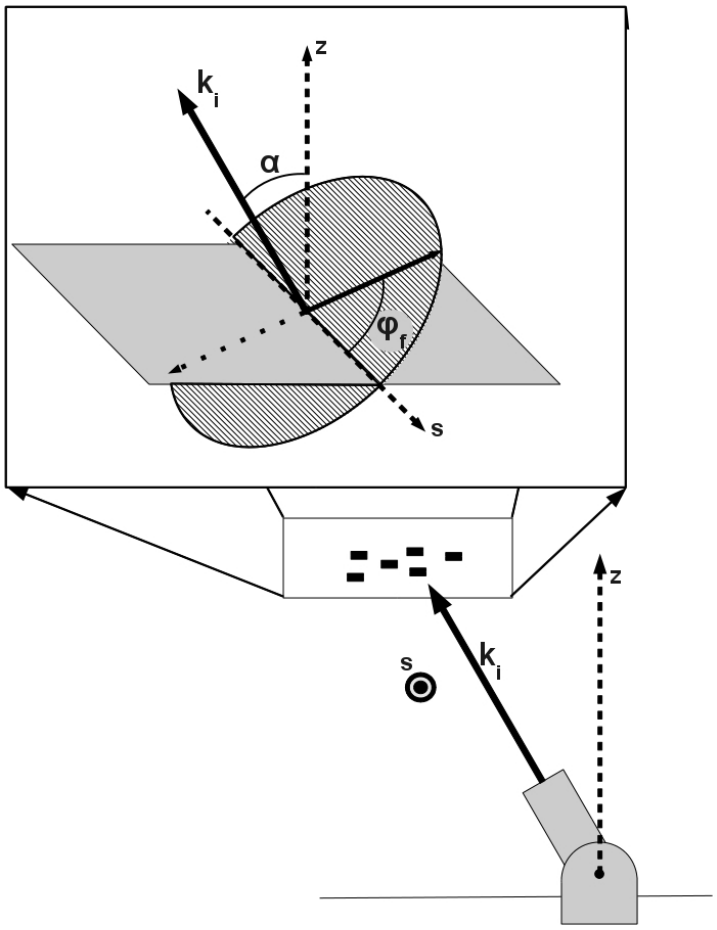

Figure 3.2: Graphical depiction of angular terms for scatterers oriented in the horizontal plane. The lidar tilt angle α is measured relative to zenith (z axis) and the polarization angle ϕ_f is measured relative to the linear polarization that lies in the horizontal plane (s axis).

where S_0 is the total transmitted intensity and ϕ_f is the transmitted linear polarization angle measured with respect to the s-polarization in the horizontal. Polarizers in the receiver are rotated according to the transmit polarization angle to measure parallel and perpendicular signals.

Using Eq. (2.11), (3.21) and (3.23), the linear polarization ratio is a function of several elements in the phase matrix, the angle ϕ_f and is given as

$$\delta_l = \frac{f_{11} - f_{22}\cos^2 2\phi_f - f_{33}\sin^2 2\phi_f}{f_{11} + 2f_{12}\cos 2\phi_f + f_{22}\cos^2 2\phi_f + f_{33}\sin^2 2\phi_f}. \tag{3.24}$$

Note that the linear polarization ratio is a function of linear diattenuation (f_{12}) and possible retarding and depolarizing terms (f_{33} and f_{22}) [42]. Also, the circular polarization ratio may contain depolarizing and retarding terms (f_{44}). Thus, although δ is often referred to as the "depolarization ratio", in the case of oriented scatterers, it is not necessarily related to the scatterer's effect on the degree of polarization.

A notable conclusion from Eq. (3.22) and (3.24) is that the polarization ratio does not make any distinction between scattering matrix types. Nor can it distinguish polarization effects exhibited by the matrix. It only allows us to determine if the polarization changed. Where with randomly oriented scatterers, the depolarization ratio is only dependent on the ellipticity of the the incident and detected polarizations, oriented scatterers also give dependence on the lidar's linear polarization plane, ϕ_f. Though sometimes useful, the polarization ratio becomes an ambiguous term in the presence of variation in scattering properties and incident polarization.

Unlike randomly oriented particles, the behavior of the oriented backscatter matrix cannot be attributed to any single polarization effect. However, we can apply Lu-Chipman Mueller decomposition to the matrix in Eq. (3.21) to determine how different polarization effects contribute to the scattering matrix terms [42]. This means that the scattering phase matrix must be composed of a combination of diattenuating, retarding and depolarizing terms

$$\mathbf{F}(\vec{k}_i, -\vec{k}_i) = f_{11}\mathbf{M}_\Delta^F\mathbf{M}_R^F\mathbf{M}_D^F, \tag{3.25}$$

where f_{11} denotes that all decomposed matrices are normalized and $\mathbf{M}_\Delta^F$, $\mathbf{M}_R^F$, and $\mathbf{M}_D^F$ are the depolarizing, retarding and diattenuating matrices of the backscatter phase matrix. Comparing the

form of the scattering matrix in Eq. (3.21) to that shown in Eq. (2.6), we see that the retarding and diattenuating axes are aligned (f_{12} corresponds to diattenuation between s- and p-polarizations, f_{34} corresponds to retardance with s- and p-polarization axes). Thus, by applying the matrix forms in Eq. (2.2) and (2.3), the scatterer diattenuation matrix is given by

$$\mathbf{M}_D^F = \begin{bmatrix} 1 & f'_{12} & 0 & 0 \\ f'_{12} & (1-f'_{12})\sqrt{1-{f'_{12}}^2}+f'_{12} & 0 & 0 \\ 0 & 0 & \sqrt{1-{f'_{12}}^2} & 0 \\ 0 & 0 & 0 & \sqrt{1-{f'_{12}}^2} \end{bmatrix}, \tag{3.26}$$

where f'_{12} is the normalized (1,2) element of the scattering matrix and also its diattenuation.

The retarder component of the scattering matrix is then given by Eq. (2.4) and (2.5) of a linear wave plate with axes along s- and p-polarizations. The matrix evaluates to

$$\mathbf{M}_R^F = \begin{bmatrix} 1 & 0 & 0 & 0 \\ 0 & 1 & 0 & 0 \\ 0 & 0 & \cos\Gamma_F & -\sin\Gamma_F \\ 0 & 0 & \sin\Gamma_F & \cos\Gamma_F \end{bmatrix}, \tag{3.27}$$

where Γ_F is the phase shift imposed by the scatterer's retarding matrix.

The diattenuation and retardance matrix combine to define a homogeneous scattering matrix. In the presence of a single scatterer, there is no depolarizing effect. However, because the volume matrix is typically a sum of several scattering matrices, depolarizing effects must generally be included. The depolarization matrix from Eq. (2.8) can be reduced to contain five independent terms. In order to maintain symmetry between the (1,2) and (2,1) terms, polarizance must exist along s- or p-polarizations. This means the (2,1) element of the depolarization matrix is not necessarily zero. Because depolarization within a volume is caused by distributed orientation about a mean, depolarization in s- and p-polarizations is caused by canceling diattenuation terms. The volume phase matrix in Eq. (3.21) contains no coupling terms between s- and p-polarizations and the other two Stokes elements. As a result, there is no cross coupling between these terms in the

depolarization matrix and $[\ 1 \quad 0 \quad 0\ ]^T$ must be an eigenvector of $\mathbf{m}_\Delta$. There is, however, cross coupling in Eq. (3.21) between the circular and $\pm 45^\circ$ Stokes vector terms, so we must account for this possibility in the assumed form of the depolarization matrix. This results in symmetric, non-zero (3,4) and (4,3) elements in the depolarization matrix. Thus the general assumed form of the depolarization matrix becomes

$$\mathbf{M}_\Delta^F = \begin{bmatrix} 1 & 0 & 0 & 0 \\ P_1 & 1-d_1 & 0 & 0 \\ 0 & 0 & 1-(d_3 - d_x\cos^2\theta_x) & \frac{d_x}{2}\sin 2\theta_x \\ 0 & 0 & \frac{d_x}{2}\sin 2\theta_x & 1-(d_2 + d_x\cos^2\theta_x) \end{bmatrix}, \tag{3.28}$$

where P_1 is the polarizance of the depolarization matrix along s- and p-polarizations, d_1 is the depolarization of along s- and p-polarizations, d_2 is the depolarization along the eigenvector closest to $\pm 45^\circ$, d_3 is the depolarization along the eigenvector closest to circular polarizations, and θ_x is the angle in Poincaré space between the eigenvectors of $\mathbf{m}_\Delta$ and the basis vectors along $\pm 45^\circ$ and circular polarizations. Thus when θ_x is not an integer multiple of zero or π, there are depolarization cross talk terms. Finally d_x is a depolarization cross talk term that is strictly a function of the other depolarizations and is given by

$$d_x = d_3 - d_2. \tag{3.29}$$

By evaluating Eq. (3.25) and imposing the symmetry requirement between the (1,2) and (2,1) elements exhibited by the total volume phase matrix in Eq. (3.21), we find the polarizance in Eq. (3.28) is not independent and is given as

$$P_1 = d_1 f'_{12}. \tag{3.30}$$

We then also apply the requirement for antisymmetry between the (3,4) and (4,3) elements ($f_{34} = -f_{43}$) shown in (3.21). By imposing this requirement, we find that the angle of the eigen axes in the depolarizer θ_x has a simple relation to the retardance of the scattering matrix Γ_F given by

$$\theta_x = \frac{\Gamma_F}{2}. \tag{3.31}$$

The volume scattering phase matrix given in Eq. (3.21) for oriented scatterers has six independent terms. Thus, Lu-Chipman Mueller decomposition also gives six independent terms corresponding to physical polarization effects: f_{11} (related only to backscatter intensity), f'_{12}, Γ_F, d_1, d_2, and d_3.

3.2.2 Geometric Scattering of Hexagonal Ice Crystals

Owing to the large size of oriented ice crystals (on the order of $100\mu m$), T-Matrix calculations will not converge without very high orders of VWSF complex coefficients. Instead we must use geometric scattering calculations to simulate the properties of these scatterers. This is done by breaking up an incident plane wave (PW) into small, finite elements, ray tracing them in the crystal geometry, then diffracting the outgoing PW element to evaluate the resulting electric field on the detector [92]. The PW elements must be large enough so diffraction is negligible within the crystal. After exiting the crystal, diffraction is included in propagating back to the detector. The total electric field observed by the detector is then the sum of all electric fields ray traced from the incident PW. For simplicity, the detected electric field is most easily described in a common lab frame, avoiding the need to track the relative transformations between local coordinate frames such as those used in Jones vectors. This process of ray tracing in a 3-dimensional coordinate frame is called polarization ray tracing (PRT) [18] and greatly simplifies the process of summing electric field components from each PW element. The corresponding 3x3 matrix for PRT is thus called the PRT matrix.

The PW element starts with a wave vector $\hat{k}_i$ along the z-axis at (x_n, y_n, z_0) where x_n and y_n are the x-y coordinates of the nth PW element and z_0 is the initial starting position of the wave along the z-axis. We then determine the next crystal face the ray will intersect by calculating the distance to intersection of each surface. The closest surface of intersection is the next interface. The position of the ray is then updated to the point of intersection between the crystal face and ray. The polarization effects of reflection or transmission are imposed on the ray. These effects are given by Fresnel coefficients [14]. Fresnel coefficients, however, are defined in the basis set of s- and

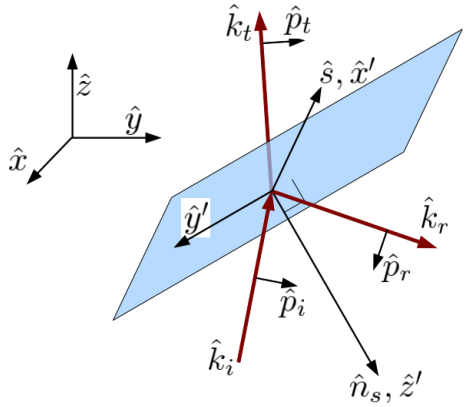

Figure 3.3: Graphical depiction of the coordinate frames used in this polarization ray tracing (PRT) discussion. The lab frame xyz is independent of the interface, the interface frame $x'y'z'$ is determined by the surface normal and s-polarization (as convention), and the Fresnel frames are dictated by the corresponding wave vector, s- and p-polarizations. The Fresnel frames are broken up by incident sp_ik_i, reflected sp_rk_r and transmitted frames sp_tk_t.

p-polarizations incident on the surface (see Figure 3.3 for a graphical description of the coordinate frames used for polarization ray tracing of a surface interface). Thus the polarization ray tracing matrix for reflection in the Fresnel coordinate frame is given by [18]

$$\mathbf{R}^{\mathbf{f}}_{\mathbf{F}}(\theta_F) = \begin{bmatrix} r_s(\theta_F) & 0 & 0 \\ 0 & r_p(\theta_F) & 0 \\ 0 & 0 & 0 \end{bmatrix}, \tag{3.32}$$

where the superscript F denotes that the matrix is in the Fresnel coordinate frame, θ_F is the angle of incidence, r_s is the complex s-polarized reflection coefficient and r_p is the complex p-polarized reflection coefficient. The transmission PRT matrix is identical to that of reflection, where the transmission coefficients t_s and t_p are substituted for the reflection coefficients. The transmission matrix is then $\mathbf{T}^{\mathbf{f}}_{\mathbf{F}}(\theta_F)$. Note that θ_F is related to the dot product of the incident ray and the surface normal

$$\cos\theta_F = \hat{k}_i \cdot \hat{n}_s. \tag{3.33}$$

Because the polarization in Fresnel coefficients is defined by s- and p-polarizations, we must perform a transformation between the lab x-y-z coordinate frame and the interface coordinate frame. The

transformation matrix from the lab frame to the incident Fresnel frame is given by

$$\mathbf{Q_1} = \begin{bmatrix} \hat{s}^T \\ \hat{p}_i^T \\ \hat{k}_i^T \end{bmatrix}, \tag{3.34}$$

where $\hat{s}$ is the normalized vector of s-polarization in the lab frame and given by the cross product between the incident ray and surface normal

$$\hat{s} = \frac{\hat{k}_i \times \hat{n}_s}{|\hat{k}_i \times \hat{n}_s|}, \tag{3.35}$$

$\hat{p}_i$ is the p-polarization vector for the incident ray in the lab frame given by

$$\hat{p}_i = \frac{\hat{k}_i \times \hat{s}}{|\hat{k}_i \times \hat{s}|}, \tag{3.36}$$

and ^{T} denotes a transpose operation.

The transformation matrix from the reflected or transmitted ray back into the lab frame is then given by

$$\mathbf{Q_{2r,t}} = \begin{bmatrix} \hat{s} & \hat{p}_{r,t} & \hat{k}_{r,t} \end{bmatrix}, \tag{3.37}$$

where all vectors are again written in the lab frame and $\hat{p}_{r,t}$ is the vector description of the outgoing p-polarization for reflection or transmission and $\hat{k}_{r,t}$ is the outgoing ray direction for reflection or transmission. For reflection, the outgoing ray is determined by converting to the interface frame ($x'y'z'$ where z' is along the surface normal), negating the resulting z component of the ray, and returning to the lab frame

$$\hat{k}_r = \mathbf{Q_{x'y'z'}}^{-1} \begin{bmatrix} 1 & 0 & 0 \\ 0 & 1 & 0 \\ 0 & 0 & -1 \end{bmatrix} \mathbf{Q_{x'y'z'}}, \tag{3.38}$$

Where $\mathbf{Q_{x'y'z'}}$ is the transformation matrix from the lab to interface frame and given by

$$\mathbf{Q_{x'y'z'}} = \begin{bmatrix} \hat{s}^T \\ \hat{y'}^T \\ \hat{n}_s^T \end{bmatrix}. \tag{3.39}$$

The selection of the x' and y' vectors are arbitrary, but by convention x' is chosen to align to the s-polarization so that y' is given by

$$\hat{y'} = \frac{\hat{n}_s \times \hat{s}}{|\hat{n}_s \times \hat{s}|}. \tag{3.40}$$

If we are considering transmission, the ray will refract. Again, the operation is most easily performed in the interface frame so we obtain

$$\vec{k}'_t = \begin{bmatrix} k_{ix'} \\ k_{iy'} \\ \sqrt{\left(\frac{n_t}{n_i}\right)^2 |\hat{k_i}|^2 - (k_{ix'})^2 - \left(k_{iy'}\right)^2} \end{bmatrix}, \tag{3.41}$$

where the subscript x' denotes the component along the x'-axis in the interface frame, n_i is the index of refraction in the incident medium and n_t is the index of refraction in the transmitted medium. Note that in Eq. (3.41) the transmitted ray vector in the interface coordinate frame is not normalized.

With the outgoing ray direction determined, we can then obtain the outgoing p-polarization, again using cross products

$$\hat{p}_{r,t} = \frac{\hat{k}_{r,t} \times \hat{s}}{|\hat{k}_{r,t} \times \hat{s}|}. \tag{3.42}$$

The reflection PRT matrix description of an interface is then described

$$\mathbf{R_F}(\hat{k}_i, \hat{n}_s) = \mathbf{Q_2} \mathbf{R_F^f}(\theta_\mathbf{F}) \mathbf{Q_1}. \tag{3.43}$$

The total path of the PW element is then described by the product of all PRT matrices along the ray path. For all instances other than the first reflection off crystal face this is given by

$$\mathbf{P}^N = \mathbf{T_F}(\hat{k}_i^N, \hat{n}_s^N) \left(\prod_{n=2}^{N-1} \mathbf{R_F}(\hat{k}_i^n, \hat{n}_s^n) \right) \mathbf{T_F}(\hat{k}_i^1, \hat{n}_s^1), \tag{3.44}$$

where the superscript denotes the interface interaction number for the particular PW element and N is the total number of interfaces observed by the PW element.

To determine how the outgoing electric field maps onto the detector we diffract the electric field [92]. For simplicity, we assume the square elements may be approximated as circular for

diffraction calculations [92]. The PW element is much smaller than the propagation distance to the lidar, so the Fraunhofer approximation may be applied [28]. The observed PRT matrix is then given by [92]

$$\mathbf{P}_d^N = \Delta\sigma_p \frac{2J_1\left[|\vec{k}_N|(\Delta\sigma_p/\pi)^{\frac{1}{2}}\sin\theta_d\right]}{|\vec{k}_N|(\Delta\sigma_p/\pi)^{\frac{1}{2}}\sin\theta_d}\mathbf{Q_d}(\hat{r}_d,\hat{k}_N)\mathbf{P}^N, \tag{3.45}$$

where $\Delta\sigma_p$ is the area of the PW element, J_1 is the first-order Bessel function, $\vec{k}_N$ is the outgoing wave vector from the last surface, $\hat{r}_d$ is the scattering direction (vector pointing to the detector), θ_d is the angle between the outgoing wave vector and $\hat{r}_d$, $\mathbf{P}^N$ is polarization ray tracing matrix for the outgoing ray and given by Eq. (3.44) and $\mathbf{Q_d}(\hat{r}_d,\hat{k}_N)$ is the transformation matrix accounting for the fact that the electric field must be orthogonal to the wave vector after diffraction. This matrix is similar to the transformation matrices into the Fresnel interface and is given by

$$\mathbf{Q_d}(\hat{r}_d,\hat{k}_N) = \begin{bmatrix} \hat{s}_d & \hat{p}_d & \hat{r}_d \end{bmatrix} \begin{bmatrix} \hat{s}_d^T \\ \hat{p}_N^T \\ \hat{k}_N^T \end{bmatrix}, \tag{3.46}$$

where the vectorial components are given by

$$\hat{s}_d = \frac{\hat{k}_N \times \hat{r}_d}{|\hat{k}_N \times \hat{r}_d|}, \tag{3.47}$$

$$\hat{p}_N = \frac{\hat{k}_N \times \hat{s}_d}{|\hat{k}_N \times \hat{s}_d|}, \tag{3.48}$$

and

$$\hat{p}_d = \frac{\hat{r}_d \times \hat{s}_d}{|\hat{r}_d \times \hat{s}_d|}. \tag{3.49}$$

The total electric field observed by the detector is then related to the incident field through the sum of all PW element PRT matrices obtained in Eq. (3.45). The amplitude scattering (Jones) matrix of the crystal is defined for a 2D coordinate frame normal to the wave vector. Because we are considering only backscatter, the scattering wave vector points along the z-axis. The amplitude matrix is thus given by the 2x2 block in the upper left corner of the PRT. This complex amplitude matrix can then be converted to a phase matrix using standard Jones to Mueller matrix relations

given by [19]

$$\mathbf{M} = \mathbf{U}\left(\mathbf{J} \otimes \mathbf{J}^{*}\right)\mathbf{U}^{-1}, \tag{3.50}$$

were $\mathbf{M}$ is the Mueller matrix corresponding to the Jones matrix $\mathbf{J}$, $\otimes$ represents the tensor product and $\mathbf{U}$ is the Jones/Mueller transformation matrix given [19]

$$\mathbf{U} = \begin{bmatrix} 1 & 0 & 0 & 1 \\ 1 & 0 & 0 & -1 \\ 0 & 1 & 1 & 0 \\ 0 & i & -i & 0 \end{bmatrix} = \left(\mathbf{U}^{-1}\right)^{\dagger}. \tag{3.51}$$

.

3.3 Multiple Scattering by Spherical Particles

When scatterers have sufficiently high scattering cross section and number density, incident laser light may be scattered more than once before exiting the scattering medium. This process of multiple scattering will cause the laser light to diffuse radially through the medium (away from the beam). Also, due to multiple forward and backward scattering events, time-of-flight may not be able to provide accurate range information. For this reason, optically dense clouds frequently have profiles that decay in range, past the physical dimension of the cloud.

It is well understood that polarization effects of multiple scattering are dependent on the lidar's field-of-view (FOV). For very narrow FOV, only forward and backward scattering events are detected. So if the cloud consists of spherical droplets, no total depolarizing effect is observed. By contrast, a wide FOV observing multiple scattering sees a depolarizing effect described by the depolarizing phase matrix in Eq. (3.5)'[65]. While both of these descriptions of multiple scattering are true, they gloss over the complexities of multiple scattering.

For a well mixed scattering medium, the total phase matrix describing a multiply scattered path becomes the product of the average single scattering matrix at each scattering angle

$$\mathbf{F} = \prod_{n=1}^{N} \mathbf{F}_{\mathbf{s}}(\Theta_n, \Phi_n), \tag{3.52}$$

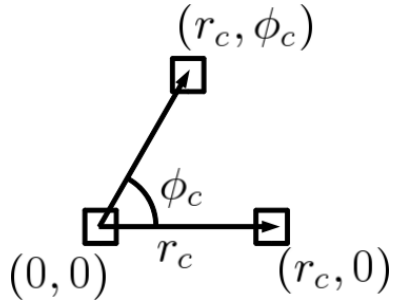

Figure 3.4: Image plane of camera recording multiple scattering patters. The (0,0) pixel corresponds to the transmitted beam, so it is the only pixel containing first order scattering returns. All pixels of equal radius r_c have, within a rotation, the same scattering matrix.

where $\mathbf{F_s}(\Theta_n, \Phi_n)$ is the single scattering phase matrix of the medium at the nth scattering angles Θ_n, the angle between the incident wave vector and scattered wave vector, and Φ_n, the azimuthal scattering angle (See Figure 3.1) and N is the the total number of scattering events.

It has been found in multiply scattered simulations and measurements that forward and back scattering peaks are substantially stronger than radially scattered directions [62]. For this reason, scattering with order higher than 2 are only weakly contributing to the received radiation patterns and polarization. These higher order terms have been shown to only smooth the cusps of the received patterns [15]. For this reason, we will only focus on second order scattering in this work.

If, instead of using a single detector, we were to focus the scattering patterns onto a camera, each pixel would measure a unique phase matrix defined by the total sum of scattering events imaged onto the pixel. Let a pixel at radius r_c from the center of the intensity pattern, along the x-axis (see Figure 3.4), observe the scattering matrix $\mathbf{F}(r_c, 0)$. If the medium is macroscopically isotropic, by argument of symmetry, another pixel at the same radius r_c, but at angle ϕ_c to the x-axis, must be related to the first pixel by a rotation matrix

$$\mathbf{F}(r_c, \phi_c) = \mathbf{R}(\phi_c)\mathbf{F}(r_c, 0)\mathbf{R}(-\phi_c), \tag{3.53}$$

where $\mathbf{R}(\phi)$ is a rotation matrix of angle ϕ. Thus for a constant value of r_c, the fundamental elements of the scattering matrix are identical.

In its most general form, the scattering matrix of each pixel will have sixteen independent

elements. However for the purpose of this discussion, let us assume the probability of scattering in the volume remains much less than 1, so that second order scattering effects dominate the multiply scattered return. The form of the scattering matrix for each pixel along the x-axis is then the same as that in Eq. (3.21) where the matrix for all pixels off the x-axis may be determined using Eq. (3.53).

When we integrate the backscatter matrix $\mathbf{F}(r_c, \phi_c)$ over all ϕ_c, the total phase matrix at each radius has no off diagonal elements thus making it strictly depolarizing. For each off diagonal element in the scattering matrix, there exists another angle, where the same element is equal and opposite in sign. Thus when we sum over all the diattenuating and retarding effects in the FOV (as with a single detector), their net polarization effects cancel, and only appear as depolarization. Though each individual pixel may observe diattenuating and retarding effects in multiply scattered returns, the total integrated field still conforms to the depolarizing matrix in Eq. (3.5).

3.3.1 Simulation of Second Order Scattering Radiation Patterns

If a single pulse is transmitted through an optically dense medium, we can calculate the backscattered radiation pattern from second order scattering recorded by a camera. The center pixel of the camera is assumed to contain the single scattered and multiply forward and backscattered returns. On each other pixel, the scattering matrix can be determined by integrating over all second order ray paths allowed by the detector integration time.

Let the range to the first scattering event be R_s (see Figure 3.5). The first scattering event occurs at the angle Θ_1, after which the scattered light propagates a distance ΔR_1 before it is scattered by a second particle at the angle Θ_2. Assuming $R_s \gg \Delta R_1 \sin\Theta_1$ the sum of the scattering angles must be 180° for the light to be received by the lidar.

$$\Theta_1 + \Theta_2 = \pi. \tag{3.54}$$

In addition to the attenuation observed in single scattering, there is also loss due to the additional propagation lengths ΔR_1 and ΔR_2 in the scattering volume. Thus the backscatter phase matrix

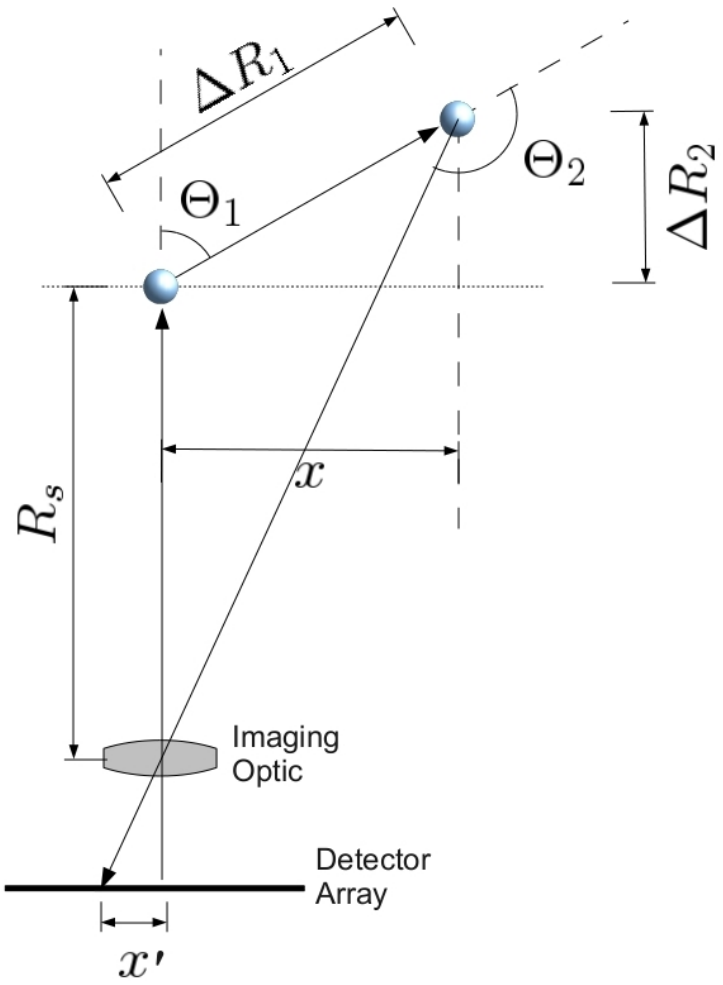

Figure 3.5: Relevant geometric parameters for calculating second order scattering in a medium. It is assumed that $R_s \gg x$ so that $\Theta_1 + \Theta_2 \approx 180°$. The transverse displacement of the second scattering event, x, is mapped onto the image plane by the detector optic with some transverse displacement x' where $x' = Mx$ and M is the magnification of the imaging system.

of an individual optical path from second order scattering is

$$\mathbf{F_2}(\pi) = \frac{R_s^2}{\Delta R_1^2(\Delta R_2 + R_s)^2} \exp\left[-\kappa(\Delta R_1 + \Delta R_2)\right] \mathbf{F_1}(\Theta_2)\mathbf{F_1}(\Theta_1), \tag{3.55}$$

where $\mathbf{F_2}(\pi)$ is the second order backscatter phase matrix of the path, $\mathbf{F_1}(\Theta)$ is the first order scattering matrix of the particles in the medium for a scattering angle Θ and κ is the extinction of the medium given by

$$\kappa = \int_0^\infty \sigma_e(r_p) n_d(r_p) dr_p, \tag{3.56}$$

where $n_d(r_p)$ is the number density of particles of radius r_d and $\sigma_e(r_d)$ is the corresponding extinction coefficient of the particles related to the scattering phase matrix of a single particle by

$$\sigma_e(r_d) = \sigma_a(r_d) + \int_0^{2\pi} \int_0^{\pi} f_{11}^p(\Theta, \Phi, r_d) \sin\Theta d\Theta d\Phi, \tag{3.57}$$

where $\sigma_a(r_d)$ is the absorption cross section of the particle of radius r_d and f_{11}^p is the (1,1) element of the scattering phase matrix of a single particle $\mathbf{F^P}$.

The scattering paths we must integrate for a single pixel are dictated by the detection integration time ΔT_D. The following condition must be satisfied for a second order scattering effect to be registered in the same time bin as the single scattered return

$$\Delta T_D > \frac{\Delta R_1 + \Delta R_2}{c}. \tag{3.58}$$

From the geometry shown in Figure 3.5 we obtain

$$\Delta R_2 = \Delta R_1 \cos\Theta_1, \tag{3.59}$$

which allows us to rewrite the above condition to give the integration limits as a function of the first scattering angle and path length

$$\Delta R_1(1 + \cos\Theta_1) > c\Delta T_D. \tag{3.60}$$

The transverse displacement of the the resulting backscattered light is

$$x = \sin\Theta_1. \tag{3.61}$$

If $c\Delta T_D \ll R_s$ or the depth of the scattering medium is much less than R_s, this transverse displacement means the total backscatter angle is slightly off 180° for light collected by the receiver. When focused by an imaging lens, the backscatter angle is imaged onto a transverse displacement in the detector plane. Thus, the transverse displacement of the second scattering event proportionally maps to an off axis pixel on the detector. We can then write the integration limits in terms of x and Θ_1

$$\frac{1}{\sin\Theta_1} + \frac{1}{\tan\Theta_1} < \frac{c\Delta T_D}{x}. \tag{3.62}$$

The inequality above is transcendental when solving for Θ_1, so no analytic solution exists. However, this equation is easily solved numerically. Let Θ_1^M be the maximum value of Θ_1 that satisfies the above inequality.

We can then use the solution to Eq. (3.62) and previously defined relations in Eq. (3.54), (3.55), (3.59) and (3.61) to write the total backscatter phase matrix observed by a pixel corresponding to transverse displacement x

$$\mathbf{F_2}(x,\pi) = \int_{-\Theta_1^M}^{\Theta_1^M} \frac{R_s^2 \sin^2\Theta_1}{x^2(R_s + x\cot\Theta_1)^2} \exp\left(-\kappa x \frac{1+\cos\Theta_1}{\sin\Theta_1}\right) \mathbf{F_1}(\pi-\Theta_1)\mathbf{F_1}(\Theta_1) d\Theta_1. \tag{3.63}$$

The matrix $\mathbf{F_2}$ may then be used as the scattering phase matrix in the SVLE to solve for the expected receive polarization and photon counts.

The matrix calculation in Eq. (3.63) gives the scattering matrix along one transverse displacement axis x. This axis corresponds to the azimuthal angle $\phi_c = 0$. However, once all matrices along the x-axis are determined, Eq. (3.53) can be used to determine the phase matrix observed by pixels of arbitrary ϕ_c.

We now simulate the recorded backscattered intensity patterns on a camera with a polarizer using the SVLE. Mie theory is used to determine the single scattering matrix of a spherical particle and the second order scattering matrix of each pixel is determined using Eq. (3.63). The parameters for simulation are matched to experimental data recorded by [58] using a 633 nm source. The two simulations shown use particles of radius $0.085\mu m$ and $0.75\mu m$ and index of refraction of 1.3. The range bin is assumed to be large so that Θ_1^M approaches π. In all Figures, the incident polarization is

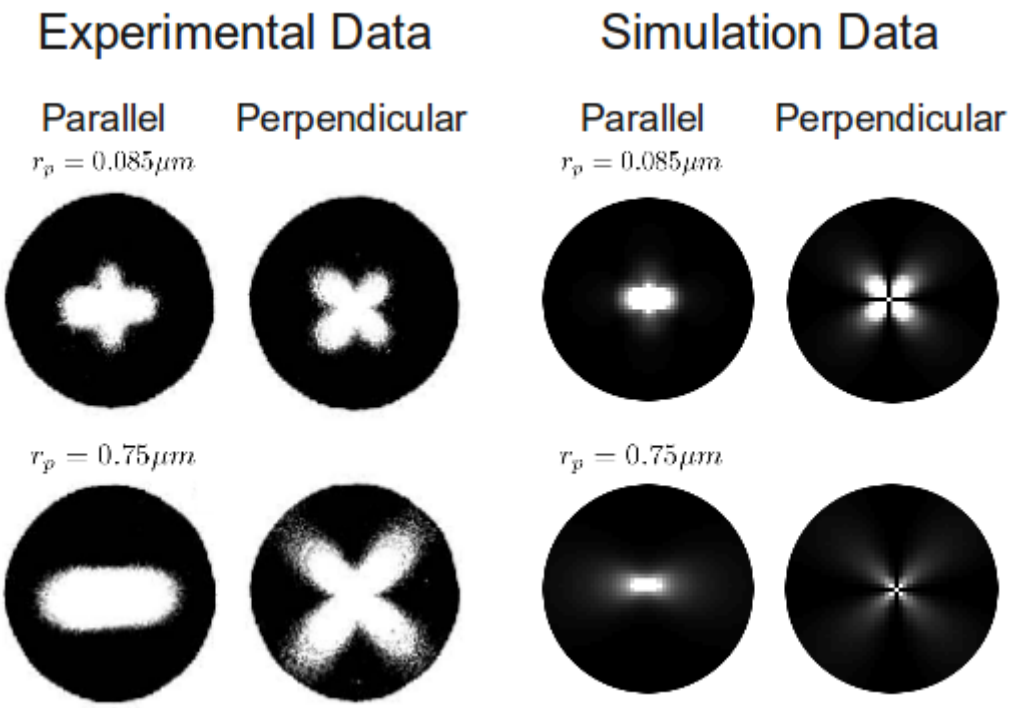

(a) Experiment (b) Simulation

Figure 3.6: Qualitative comparison of (a) published experimentally measured intensity patterns from all orders of multiple scattering by [58] and (b) simulated intensity patterns of second order scattering for spherical particle of radius r_p. The experimental data was recorded with a polarizer in front of the film in both positions parallel and perpendicular to the incident polarization. The same measurement method is duplicated for the simulations.

vertical and the scatterers are assumed spherical. The intensity patterns are recorded and simulated with a polarizer parallel to the transmit polarization then perpendicular. The experimentally recorded intensity patterns from [58] are reprinted here for qualitative comparison.

In both simulated and experimental data, the sensitivity of the detector and FOV are arbitrary. However, the patterns are qualitatively very similar. The particle with radius $0.085\mu m$ radiates very little along the direction of the incident polarization (vertical), while the particle with radius $0.75\mu m$ has a radiation lobe in the vertical direction. This means that smaller particles exhibit more diattenuation in second order scattering than large particles. While it is known that the particle scattering cross-section increases with particle radius, this total backscatter is also dependent on particle density. However, diattenuation is a polarization effect that can be normal-

ized, making it independent of particle density. Thus diattenuation might offer a useful means for characterizing particle size.

Chapter 4

Polarization Techniques

The ability to discern polarization in the scattering medium provides an additional data product for atmospheric characterization. However, the process of actually measuring polarization effects in the phase matrix is dependent on the technique employed.

For full characterization of an arbitrary scatterer, the entire phase matrix must be measured. To do so, four Stokes vectors, that span the Poincaré Sphere, are measured. Each full Stokes vector requires a minimum of four intensity measurements [18, 44, 14] thus requiring a total of 16 separate measurements. Clearly the most general approach for characterizing the scattering phase matrix places heavy demands on the lidar system. Each intensity measurement must either be acquired by splitting the return signal or polling individual polarizations in time. In both cases, redundant and zero elements are unnecessarily measured causing SNR to suffer while integration times and instrument complexity increase.

Fortunately, in most instances we can make assumptions about the form of the scattering phase matrix. This allows us to assume some of the elements in the phase matrix are zero. In addition to the zero elements in the matrix, there are often relationships between the different elements, thereby reducing the number of independent terms in the scattering matrix. Polarization techniques for measuring these reduced matrices have the benefit of improved SNR and shorter integration times due to the reduced number of irrelevant measurements (i.e. measuring a matrix element known to be zero). However the validity of the implied assumptions relates directly to the validity of the data and its interpretation. It is important to be conscious of this fact when

deriving meaning from polarization data. If the scattering medium does not conform to the assumed matrices, the measured quantities cannot be accurately linked to actual manifestation in the scatterer.

The sections below discuss the measurement of depolarization from randomly oriented particles, the impact and measurement of oriented particles and the use of altered polarization for improved lidar ranging.

The depolarization technique commonly employed in polarization lidar requires only the collection of parallel and perpendicular polarized backscatter intensity. This technique proves useful for measuring depolarization of scatterers that are randomly oriented, but the actual definitions of the scattering and detection techniques and their acceptable applications are largely unexplored. If lidar systems do not employ the same transmit polarizations (i.e. linear, circular, elliptical), the polarization ratio δ cannot be used as a common term for comparison between instruments. Furthermore, the depolarization technique is often employed for arbitrary atmospheric scattering problems, resulting in ambiguity as to how the collected data relates to polarization properties of the medium and therefore its physical attributes.

The depolarization technique generally applied to randomly oriented scatterers produces ambiguous results if used to characterize oriented scatterers. Due to the limited and confining techniques presently available for detecting oriented scatterers, very little is known about atmospheric oriented scatterer occurrence frequency and scattering attributes. We present here, two techniques for identifying the presence of oriented scatterers, by measuring the diattenuation of the scattering medium.

Polarization may also be used in ranging problems to separate returns from different surfaces. This technique capitalizes on polarization differences between the targets, but also, due to its very high level of temporal resolution, introduces new issues for ranging of two hard targets. In this case, the purpose of the polarization technique is not to characterize the targets, but to suppress signal originating from one of the targets. This allows the detector to effectively multiplex between two targets and enables sub-pulse length range resolution.

4.1 Depolarization

Owing to the fact that most scatterers in the atmosphere are randomly oriented, the most common polarization effect observed in the atmosphere is depolarization. In these circumstances, the scattering phase matrix is strictly depolarizing, given by Eq. (3.5), and has only one independent polarization term d for which allowable values only exist between zero and one [25, 26]. This fact makes the entire scattering phase matrix easy to characterize using the two measurements commonly employed in conventional polarization lidar.

In conventional polarization lidar operation, parallel and perpendicular components of the backscattered light are measured. The resulting photon counts are given by

$$\vec{N} = \begin{bmatrix} N_{||} \\ N_{\perp} \end{bmatrix}, \tag{4.1}$$

and the output matrix is

$$\mathbf{O} = \mathbf{o} \begin{bmatrix} \mathbf{P}_{||} \\ \mathbf{P}_{\perp} \end{bmatrix} \tag{4.2}$$

where $\mathbf{P}_{||}$ and $\mathbf{P}_{\perp}$ are 4x4 Mueller matrix descriptions of parallel and perpendicular polarizers in the receiver respectively and $\mathbf{o}$ transforms the resulting eight element Stokes vector into the two measured photon counts,

$$\mathbf{o} = \begin{bmatrix} \eta_{D||} & 0 & 0 & 0 & 0 & 0 & 0 & 0 \\ 0 & 0 & 0 & 0 & \eta_{D\perp} & 0 & 0 & 0 \end{bmatrix}, \tag{4.3}$$

where $\eta_{D||}$ and $\eta_{D\perp}$ are the detector efficiencies of the parallel and perpendicular channels.

If we evaluate the SVLE (Eq. (2.11)) using the definitions provided above and assuming there are no polarization effects in the lidar instrument or in atmospheric transmission, we find the depolarization of the scattering medium is calculated for linear transmit and detection polarizations [25, 26]

$$d = \frac{2N_{\perp}}{N_{\perp} + N_{||}}, \tag{4.4}$$

and for transmitted and received circular polarization

$$d = \frac{N_{\perp}}{N_{\perp} + N_{||}}. \tag{4.5}$$

In the general case where the transmitted Stokes vector is

$$\vec{S}_{TX} \propto \begin{bmatrix} 1 \\ \cos\Gamma_f \\ 0 \\ \sin\Gamma_f \end{bmatrix}, \tag{4.6}$$

where Γ_f is twice the ellipticity angle of the outgoing polarization [93]. The receiver detects in the polarization planes parallel and orthogonal to the transmitted mode. The receiver polarizers in Eq. (4.2) are thus fully described by their diattenuation vectors

$$\vec{D}_{\|} = \begin{bmatrix} \cos\Gamma_f \\ 0 \\ -\sin\Gamma_f \end{bmatrix}, \tag{4.7}$$

and

$$\vec{D}_{\perp} = \begin{bmatrix} -\cos\Gamma_f \\ 0 \\ \sin\Gamma_f \end{bmatrix}. \tag{4.8}$$

Note that the scattering matrix negates the polarized component of S_3, so Γ_f is negated in the parallel polarizer. The depolarization is then given by

$$d = \frac{4N_{\perp}}{\left(N_{\perp} + N_{||}\right)\left(3 - \cos 2\Gamma_f\right)}. \tag{4.9}$$

Thus, in the common case where the scattering medium consists of randomly oriented axially symmetric particles the full scattering matrix can be characterized through only two polarization measurements.

Because this polarization technique is common in lidar, it has been applied to a number of aerosol characterization applications [71, 75, 10, 46]. However, results are most commonly

reported in terms of the polarization ratio δ defined in Eq. (1.7). The polarization ratio derives its meaning from the measurement technique employed, not the scattering phase matrix. Thus, the quantity technically has no inherent assumptions about the form of the scattering matrix. This fact proves convenient, though ambiguous, when the form of the scattering matrix is not known. However, in order to fit the collected data to scattering models, assumptions must be made about the form of the matrix which is often unstated and unjustified in publications. By contrast, data reported as depolarization d is unambiguous. Without adding additional content, the assumed form of the scattering matrix is clearly communicated as that in Eq. (3.5). It leaves no room for misinterpretation of the author's assumptions about the medium, but the quantity cannot be applied to other scattering matrices.

The polarization ratio is dependent on the particular plane of operation for the lidar. When the lidar operates in linear polarizations, the polarization ratio is given by

$$\delta_l = \frac{N_\perp}{N_\parallel} = \frac{d}{2-d}, \tag{4.10}$$

but if the system uses circular polarization, the lidar will measure a polarization ratio given by

$$\delta_c = \frac{N_\perp}{N_\parallel} = \frac{d}{1-d}. \tag{4.11}$$

A notable consequence of these equations is that the circular polarization ratio may be any number from zero to infinity, while linear polarization ratios are confined on the same interval as d (zero to one). When lidar data products are reported in terms of d, there can be no confusing lidar operating parameters with the scattering characteristics of the atmosphere. Thus, using depolarization instead of polarization ratio offers an additional reduction in ambiguity, by removing dependence on the instrument's polarization mode of operation.

In this work, the polarization ratio is still used in cases where the scattering matrix is either unknown, or may be a composition of more than one independent matrix element. However, use of this data product proves to be limiting without additional polarization measurements.

If we apply the polarization technique discussed here to the more general scattering matrix

of oriented scatterers in Eq. (3.21) and let lidar operate in an arbitrary polarization

$$\vec{S}_{TX} = \begin{bmatrix} 1 \\ \cos 2\phi_f \cos \Gamma_f \\ \sin 2\phi_f \cos \Gamma_f \\ \sin \Gamma_f \end{bmatrix}, \tag{4.12}$$

where ϕ_f is the inclination angle and Γ_f is twice the ellipticity angle of the outgoing polarization [93]. We can evaluate Eq. (2.11) to find the general form of the polarization ratio is

$$\delta\left(\phi_f, \Gamma_f, \mathbf{F}\right) = \frac{-f_{11} + f_{22}\cos^2 2\phi_f \cos^2 \Gamma_f + f_{33}\sin^2 2\phi_f \cos^2 \Gamma_f + f_{44}\sin^2 \Gamma_f}{f_{11} + 2f_{12}\cos 2\phi_f \cos \Gamma_f + f_{22}\cos^2 2\phi_f \cos^2 \Gamma_f + f_{33}\sin^2 \phi_f \cos^2 \Gamma_f + f_{44}\sin^2 \Gamma_f}. \tag{4.13}$$

As complexity of the scattering matrix increases, the polarization ratio becomes increasingly dependent on the lidar's operating polarization. More importantly, because the elements of the matrix cannot be uniquely determined from Eq. (4.13), these data products cannot be compared between instruments using different polarizations. Thus, it is important to understand how the polarization technique covered here has limited practical benefit when we cannot assume the scattering medium's phase matrix conforms to the depolarizer described in Eq. (3.5). In such instances, other polarization techniques are required to both identify the presence of non-depolarizing effects and characterize the medium.

4.2 Diattenuation

In atmospheric cases such as multiple scattering and scattering by oriented ice crystals, the phase matrix does not conform to Eq. (3.5). The depolarization d has no meaning because it is not directly related to the medium's scattering matrix. Though perpendicular and parallel polarization components can still be measured, the polarization ratio cannot distinguish between different scattering matrices, nor is it strictly related to a depolarizing effect in the scattering medium.

The ability to detect the presence of oriented scatterers has been a subject of inquiry with

limited success. Though a common technique has been developed to look for oriented scatterers [56], the measurement fails to work well with other atmospheric measurements. In order to gather information on occurrence frequency of oriented scatterers, the Cloud-Aerosol Lidar with Orthogonal Polarization (CALIOP) on CALIPSO was pointed near nadir for one year to look for specular scattering from oriented platelets. This measurement, however, came at a price. When specular returns are present, the high intensity signal overwhelms detectors, thus preventing simultaneous study of other aerosol and cloud polarization and backscatter ratios [35]. As a result, the study of oriented scatterers and aerosol characteristics were somewhat mutually exclusive during the CALIPSO mission, and data collection on oriented platelets was limited to a run of only eighteen months.

CALIPSO and [56] identified oriented scatterers by their strong specular returns and low polarization ratios for lidars operating near nadir or zenith respectively. This method has the limitation of only identifying oriented platelets, not necessarily columns or bullets oriented in the horizontal plane. Due to the narrow solid angle where specular returns can be expected, it is difficult to determine if scatterers may have been misclassified as randomly oriented in cases where their angular distributions are narrow. Indeed after tilting CALIOP 3° off nadir for the remainder of the CALIPSO mission, clouds containing oriented scatterers had the same backscatter/polarization ratio signatures as randomly oriented ice crystals [55], thus demonstrating the substantial sensitivity to the pointing direction of the lidar relative to platelet orientation. Because CALIOP is not a scanning lidar and only probes one point of the angular phase function, it is difficult to definitively claim the measurement was able to accurately determine oriented scatterer concentrations. This may account for the substantial discrepancy in oriented ice crystal concentration estimates between [55] and [54] ($< 5\%$ and $< 21\%$ respectively). As previously discussed, this mode of lidar operation also largely prevents simultaneous aerosol studies and cloud characterization due to the relative difference in signal levels between specular and non-specular returns.

The work published by Kaul [39, 44] has been some of the most comprehensive scatterer characterization work, where the lidar measures all 16 elements of the phase matrix. Measuring

the full phase matrix leaves little uncertainty about the polarization effects of the scatterer, however the complexity of such a system for design and deployment is perhaps too great for widespread use.

Other researchers have used the functional relationship between circular and linear polarization ratios in Eq. (4.10) and (4.11) for randomly oriented scatterers as a criteria for identifying the presence of preferential orientation in the scatterer [31, 5]. However, there is no requirement that volumes containing oriented scatterers cannot have a similar functional relationship between linear and circular polarization ratios. Thus this technique cannot misclassify randomly oriented scatterers as oriented, but oriented scatterers may be misclassified as randomly oriented. This may tend to underestimate the occurrence frequency of oriented scatterers. Also, researchers using this method have been hesitant to assert the relationship between linear/circular polarization ratio and orientation. This is because randomly oriented scatterers without axial symmetry can theoretically exhibit circular diattenuation (non-zero (1,4) and (4,1) terms in the scattering matrix). The presence of circular diattenuation would nullify the assumed functional relationship between polarization ratios.

For practical identification of oriented scatterers, detection techniques must be simple, robust and accommodating of other aerosol studies. To identify the presence of oriented scatterers, we note that linear diattenuation is exhibited in the oriented scattering phase matrix [39] when the lidar is operating off zenith. By contrast, randomly oriented scatterers exhibit no linear diattenuation in their scattering matrix. Thus measuring a non-zero linear diattenuation while the lidar is pointed off zenith indicates the presence of oriented scatterers.

4.2.1 Parallel-45-Perpendicular

For the greatest versatility in polarization measurement, we would like to be able to measure both polarization ratio and diattenuation simultaneously. The Parallel-45-Perpendicular (P45P) technique achieves this objective by transmitting a linear polarization and adding an additional receiver polarization channel at 45° to the conventional parallel-perpendicular polarization lidar.

Thus the new measurements are given by

$$\vec{N} = \begin{bmatrix} N_{||} \\ N_{45} \\ N_{\perp} \end{bmatrix}, \tag{4.14}$$

where the subscript indicates the receiver polarizer position relative to the transmit polarization and thus $\mathbf{O}$ is now given by

$$\mathbf{O} = \mathbf{o} \begin{bmatrix} \mathbf{P}(0^\circ + \phi_f) \\ \mathbf{P}(45^\circ + \phi_f) \\ \mathbf{P}(90^\circ + \phi_f) \end{bmatrix}, \tag{4.15}$$

where ϕ_f is the transmit polarization angle, $\mathbf{P}(\theta)$ is the Mueller matrix of a linear polarizer at orientation θ and

$$\mathbf{o} = \begin{bmatrix} \eta_D & 0 & 0 & 0 & 0 & 0 & 0 & 0 & 0 & 0 & 0 & 0 \\ 0 & 0 & 0 & 0 & \eta_D & 0 & 0 & 0 & 0 & 0 & 0 & 0 \\ 0 & 0 & 0 & 0 & 0 & 0 & 0 & 0 & \eta_D & 0 & 0 & 0 \end{bmatrix}. \tag{4.16}$$

We define the polarization coordinate frame such that the Stokes vector $\begin{bmatrix} 1 & 1 & 0 & 0 \end{bmatrix}^T$ represents s-polarization in the horizontal plane in Figure 3.2. For this coordinate frame the scattering matrix in the SVLE is given by Eq. (3.21). The term f_{12} accounts for the total linear diattenuation of the scatterer, and a nonzero value in this position indicates the scatterer is not randomly oriented. We now define a qualitative assessment of this linear diattenuation

$$D_q = \frac{2N_{45}}{N_{||} + N_{\perp}} - 1 = \frac{f_{12} \sin 2\phi_f + \frac{1}{2}(f_{22} + f_{33}) \sin 4\phi_f}{f_{11} + f_{12} \cos 2\phi_f}. \tag{4.17}$$

If f_{12} is zero, the scattering matrix will take the form in Eq. (3.5) where $f_{22} = -f_{33}$ [87] and the numerator evaluates to zero. Note again, that ϕ_f is the relative angle between the s-polarization in the horizontal plane and incident polarization. Thus, if we set the linear polarization angle to $\phi_f = 45^\circ$,

$$D_q = \frac{f_{12}}{f_{11}} = f'_{12}, \tag{4.18}$$

which is the normalized linear diattenuation of the scattering matrix from Eq. (3.21).

From Eq. (4.17) we determine the measurement sensitivity to misalignment of ϕ_f

$$\left.\frac{\partial D_q}{\partial \phi_f}\right|_{\phi_f=\frac{\pi}{4}} = 2D_q^2 - 2\left(\frac{f_{22}+f_{33}}{f_{11}}\right). \tag{4.19}$$

Note that Eq. (4.19) is a function of scatterer diattenuation. For no diattenuation, the sensitivity to misalignment is zero. It is difficult to assert any specific relationship between f_{22} and f_{33} for an oriented scatterer, as they are functions of the matrix diattenuation and retardance respectively. However, because $|D_q| \leq 1$ and $\frac{f_{22}+f_{33}}{f_{11}} \leq 2$ [52], we can bound the error introduced by polarization misalignment $\Delta\phi_f$ as

$$\Delta D_q \leq 4\Delta\phi_f. \tag{4.20}$$

In addition to this assessment of linear diattenuation in the scatterer, when $\phi_f = 45°$, we can also obtain the normalized (3,3) element of the scattering matrix.

$$\frac{f_{33}}{f_{11}} = f'_{33} = \frac{N_{\parallel} - N_{\perp}}{N_{\parallel} + N_{\perp}}. \tag{4.21}$$

When the scatterer is randomly oriented, we can use the notation of [26] and write, independent of ϕ_f,

$$f'_{33} = d - 1. \tag{4.22}$$

In the case of randomly oriented scatterers, this measurement fully characterizes the depolarizing effect of the scattering volume. When scatterers are not randomly oriented (as indicated by a nonzero D_q signature), the f'_{33} element contains multiple polarization terms. We apply the Lu-Chipman decomposition performed in Chapter 3, multiplying the polarization matrices according to Eq. (3.25). This reveals the measured f'_{33} element has the following relationship to the matrix polarization terms:

$$f'_{33} = \sqrt{1 - {f'_{12}}^2}\left(\cos\Gamma_F - d_2\cos^2\frac{\Gamma_F}{2} + d_3\sin^2\frac{\Gamma_F}{2}\right), \tag{4.23}$$

where $f'_{12} = \frac{f_{12}}{f_{11}}$ and is the normalized diattenuation of the scattering matrix, Γ_F is the retardance of the scattering matrix, d_2 is the depolarization for the depolarizer basis vector nearest $\pm 45°$ polarizations and d_3 is the depolarization for the depolarizer basis vector nearest circular

polarizations. Note that f'_{12} is calculated in the diattenuation measurement D_q, but the remainder of Eq. (4.23) still contains three independent polarization terms. Thus, when oriented scatterers are present, this measurement provides some insight into additional scattering parameters, but the physical polarization effect, in the general case, cannot be strictly attributed to retardance and depolarization.

Note that use of P45P, allows us to test our assumption that scatterers in the volume are randomly oriented. The presence of a diattenuation signature, tells us that the polarization data cannot be reported in terms of d because the scattering volume does not have the correct matrix form. We can still report data in terms of the polarization ratio, but it will not uniquely depend on one scattering matrix term. The best way of reporting this data is in terms of the normalized (3,3) component f'_{33} because it unambiguously identifies an element of the scatterer's matrix description regardless of orientation.

4.2.1.1 Simulation of P45P

The polarization ray tracing code described in Section 3.2 is run to evaluate the polarization scattering properties of oriented ice platelets at different lidar tilt angles. This is then used in a lidar simulation to determine optimal lidar tilt angles for system performance. We consider a typical tropospheric polarization lidar operating at 532 nm performing the polarization measurements required for the P45P technique to identify oriented ice crystals.

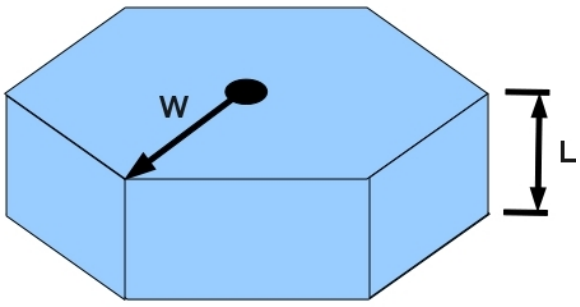

Figure 4.1: Relevant dimensions for simulation of hexagonal ice crystals. Crystal length is marked L and the crystal base radius is marked W.

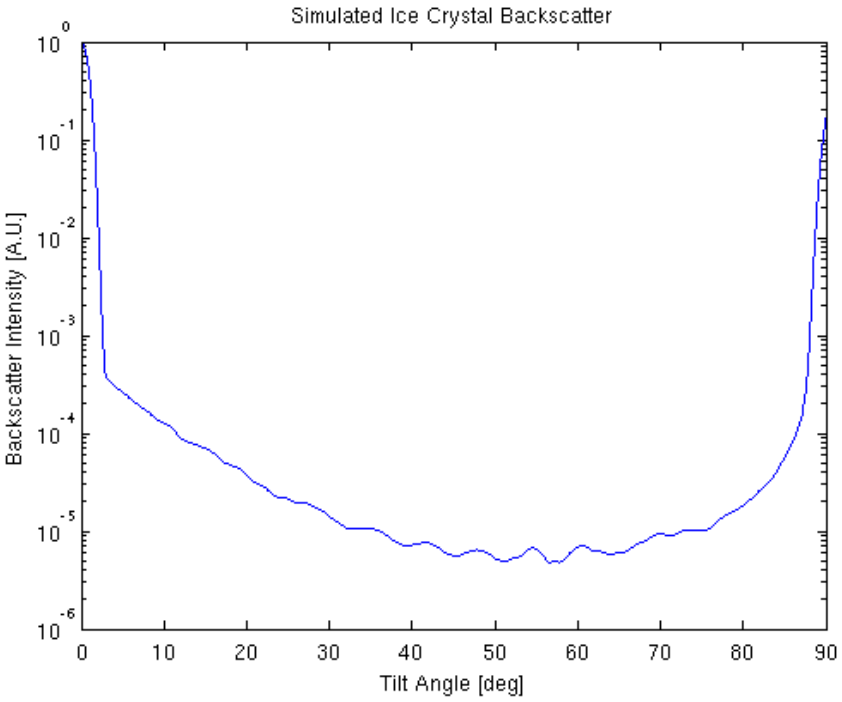

Figure 4.2: Simulated backscatter as a function of tilt angle for hexagonal platelets using polarization ray tracing described in Chapter 3. The platelets have a Gaussian angular distribution width of 3°.

We consider the backscatter phase matrix of oriented hexagonal ice platelets with crystal length (L) of $120\mu m$ and base radius (W) of $160\mu m$ [31] (see Figure 4.1). We assume they are oriented so the large crystal faces point downward and the distribution of crystal tilt out of the horizontal plane (flutter) is Gaussian such that the first null in the lobe from specular reflection occurs at 3°. In most cases oriented ice crystals have a specular reflection width of less than 3° [54]. The PW elements are broken into squares 30λx30λ and contributions from up to 5 internal reflections are calculated.

The simulation results for backscattering intensity and diattenuation are plotted as a function of lidar tilt angle in Figures 4.2 and 4.3. In Figure 4.2 we see the narrow, high intensity peak for instances where the lidar is pointing zenith or nadir. This peak rapidly falls off, so that even a slight deviation in angle will significantly reduce the observed intensity. This peak width is a function of particle size (due to diffraction) and the ice crystal tilt angle distribution.

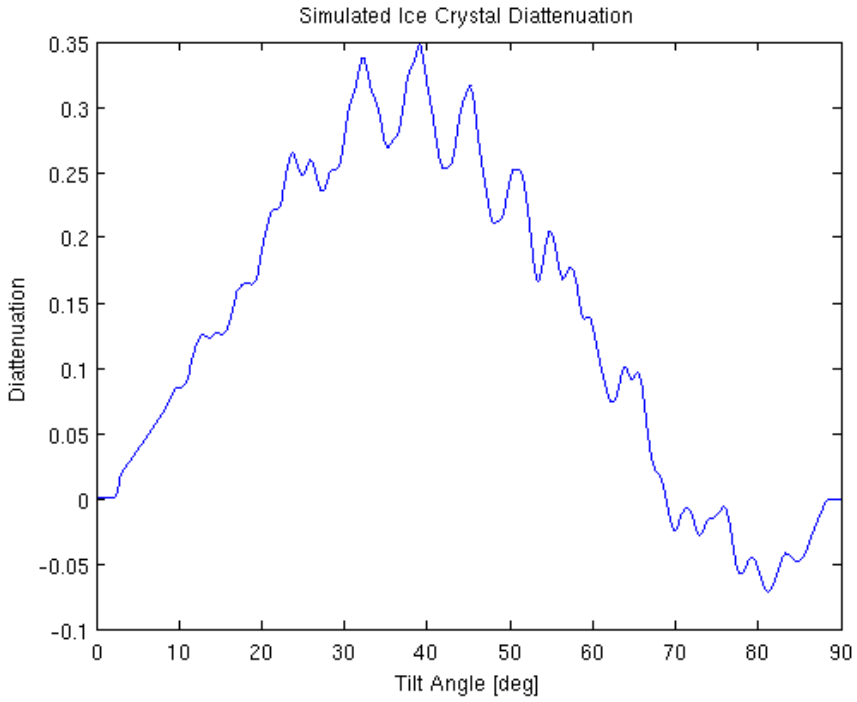

Figure 4.3: Simulated diattenuation as a function of tilt angle for hexagonal platelets using polarization ray tracing described in Chapter 3. The platelets have a Gaussian angular distribution width of 3°. Oscillations on the overall curve would likely average out if a distribution of crystal sizes is considered. The reader's focus should be on the overall functional shape.

At higher tilt angles, the backscatter signal is several orders of magnitude weaker than the specular returns. At these intensities the signals are less likely to overwhelm or saturate detection systems designed for randomly oriented aerosol studies. Thus lower backscatter may be a desirable characteristic. By controlling the tilt angle we can engineer the system for simultaneous cloud and aerosol characterization while identifying oriented scatterers. Figure 4.3 illustrates that diattenuation is zero for a zenith pointing lidar, but becomes larger as the lidar tilt angle approaches 40°. Thus one can trade required dynamic range of the lidar system with the diattenuation measurement sensitivity to shot noise and system error contributions to determine the optimal tilt angle for detecting oriented scatterers.

In general, the value of D_q within a measurement volume is not given exclusively by the single particle scattering matrix. Rayleigh scattering from molecules as well as the scattering matrix of randomly oriented cloud particles must be considered. The total scattering matrix is therefore the sum of all contributing scattering matrices, weighted by their relative contributions to the backscattered signal

$$\mathbf{F}(\vec{k}_i, -\vec{k}_i) = N_c p_o \mathbf{F_o}(\vec{k}_i, -\vec{k}_i) + N_c(1-p_o)\mathbf{F_r}(\pi) + N_{mol}\mathbf{F_{mol}}(\pi). \tag{4.24}$$

The term N_c is the total scatterer number density of the cloud, p_o is the fraction of scatterers in the cloud that are oriented, $\mathbf{F_o}(\vec{k}_i, -\vec{k}_i)$ is the backscatter matrix of the oriented scatterers which is a function of tilt angle, $\mathbf{F_r}(\pi)$ is the backscatter matrix of randomly oriented cloud particles, N_{mol} is the molecular scatterer number density and $\mathbf{F_{mol}}(\pi)$ is the scattering matrix of the molecular scatterers. Note that for the randomly oriented cloud and molecular contributors, their matrices will have the form shown in Eq. (3.5). Thus for low concentrations of oriented particles, randomly oriented scatterers will "dilute" the diattenuation of the total backscatter phase matrix.

Due to the presence of the randomly oriented scatterers in Eq. (4.24), the volume diattenuation as a function of tilt angle may not be the same as the individual crystal diattenuation in Figure 4.3. As tilt angle increases to 40°, diattenuation in the crystal scattering matrix increases. But at angles where the diattenuation is large, the oriented ice crystals contribute less signal to volume

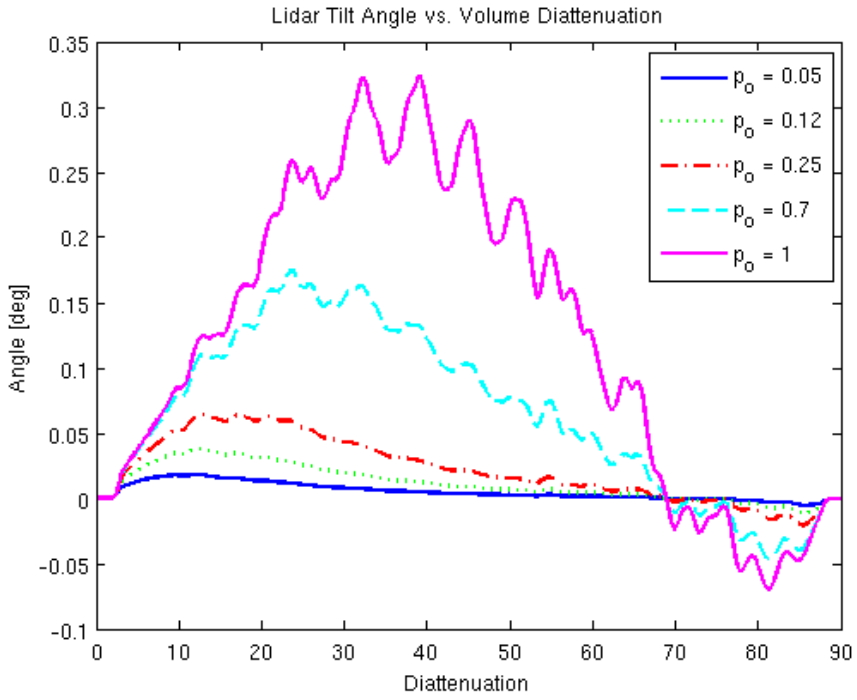

Figure 4.4: Simulated volume diattenuation of hexagonal platelets with flutter distribution width of 3° as a function of lidar tilt angle. The cloud has an oriented scatterer concentration of p_o and altitude of 10 km. The density of the cloud is determined by assuming the backscatter ratio R_{BS} is 50 when $p_o = 0$.

backscatter causing greater dilution of diattenuation. Figure 4.4 shows the volume diattenuation as a function of lidar tilt angle for a variety of oriented scatterer concentrations p_o. The total number density of ice crystals is determined by assuming a randomly oriented cloud ($p_o = 0$) has a backscatter ratio of 50 where the backscatter ratio is defined in Eq. (1.4) and for this specific case may be written [47]

$$R_{BS} = \frac{\beta_{mol} + \beta_c}{\beta_{mol}} = \frac{f_{11}^{mol} + f_{11}^{c}}{f_{11}^{mol}}, \tag{4.25}$$

where β_m is the volume backscatter coefficient of the molecular scatterers and is also the f_{11}^{mol} term of the molecular scattering matrix and β_c is the volume backscatter coefficient of the cloud and is also the f_{11}^{c} term of the total cloud scattering matrix in Eq. (4.24).

As the population density of oriented scatterers increases, the volume backscatter diattenuation more closely resembles that of the oriented ice crystal. The peak value of diattenuation changes

as a function of the oriented scatterer concentration p_o. Current data suggests oriented scatterers are generally low in concentration, ranging from $p_o = 0.05$ [55] to $p_o = 0.2$ [54]. However, the space-based instruments that determined these concentrations integrated over areas much larger than those of a typical terrestrial based lidar system. It is difficult to know if oriented scatterers tend to concentrate in pockets or are evenly distributed within the cloud. Thus for a typical terrestrial lidar with a much smaller integrated area, p_o could take any value from 0.05 to 1.00 when oriented ice crystals are present.

Backscatter ratio also plays a role in determining how molecular scattering dilutes the oriented ice crystal matrix. As the backscatter ratio increases, larger volume diattenuation may be possible at higher tilt angles. Thus we consider the cloud's maximum diattenuation as a function of the cloud's equivalent randomly oriented backscatter ratio and p_o. The results are plotted in Figure 4.5 where it is clear that peak values of diattenuation level off asymptotically, resulting in diminishing returns for higher backscatter ratios. The angles corresponding to those peak diattenuation values are plotted in Figure 4.6.

The scattering volume diattenuation determines tolerable error in measured signals. In order to accurately resolve the presence of diattenuation, we wish to have $D_q \gg \sigma_{D_q} + \Delta D_q$ where σ_{D_q} is the diattenuation error due to shot noise and ΔD_q is error introduced by the optical system (discussed in further detail in Chapter 5). The shot noise uncertainty of diattenuation measurements using P45P is determined using propagation of error:

$$\sigma_{D_q}^2 = \frac{4}{N_{RX}^2}\left[\sigma_{45}^2 + \sigma_{N_{RX}}^2\left(\frac{N_{45}}{N_{RX}}\right)^2\right] \tag{4.26}$$

where σ_x is the standard deviation of x, N_{RX} is the sum of the total photons detected on the perpendicular and parallel channels during the integration time, and N_{45} are the photons received during the integration time on the 45° polarization measurement.

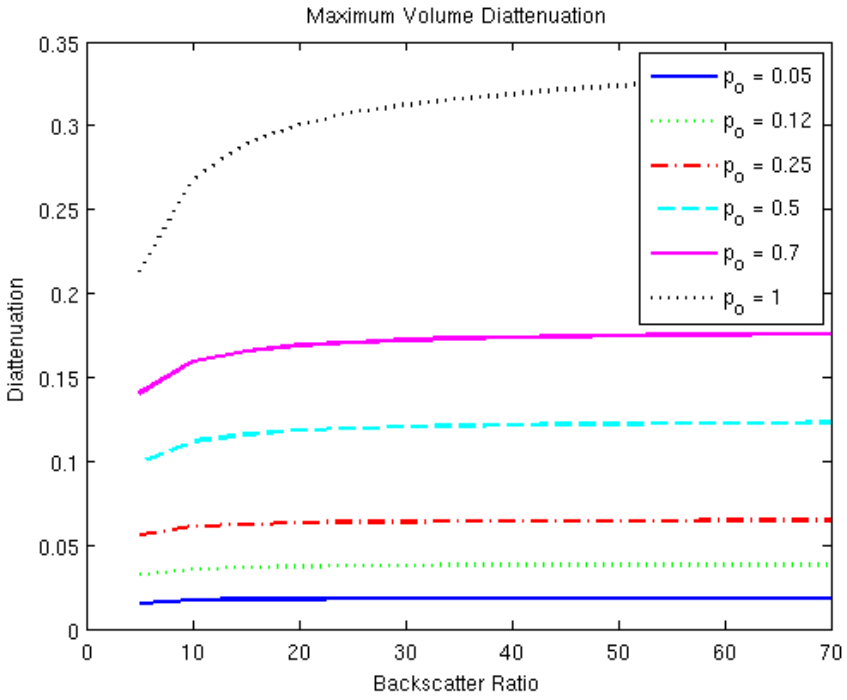

Figure 4.5: Simulation using polarization ray tracing in Section 3.2 of maximum volume diattenuation as a function of non-specular backscatter ratio at various concentrations of oriented scatterers. Here the oriented scatterers are diluted by both molecular scatterers and randomly oriented ice crystals.

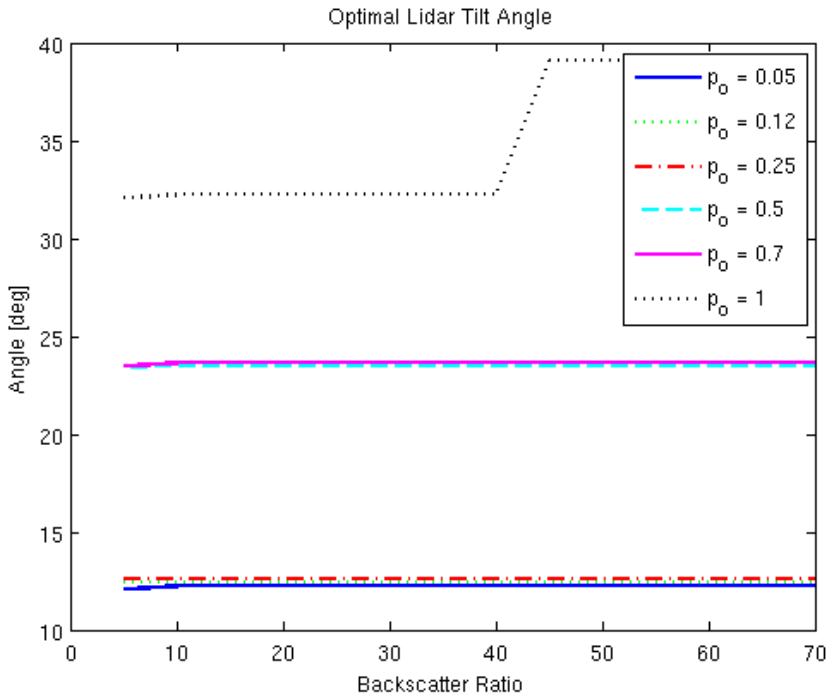

Figure 4.6: Tilt angle corresponding to maximum volume diattenuation as a function of non-specular backscatter ratio at various concentrations of oriented scatterers. Optimal tilt angles are nearly constant for most concentrations and make discrete hops as a function of concentration. The weakest clouds ($p_o < 0.25$) are ideally probed at angles between 10° and 20°.

4.2.2 Alternating Cross Polarized

While P45P offers the benefit of measuring both polarization ratio and diattenuation simultaneously, it is not always practical for implementation in existing lidar. The Alternating Cross Polarized (ACP) technique more directly measures diattenuation by measuring the polarization dependence of the volume scattering coefficient. This is done by transmitting alternating, orthogonal polarizations and measuring the difference in backscatter. Though the technique does not allow for simultaneous measurement of polarization ratio, the ARCLITE lidar is easily modified for this technique. Also, as will be shown in Chapter 5, this technique is unaffected by retarding and depolarizing effects in the receiver.

ACP transmits two orthogonal polarizations and measures the resulting backscatter photon counts from the medium. Diattenuation in the medium can be determined by the relative difference in backscatter amplitudes. If the scattering matrix takes the form shown in Eq. (3.21), the normalized diattenuation can be directly measured by transmitting orthogonal polarizations corresponding to the nonzero diattenuating element. Thus, we transmit alternating orthogonal polarizations,

$$\vec{S}_{TX_1} = N_{TX} \begin{bmatrix} 1 \\ \cos 2\phi_f \\ \sin 2\phi_f \\ 0 \end{bmatrix}, \tag{4.27}$$

and

$$\vec{S}_{TX_2} = N_{TX} \begin{bmatrix} 1 \\ -\cos 2\phi_f \\ -\sin 2\phi_f \\ 0 \end{bmatrix}, \tag{4.28}$$

where transmit photons N_{TX} are the same for both modes. We then measure the received intensity corresponding to each transmit polarization. Thus the output matrix is

$$\mathbf{O} = \begin{bmatrix} \eta_D & 0 & 0 & 0 \end{bmatrix}. \tag{4.29}$$

The measured diattenuation of the scatterer along the transmitted Stokes vectors is then given by

$$\frac{f_{12}}{f_{11}}\cos 2\phi_f = \frac{N_{RX_1} - N_{RX_2}}{N_{RX_1} + N_{RX_2}}, \tag{4.30}$$

where N_{RX_1} is the intensity received when transmitting $\vec{S}_{TX_1}$ and N_{RX_2} is the intensity received when transmitting $\vec{S}_{TX_2}$.

By selecting $\phi_f = 0$ (see Figure 3.2) the normalized diattenuation f'_{12} is fully measured using Eq. (4.30). Likewise, when ϕ_f is 45°, diattenuation cannot be accurately measured through the two transmit polarizations. Thus care must be taken in how the operator orients the transmit polarizations relative to the lidar tilt angle.

4.3 Intrapulse Phase Modification Induced by Scattering

Intrapulse Phase Modification Induced by Scattering (INPHAMIS) is a polarization technique for hard target lidar that can be used to suppress signals from one or more surfaces. This, in effect, allows the lidar to multiplex between surfaces using polarization, changing the two-target ranging problem into two one-target range problems. One target range problems can then be solved using the same techniques as conventional laser altimeters, that can obtain centimeter range accuracy, independent of laser pulse length.

The driving requirement for this technique is that surface 1 and surface 2 cannot have the same polarization properties. In general, however, there are no specific requirements imposed on the scattering matrices of the first and second surfaces, $\mathbf{F}_1$ and $\mathbf{F}_2$ respectively. The fundamental requirement to resolve the position of the second surface is that its SNR must be greater than one.

$$SNR_2(t, t+\Delta t) = \frac{N_2(t, t+\Delta t)}{\sqrt{N_2(t, t+\Delta t) + N_1(t, t+\Delta t) + N_B(\Delta t)}}, \tag{4.31}$$

where $N_2(t, t+\Delta t)$ are the mean photon counts from the second surface over the detection interval from time t to $t+\Delta t$, $N_1(t, t+\Delta t)$ are the mean photon counts from the first surface over the same interval which are regarded as noise in this case, and $N_B(t, t+\Delta t)$ are the mean background counts received during the detection interval.

The use of the SVLE becomes critical in this scenario, because it provides the theory definitions necessary to optimize SNR in the presence of arbitrary scattering effects.

The transmitter is already defined in the most general terms in Eq. (4.12). For an arbitrary scattering problem, four parameters can be optimized: The transmitted polarization angle ϕ_f, the transmitted ellipticity angle Γ_f, the analyzer polarization angle ϕ_{RX} and the analyzer ellipticity angle Γ_f. This optimization assumes that the instrument can achieve any possible transmitted and detected polarization state. If we wish to confine the allowed solutions to strictly linear transmit and receive polarizations the terms Γ_f and Γ_{RX} can be set to zero. More generally, the variables optimized may be parameters of the specific system elements (i.e. wave plate angles and phase). Never-the-less, the optimization problem is basically unchanged.

The SNR of the second surface should be maximized in the instrument's available parameters space. Though not explicitly stated in Eq. (4.31), all of the photon count terms are naturally dependent on the transmit and receiver polarization states ϕ_f, Γ_f, ϕ_{RX} and Γ_{RX}. Thus optimal operation of INPHAMIS is given by maximizing SNR_2.

4.3.1 Example Application of INPHAMIS

In the simplest case where INPHAMIS may be applied, one surface is polarization preserving with a scattering matrix

$$\mathbf{F}_1(\pi) = \beta_1 \begin{bmatrix} 1 & 0 & 0 & 0 \\ 0 & 1 & 0 & 0 \\ 0 & 0 & -1 & 0 \\ 0 & 0 & 0 & -1 \end{bmatrix}, \tag{4.32}$$

while the second surface isotropically depolarizes by an amount d_2 so that its scattering matrix is given by

$$\mathbf{F}_2(\pi) = \beta_2 \begin{bmatrix} 1 & 0 & 0 & 0 \\ 0 & 1-d_2 & 0 & 0 \\ 0 & 0 & d_2-1 & 0 \\ 0 & 0 & 0 & d_2-1 \end{bmatrix}, \tag{4.33}$$

If $\beta_1 \gg \beta_2$, strict intensity detection will make it difficult to see the presence of backscatter signal from the second surface. However, the signal from the first surface can be fully suppressed by orienting a polarizer in the receiver to reject the transmitted polarization [53]. In this case, signals from the first surface will not be received by the detector. If range to the first surface is desired, the polarizer can be reoriented to allow some light from the first surface onto the detector. Thus the two target ranging problem becomes two single target problems. Because the problem is ranging of a single return, the resolution of the measurement is independent of the laser pulse width and detector speed and instead is driven strictly by the clock rate on the detection electronics.

4.3.2 Background Light

In the example above, any polarization may be chosen to operate the lidar. However the presence of solar background light may still result in a unique optimum polarization. The shot noise limited SNR of the weaker second surface is given in Eq. (4.31). The background count contribution is determined using the SVLE, and is the product of the background Stokes vector and the receiver projection matrix. The background Stokes vector is most generally described

$$\vec{S}_B(\Delta t) = N_{B0}(\Delta t) \begin{bmatrix} 1 \\ P_B \cos 2\phi_B \cos \Gamma_B \\ P_B \sin 2\phi_B \cos \Gamma_B \\ P_B \sin \Gamma_B \end{bmatrix}, \tag{4.34}$$

where $N_{B0}(\Delta t)$ is the total photons incident on the detector over the interval Δt when no polarizer P_{RX} is present, P_B is the DOP of the background light, ϕ_B is the orientation of the polarization

component of background light, and Γ_B is twice the ellipticity angle of the background.

The projection matrix is here assumed to be a polarizer $\mathbf{P}_{RX}$ for an arbitrary polarization. In the general case, it is a diattenuator with unit magnitude diattenuation vector

$$\vec{D}_{P_{RX}} = \begin{bmatrix} \cos 2\phi_{RX} \cos \Gamma_{RX} \\ \sin 2\phi_{RX} \cos \Gamma_{RX} \\ \sin \Gamma_{RX} \end{bmatrix} \tag{4.35}$$

where ϕ_{RX} is the linear rotation, and Γ_{RX} twice the ellipticity angle of the the polarization accepted by the polarizer. From the diattenuation vector in Eq. (4.35), Eq. (2.2) can be used to determine the total polarizer matrix.

When the background light is passed through $\mathbf{P}_{RX}$, the total background photon counts are then given by the product of the Stokes vector in Eq. (4.34) with the projection matrix defined by Eq. (4.35) giving

$$\begin{aligned} N_B(\Delta t) = \; & \frac{N_{B0}(\Delta t)}{2} \left(1 + P_B \cos 2\phi_B \cos 2\phi_{RX} \cos \Gamma_B \cos \Gamma_{RX} \right. \\ & + P_B \sin 2\phi_B \sin 2\phi_{RX} \cos \Gamma_B \cos \Gamma_{RX} \\ & \left. + P_B \sin \Gamma_B \sin \Gamma_{RX} \right). \end{aligned} \tag{4.36}$$

Thus, even though the signal from the first surface can be fully rejected for any polarization of operation, the presence of polarized background suggests for maximum SNR we should transmit the same polarization as the background, and detect in the polarization orthogonal to it. The effectiveness of this technique is dependent on the background DOP.

In this case, we see how the presence of polarized background can drive the system operation of INPHAMIS to a unique optimization. As more complicated polarization effects are considered, optimal solutions generally do not have analytic solutions. Furthermore full suppression of the signal from the first surface and polarized background can be mutually exclusive, so that optimal SNR will depend on the levels of each noise source.

4.3.3 Hard Target Photon Count Distributions

Ranging hard targets down to centimeter (70 ps) accuracy with longer pulse lengths means that photon returns from a single target will be distributed over multiple range bins. Practical factors independent of the system's ability to range using INPHAMIS such as the laser pulse distribution in time, PMT timing jitter caused by variable traversal times of the dynode chain, and the timing and shape of PMT pulses all contribute to a return signal that is wider than the electronic bin resolution. In order to accurately deconvolve these timing signals to the resolution of the timing electronics, we must understand how these signal distributions are impacted by the operating parameters of the system. In particular, how does detection accuracy change as a function of discriminator threshold (the voltage or current level that must be exceeded for the data acquisition board to count a PMT pulse), background level, and the number of photons incident on the detector?

We assume the laser transmits a Gaussian pulse so that it is described in time by

$$N_L(t) = N_{L0}\frac{1}{\sqrt{2\pi\sigma_L^2}}\exp\left(\frac{-(t-t_R)^2}{2\sigma_L^2}\right), \tag{4.37}$$

where N_{L0} is the total number of photons in the pulse incident on the detector, σ_L is the width of the pulse and t_R is the range time representing the propagation time of the pulse. Because it only represents an offset in timing, this analysis will set t_R to zero.

The timing jitter of the PMT is also Gaussian where the delay between an incident photon on the cathode and the resulting output current pulse of the PMT is a random variable given by the probability distribution function

$$P_{PMT}(t) = \frac{1}{\sqrt{2\pi\sigma_{PMT}^2}}\exp\left(\frac{-(t-t_{PMT})^2}{2\sigma_{PMT}^2}\right), \tag{4.38}$$

where t_{PMT} is the average time delay and σ_{PMT} is the standard deviation or timing jitter of the PMT.

Finally the PMT current pulse shape is described as a piecewise function to approximate

that observed at the PMT output

$$I_{PMT}(t) = \begin{cases} 1 - \exp\left(\dfrac{-t}{\tau_R}\right) & for \quad t \leq 4\tau_R \\ \left[1 - \exp\left(\dfrac{-t}{\tau_R}\right)\right] \exp\left(\dfrac{-(t-4\tau_R)^2}{(\tau_F/\sqrt{2ln2})^2}\right) & for \quad t > 4\tau_R \end{cases} \tag{4.39}$$

where τ_R and τ_F are the rise and fall times of the pulse respectively. Note that this function is defined based on the observed behavior of PMT pulses and has no fundamental mathematical basis. The function above can also be scaled by the mean PMT current per photon, however in this analysis we normalize $I_{PMT}(t)$ so its integral is one. This makes computation of the photon count distribution easier. Conversion between photon counts, current or voltage is most easily applied later, when setting the discriminator threshold.

The mean number of PMT pulses are then given by the convolution of the photon counts incident on the detector, PMT jitter and normalized PMT pulse shape

$$\langle N_D(t) \rangle = \eta_{QE} \left(N_L(t) + N_B(t) \right) * P_{PMT}(t) * I_{PMT}(t), \tag{4.40}$$

where η_{QE} is the detector quantum efficiency and $N_B(t)$ is the background photon counts.

Here we can easily convert between a discriminator voltage setting to a more practical quantity of pulse counts so that the discriminator threshold used in calculations is given by

$$N_{TH} = \frac{V_{TH}}{R_L \langle I_{PMT} \rangle}, \tag{4.41}$$

where N_{TH} is the discriminator threshold in PMT pulse counts, V_{TH} is the voltage setting of the discriminator threshold, R_L is the load resistance of the pulse counting electronics, and $\langle I_{PMT} \rangle$ is the average PMT current per photon incident on the PMT cathode.

The number of current pulses exiting the PMT is a random variable described by a Poisson distribution with PDF

$$P_{N_D(t)}(n) = \frac{\langle N_D(t) \rangle^n e^{-\langle N_D(t) \rangle}}{n!}. \tag{4.42}$$

As $\langle N_D(t) \rangle$ becomes large, the Poisson distribution becomes difficult to numerically calculate due to the finite bits available for binary representation of large numbers. While the Poisson distribution

still exists for large $\langle N_D(t)\rangle$, it requires the computer to calculate the ratio of rapidly growing factorial and exponential functions. In such cases the PDF is approximated as Gaussian, allowing us to consider a large number of photons incident on the detector

$$P_{N_D(t)}(n) \approx \frac{1}{\sqrt{2\pi\langle N_D(t)\rangle}} \exp\left(\frac{-(t-t_{PMT})^2}{2\langle N_D(t)\rangle}\right). \tag{4.43}$$

The probability that a pulse from the PMT is counted by the timing electronics is then given by the probability that the signal output from the PMT exceeds the discriminator threshold

$$P_{C(t)}(N_{TH}) = \sum_{n=N_{TH}}^{\infty} P_{N_D(t)}(n). \tag{4.44}$$

Once a pulse from the PMT is counted, the timing electronics may have a dead time τ_D during which they cannot register another pulse. This dead time is often longer than the laser pulse, resulting in an additional term deciding whether or not a pulse may be counted by the data acquisition board. It is dependent on both the probability that the PMT current exceeds the discriminator threshold as well as the probability that no PMT pulses were previously counted in the preceding time interval τ_D. Thus the probability that a pulse is registered is given by

$$P_{R(t)} = P_{C(t)}(N_{TH}) \int_{t-\tau_D}^{t} \left(1 - P_{R(\tau)}\right) d\tau. \tag{4.45}$$

While $P_{R(t)}$ is dependent on its own integral, this presents little issue for numerical computation. Note that as the probability of detecting a pulse on the time interval τ_D approaches one, the integral term begins to dominate $P_{R(t)}$, driving the PDF to zero. Since the integral term includes the pulse distribution over a relatively large time frame, it suppresses the variance of the pulse counting statistics. This makes the trailing edge of the photon count histogram particularly useful for timing comparisons in cases of large return signals, due to the low signal uncertainty from shot noise.

Once the probability of detecting a PMT pulse is determined, we then tailor the distribution for the particular timing bins of the data acquisition board. The board has a timing bin width of Δt so that the time stamp of the kth bin is given by $t_k = k\Delta t$. The probability of counting a

photon in the kth bin is then given by

$$P_{B[k]} = \int_{t_{k-1}}^{t_k} P_{R(\tau)} d\tau. \tag{4.46}$$

4.3.3.1 Photon Count Histogram Simulations

Let us consider a single hard target using a high resolution data acquisition board with timing resolution of 27 ps and dead time of 8 ns after registering a pulse. These timing figures are given by the specifications of the HRM-Time data acquisition boards used in the first INPHAMIS prototype. We assume that 2×10^5 photons scattered from the target are incident on the detector after every transmitted pulse. This quantity may be traded with the discriminator threshold settings with some approximate equivalence, though higher photon concentrations serve to reduce variance of shot noise distributions, offering some impact in Eq. (4.42) or (4.43). A detector QE of 0.4 is used with a photon pulse shape described by Eq. (4.39) with $\tau_R = 0.25$ ns and $\tau_F = 2.5$ ns and a timing jitter of 0.35 ns. These PMT characteristics are based on those of the Hammamatsu H7422PA-40. The laser pulse width is 0.45 ns. We then determine the timing board PDF as a function of discriminator threshold (here defined in terms of number of N_{TH}). The resulting PDF of some of these discriminator thresholds are shown in Figure 4.7.

The data shown in Figure 4.7 demonstrates that the photon count PDF is dependent, both in shape and timing, on the relative discriminator threshold/incident photons relationship. When the discriminator threshold is low, the PDF appears to be approximately Gaussian near the front edge. This is expected because the distribution of photons incident on the detector should be approximately Gaussian in time. However, the distribution rapidly falls off on the trailing edge, resulting in an asymmetry in histograms recorded by the HRM-Time. Actual data reflecting this behavior is reported in [53]. Because the discriminator threshold is set low, the probability of counting a photon on the 8 ns dead time interval approaches one. Thus the integral term in Eq. (4.45) dominates the distribution and drives it to zero near the front end of the laser pulse. However, as the discriminator threshold is increased, the integral dominates less. This results in a reduction in photon counting probability at each bin and causes the falling edge to move back in time. The

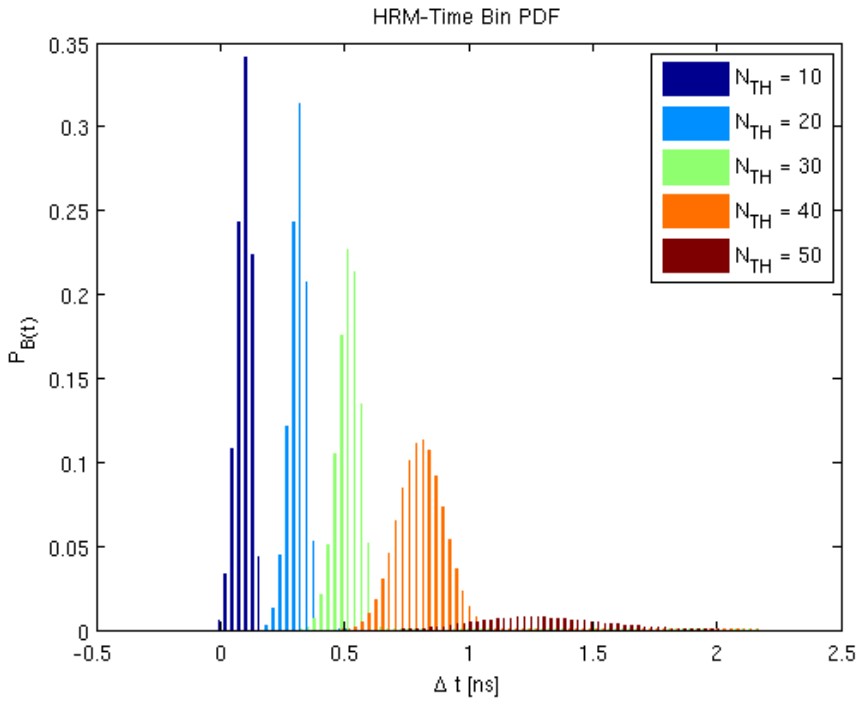

Figure 4.7: Probability distribution function of HRM-Time timing bins as a function of discriminator threshold. As the discriminator threshold increases, the distribution both shifts in time and changes shape.

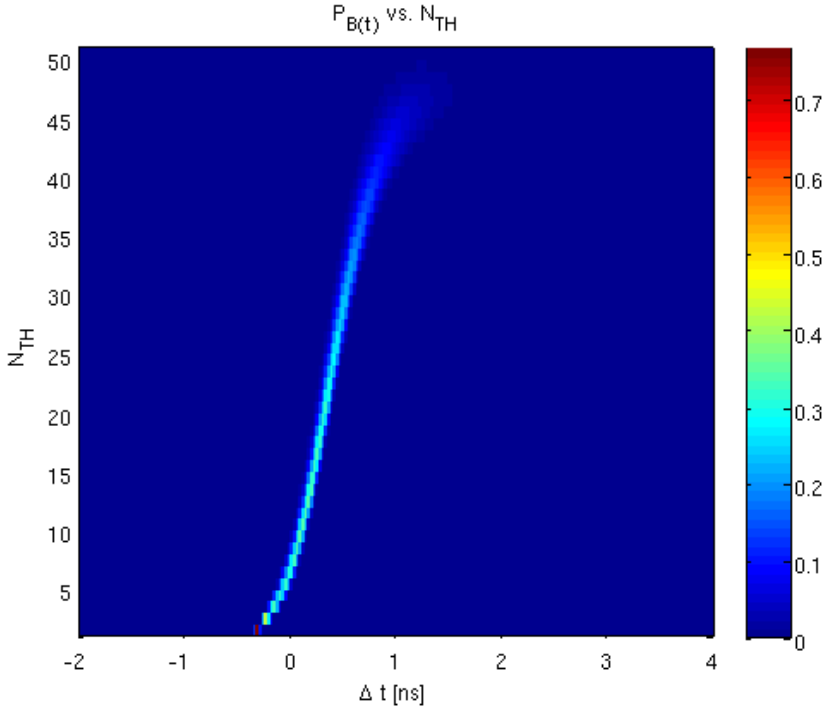

Figure 4.8: Probability distribution function of photon counts in timing bins as a function of discriminator threshold. The shift in timing of the PDF can clearly be seen by the shift in its peak as discriminator threshold changes.

photon count PDF shifts back in time and appears shorter. At high values of N_{TH}, the integral in Eq. (4.45) no longer plays a significant role in the PDF, and the resulting photon PDF reflects the shape of $\langle N_D(t) \rangle$.

A more complete picture of the photon count PDF for this data acquisition board is shown for the described scenario in Figure 4.9. There it can clearly be seen how the photon count PDF shifts in time as a function of discriminator threshold. Indeed the peak of the PDF not only shifts in time, but also this shift is non-linear near the extremes. Thus, the shift is most easily corrected by operating in a restricted dynamic range.

If the lidar system is expected to operate during daytime, we must also consider the effects of background radiation. Due to the unique timing behaviors of the high resolution timing electronics used for the INPHAMIS technique, we should consider its impact. Since Eq. (4.40) makes allowance for the presence of background radiation, we modify the above analysis to include a constant

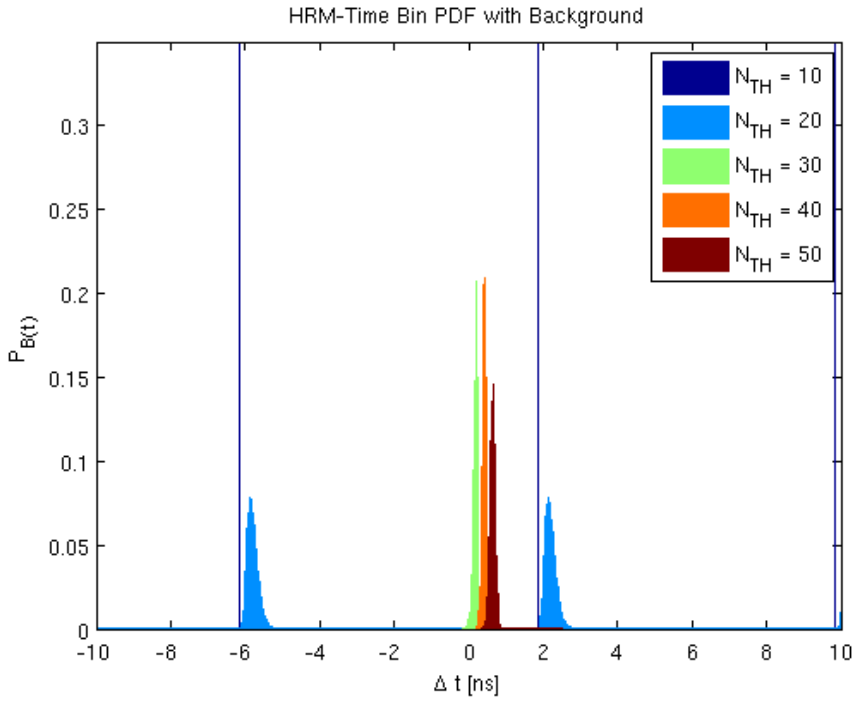

Figure 4.9: Probability distribution function of HRM-Time timing bins as a function of discriminator threshold when with constant background radiation included. Low discriminator thresholds now result in timing histograms that repeat every 8 ns (data acquisition board dead time). As the discriminator threshold increases, the background is suppressed and the signal from the target becomes resolvable.

background radiation arrival rate of 3×10^{16} photons/ns. This specific background arrival rate is exceptionally high (approximately $10^7 W$) but is selected here purely for illustrative purposes. This background level allows us to demonstrate the different effects of background versus discriminator threshold.

The total photon PDF of the timing bins with background as a function of the selected discriminator thresholds are shown in Figure 4.10 and for all integer thresholds from 1 to 50 in Figure 4.8. When the discriminator threshold is low, the probability of registering a pulse from background is one before the end of the board dead time. Thus only backgrounds counts can appear in the photon histogram, and do so every 8 ns. When the discriminator threshold exceeds 25, the periodic histogram from background radiation is sufficiently suppressed so that the photon distribution from the target is now visible. Thus it is clear that discriminator threshold settings

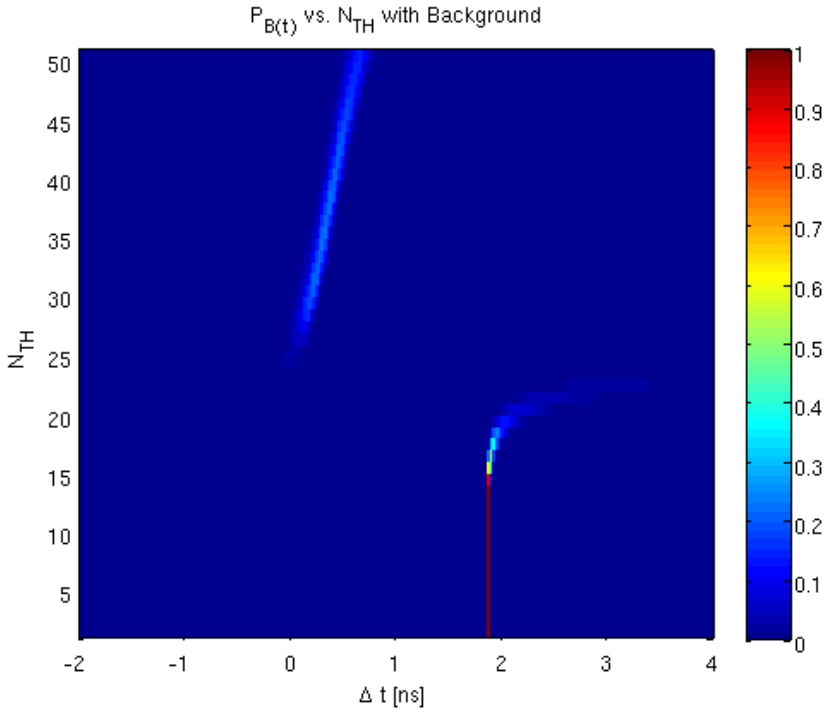

Figure 4.10: Probability distribution function of photon counts in timing bins as a function of discriminator threshold including background. One of the periodic distributions resulting from large background is shown in the bottom right of the plot. When the discriminator threshold exceeds 25, the target signal is resolvable. Again the shift in timing of the PDF can clearly be seen by the shift in its peak as discriminator threshold changes.

should be dictated in part by background radiation levels. Because of the dead time on the data acquisition board, improper setting of the discriminator threshold can result in missing returns from the target entirely. It should be noted that this simulation assumes the background signal levels are less than the return signal. In instances where the background dwarfs return signals, it is unlikely the target's signal can be resolved through adjustment of the discriminator threshold.

The simulations above only considered the presence of a DC background. However, in the two target ranging problem using INPHAMIS, signal from the first target may leak onto the detector while attempting to range to the second target. The most general case where this becomes an issue is when the first target is partially depolarizing. We can regard this first signal as background, only now with time dependence. The ability of the system to resolve the second surface will be driven by suppression of signal from the first surface. Again, through adjusting discriminator threshold,

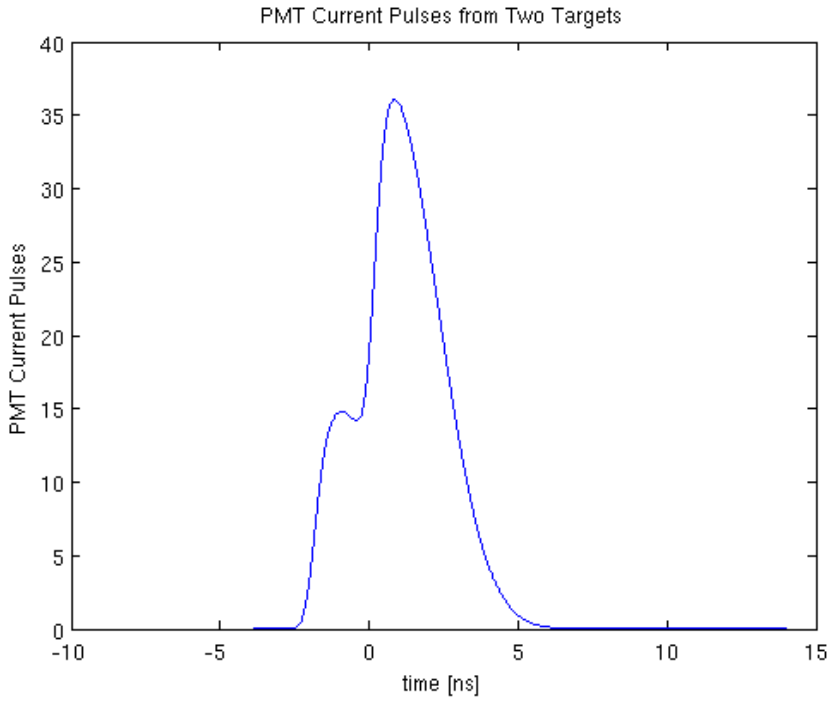

Figure 4.11: PMT current pulse distribution from two targets separated by 30 cm (2 ns temporal separation). The return from the first target is suppressed so that it contains half as many photons as the return from the second surface.

we should be able to optimally detect the second surface. In these cases the discriminator must be set high enough, that the integral term in Eq. (4.45) does not dominate before the arrival of the laser pulse from the second target.

Consider a case where two surfaces are separated by 30 cm (2 ns by time of flight) and the received photons from the first surface are suppressed to half of the photons from the second surface. In Figure 4.11 we show the resulting PMT output current pulse distribution. The two distributions distinctively overlap. If the discriminator threshold is not set sufficiently high, the timing electronics will always trigger on the first surface, so that no photons would be counted from the second surface. The resulting photon count distributions are shown for a selected discriminator thresholds in Figure 4.12 and for all simulated thresholds in Figure 4.13. The return from the second surface is only visible when the discriminator is set high enough to miss most of the returns from the first surface.

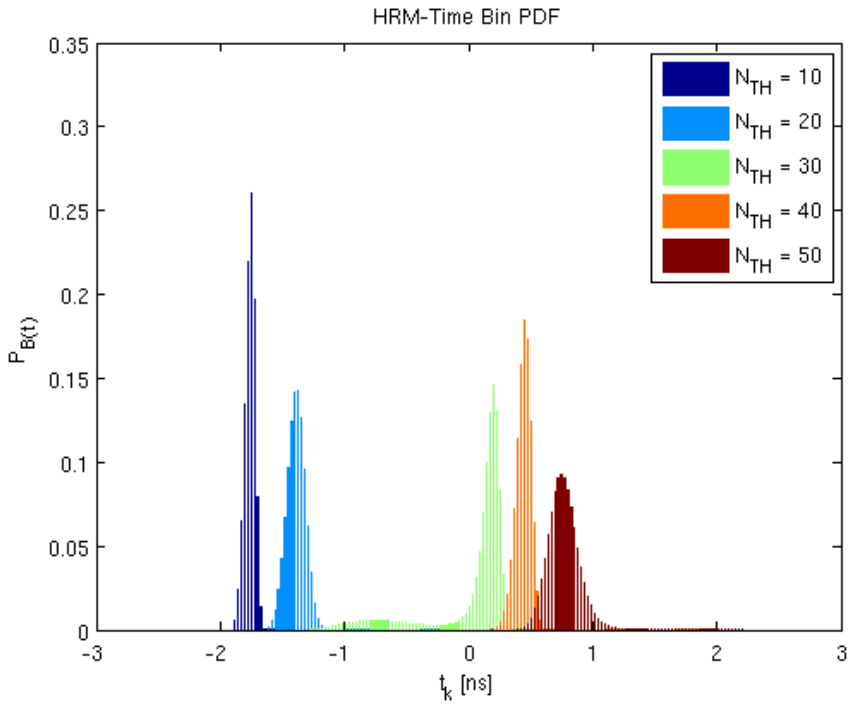

Figure 4.12: Photon count distribution of two targets for various discriminator threshold settings. As the threshold is raised, returns from the second target become visible. At $N_{TH} = 30$, contributions from both targets can be seen in the distribution.

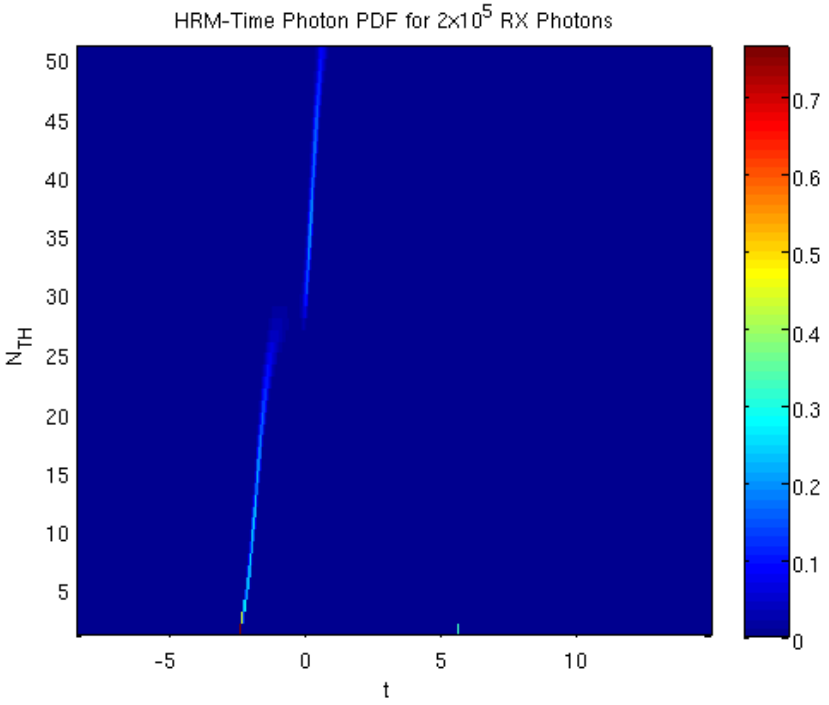

Figure 4.13: Photon count distribution of two targets as a function of discriminator threshold settings. Only after the threshold exceeds 26 pulses is the second target visible in the photon count PDF.

As direct detection lidar pushes to shorter timing resolution, it becomes clear that new issues must be considered. When dynamic range of signals or discriminator threshold change, the photon distribution will shift later in time. We must consider the level of the discriminator threshold needed to ignore background and ensure photons from targets are registered by the data acquisition electronics. The specifics of this problem invariably must be known to obtain optimal system solutions, but the above theory provides a useful baseline for solving these problems.

Chapter 5

Polarization Effects in Lidar Instruments

While measurement techniques can be developed for any number of polarization measurements, the technique's ability to resolve its desired data product is limited by the polarization corrupting effects of the instrument. In some cases, these effects can be corrected with additional hardware and post processing, while others require thorough and careful system design to ensure the instrument meets the accuracy requirements of the mission.

5.1 Characterizing the Instrument

The most complete information about the polarization performance of an instrument is given in its Mueller matrix. The process of measuring a Mueller matrix requires transmission of four polarization states and measurement of the resulting exit polarization state

$$\vec{S}_{out} = \mathbf{M_{sys}} \vec{S}_{in}. \tag{5.1}$$

The necessary input polarization states for this measurement are not unique. The method employed here uses input states of horizontal, vertical, 45° and left-hand circular polarization. The system Mueller matrix is then given by [18]

$$\vec{C}_1 = \frac{1}{2}\left(\vec{S}^h_{out} + \vec{S}^v_{out}\right), \tag{5.2}$$

$$\vec{C}_2 = \frac{1}{2}\left(\vec{S}^h_{out} - \vec{S}^v_{out}\right), \tag{5.3}$$

$$\vec{C}_3 = \vec{S}^{45}_{out} - \vec{C}_1, \tag{5.4}$$

$$\vec{C}_4 = \vec{S}^{lhc}_{out} - \vec{C}_1, \tag{5.5}$$

where $\vec{C}_i$ is the *ith* column in the 4x4 system Mueller matrix and the superscripts h, v, 45, and lhc on the Stokes vectors denote the corresponding input polarization state to the system.

Applying the above method to characterize lidar transmitters is relatively straight-forward. However, characterizing an optical system with large optics such as a telescope, presents a substantial problem for most lidars. The most accurate way to characterize the receiver system is to do so through the lidar operation. The scattering matrix of atmospheric molecules is well known. This matrix is nearly polarization preserving, described by the matrix in Eq. (3.5) with $d = 0.00727$ for the central Cabannes line at 532 nm. We then operate the lidar system by transmitting four polarization states described above and measure the resulting Stokes vectors in the receiver. The Mueller matrix measurement process is described

$$\vec{S}_{out} = \mathbf{M}_{sys}\mathbf{F}_{mol}\vec{S}_{in}. \tag{5.6}$$

The system Mueller matrix $\mathbf{M}_{sys}$ can be determined independent of the molecular scattering matrix $\mathbf{F}_{mol}$ by adapting the relations in Eq. (5.2) to account for the depolarizing effect of the molecular return

$$\vec{C}_1 = \frac{1}{2}\left(\vec{S}^h_{out} + \vec{S}^v_{out}\right), \tag{5.7}$$

$$\vec{C}_2 = \frac{1}{2(1-d_{mol})}\left(\vec{S}^h_{out} - \vec{S}^v_{out}\right), \tag{5.8}$$

$$\vec{C}_3 = \frac{1}{1-d_{mol}}\left(\vec{S}^{45}_{out} - \vec{C}_1\right), \tag{5.9}$$

$$\vec{C}_4 = \frac{1}{1-2d_{mol}}\left(\vec{S}^{lhc}_{out} - \vec{C}_1\right), \tag{5.10}$$

To avoid uncertainty in the scattering depolarization caused by aerosols, we use returns in the lower stratosphere. Also this characterization is only performed under clear sky conditions since clouds tend to introduce variable extinction between and within Stokes vector measurements.

5.1.1 Cloude Filtering

When the optical system Mueller matrix is measured through the above process, the measurement inevitably contains noise. Generally this means the resultant matrix is not a true Mueller

matrix. A Cloude filter determines the closest realizable Mueller matrix to the measured matrix using unique properties of the covariance matrix [27].

In common coherent sensors such as radar and coherent lidar, the covariance matrix is used to express the coherency of the received radiation. However, we also find that the unique properties of the covariance matrix also allow us to find the closest true Mueller matrix to a noisy measurement.

The covariance matrix $\mathbf{T}_c$ of a true Mueller matrix $\mathbf{M}$ must be Hermitian and positive semi definite, so that all eigen values of $\mathbf{T}_c$ are real and positive or zero. The covariance matrix of the measured Mueller matrix is given in compact form by [22]

$$\mathbf{T}_c = \frac{1}{2}\sum_{i=1}^{4}\sum_{j=1}^{4} M_{ij}\sigma_{i-1} \otimes \sigma_{j-1}^{*}, \tag{5.11}$$

where $\mathbf{T}_c$ is the covariance matrix of the measured Mueller matrix $\mathbf{M}$ composed of elements M_{ij} The terms σ_i where $i = 0, 1, 2, 3$ are Pauli Matrices. This compact formula may also be written in terms of individual matrix elements which are given incorrectly in [27]. The correct formulas are given below.

$$T_{c11} = \frac{1}{2}\left(M_{11} + M_{22} + M_{33} + M_{44}\right), \tag{5.12}$$

$$T_{c12} = \frac{1}{2}\left(M_{12} + M_{21} - i(M_{34} - M_{43})\right), \tag{5.13}$$

$$T_{c13} = \frac{1}{2}\left(M_{13} + M_{31} + i(M_{24} - M_{42})\right), \tag{5.14}$$

$$T_{c14} = \frac{1}{2}\left(M_{14} + M_{41} - i(M_{23} - M_{32})\right), \tag{5.15}$$

$$T_{c21} = T^*_{c12}, \tag{5.16}$$

$$T_{c22} = \frac{1}{2}\left(M_{11} + M_{22} - M_{33} - M_{44}\right), \tag{5.17}$$

$$T_{c23} = \frac{1}{2}\left(M_{23} + M_{32} + i(M_{14} - M_{41})\right), \tag{5.18}$$

$$T_{c24} = \frac{1}{2}\left(M_{24} + M_{42} - i(M_{13} - M_{31})\right), \tag{5.19}$$

$$T_{c31} = T^*_{c13}, \tag{5.20}$$

$$T_{c32} = T^*_{c23}, \tag{5.21}$$

$$T_{c33} = \frac{1}{2}\left(M_{11} - M_{22} + M_{33} - M_{44}\right), \tag{5.22}$$

$$T_{c34} = \frac{1}{2}\left(M_{34} + M_{43} + i(M_{12} - M_{21})\right), \tag{5.23}$$

$$T_{c41} = T^*_{c14}, \tag{5.24}$$

$$T_{c42} = T^*_{c24}, \tag{5.25}$$

$$T_{c43} = T^*_{c34}, \tag{5.26}$$

$$T_{c44} = \frac{1}{2}\left(M_{11} - M_{22} - M_{33} + M_{44}\right), \tag{5.27}$$

The covariance matrix may then be decomposed into the form [66]

$$\mathbf{T}_c = \mathbf{W}\mathbf{\Lambda}\mathbf{W}^\dagger, \tag{5.28}$$

where $\mathbf{W}$ is a matrix of the eigen vectors of $\mathbf{T}_c$ and $\mathbf{\Lambda}$ is a diagonalized matrix of eigen values of $\mathbf{T}_c$. If any eigen value λ_i is negative, it is set to zero giving the filtered eigen value matrix $\tilde{\mathbf{\Lambda}}$ which is positive semidefinite. The filtered covariance matrix is then obtained by substituting $\tilde{\mathbf{\Lambda}}$ into Eq. (5.28) for $\mathbf{\Lambda}$

The closeness of the measured matrix to a true Mueller matrix is given by the magnitude of the ratio of the most negative and most positive covariance matrix eigenvalues.

Finally the filtered Mueller matrix may be obtained by converting back from the filtered covariance matrix

$$\tilde{M}_{11} = \frac{1}{2}(\tilde{T}_{c11} + \tilde{T}_{c22} + \tilde{T}_{c33} + \tilde{T}_{c44}), \tag{5.29}$$

$$\tilde{M}_{12} = Re(\tilde{T}_{c12}) + Im(\tilde{T}_{c34}), \tag{5.30}$$

$$\tilde{M}_{13} = Re(\tilde{T}_{c13}) + Im(\tilde{T}_{c24}), \tag{5.31}$$

$$\tilde{M}_{14} = Re(\tilde{T}_{c14}) + Im(\tilde{T}_{c23}), \tag{5.32}$$

$$\tilde{M}_{21} = Re(\tilde{T}_{c21}) - Im(\tilde{T}_{c34}), \tag{5.33}$$

$$\tilde{M}_{22} = \frac{1}{2}(\tilde{T}_{c11} + \tilde{T}_{c22} - \tilde{T}_{c33} - \tilde{T}_{c44}), \tag{5.34}$$

$$\tilde{M}_{23} = Re(\tilde{T}_{c23}) + Im(\tilde{T}_{c41}), \tag{5.35}$$

$$\tilde{M}_{24} = Re(\tilde{T}_{c24}) + Im(\tilde{T}_{c13}), \tag{5.36}$$

$$\tilde{M}_{31} = Re(\tilde{T}_{c31}) - Im(\tilde{T}_{c42}), \tag{5.37}$$

$$\tilde{M}_{32} = Re(\tilde{T}_{c32}) - Im(\tilde{T}_{c41}), \tag{5.38}$$

$$\tilde{M}_{33} = \frac{1}{2}(\tilde{T}_{c11} - \tilde{T}_{c22} + \tilde{T}_{c33} - \tilde{T}_{c44}), \tag{5.39}$$

$$\tilde{M}_{34} = Re(\tilde{T}_{c34}) + Im(\tilde{T}_{c21}), \tag{5.40}$$

$$\tilde{M}_{41} = Re(\tilde{T}_{c41}) - Im(\tilde{T}_{c23}), \tag{5.41}$$

$$\tilde{M}_{42} = Re(\tilde{T}_{c42}) - Im(\tilde{T}_{c13}), \tag{5.42}$$

$$\tilde{M}_{43} = Re(\tilde{T}_{c43}) - Im(\tilde{T}_{c21}), \tag{5.43}$$

$$\tilde{M}_{44} = \frac{1}{2}(\tilde{T}_{c11} - \tilde{T}_{c22} - \tilde{T}_{c33} + \tilde{T}_{c44}). \tag{5.44}$$

5.2 Hardware Compensation

After we obtain an optical system Mueller matrix, it can be decomposed into its fundamental polarization effects [42]. Retarding effects are common in lidar systems, often skewing depolar-

ization estimates and coupling polarized solar background into the detector channel. In order to minimize these effects, a compensator may be constructed to cancel the phase shift imposed by the optical system. The improved polarized background rejection and reduced signal corrupting effects result in improved SNR and better instrument accuracy.

To improve the polarization performance of a lidar, matrices representing compensators are added before the transmitter and after the receiver optics

$$\vec{S}_{RX} = \mathbf{M}_{RXcomp}\mathbf{M}_{RX}\mathbf{F}\mathbf{M}_{TX}\mathbf{M}_{TXcomp}\vec{S}_{TX}. \tag{5.45}$$

The system Mueller matrices may be decomposed into depolarizing, diattenuating and retarding Mueller matrices [42]. To cancel retarding effects in the optical system, the compensator must be the inverse of the optical system retarder matrix $\mathbf{M}_R$. Equivalently, the compensator is a retarder with its fast axis aligned to that of the system retarder but with the opposite phase shift. This realization generally requires a combination of two quarter wave plates and one half wave plate. This combination can be used to construct any arbitrary retarder [82, 4].

A general, arbitrary, elliptical retarder may be described as the combination of a linear wave plate of orientation φ and phase shift Γ and a linear rotator of angle ϑ [4]

$$\mathbf{M}_R = \mathbf{M}_{WP}\left(\varphi, \Gamma\right)\mathbf{R}\left(\vartheta\right). \tag{5.46}$$

This description effectively decomposes the total retarder into a linear retarding effect, $\mathbf{M}_{WP}\left(\varphi, \Gamma\right)$, which is a rotation about a linear polarization, and a circular retarding effect, $\mathbf{R}\left(\vartheta\right)$, which is strictly a linear rotation. Note that this decomposition can be performed so the matrices are in the opposite order, but the arguments of the matrices will not be identical between the two decompositions.

To cancel the effect of a retarder, we insert an optical component whose Mueller matrix is the inverse of the retarder in the optical system. Equivalently, the element must perform the opposite operations of the linear wave plate and rotator, in the opposite order.

$$\mathbf{M}_{comp} = \mathbf{M}_R^{-1} = \mathbf{R}\left(-\vartheta\right)\mathbf{M}_{WP}\left(\varphi, -\Gamma\right) \tag{5.47}$$

An arbitrary retarder constructed using a combination of two quarter-wave plates and one half-wave plate is given by [82, 4].

$$\mathbf{M}_{WP}\left(\varphi,\Gamma\right)\mathbf{R}\left(\vartheta\right)=\mathbf{Q}\left(\varphi+\frac{\pi}{4}\right)\mathbf{Q}\left(\varphi+\frac{\pi}{4}+\frac{\Gamma}{2}\right)\mathbf{H}\left(\varphi+\frac{\pi+\Gamma}{4}-\frac{\vartheta}{2}\right) \tag{5.48}$$

where $\mathbf{Q}$ and $\mathbf{H}$ are quarter-wave and half-wave plates respectively and their arguments are the orientation of the wave plates' fast axes.

Using Eq. (5.47) and (5.48), we can then write the inverse retarder matrix as a combination of wave plates.

$$\mathbf{M}_{R}^{-1}=\mathbf{H}\left(\varphi+\frac{\pi-\Gamma}{4}-\frac{\vartheta}{2}\right)\mathbf{Q}\left(\varphi+\frac{\pi}{4}-\frac{\Gamma}{2}\right)\mathbf{Q}\left(\varphi+\frac{\pi}{4}\right), \tag{5.49}$$

which can be derived using the communitive properties below[4].

$$\mathbf{M}\left(\varphi,\Gamma\right)=\mathbf{Q}\left(\varphi+\frac{\pi}{4}\right)\mathbf{Q}\left(\varphi+\frac{\pi}{4}+\frac{\Gamma}{2}\right)\mathbf{H}\left(\varphi+\frac{\pi+\Gamma}{4}\right) \tag{5.50}$$

$$\mathbf{R}\left(\alpha\right)\mathbf{H}\left(\gamma\right)=\mathbf{H}\left(\gamma+\frac{\alpha}{2}\right) \tag{5.51}$$

$$\mathbf{H}\left(\gamma\right)\mathbf{R}\left(\alpha\right)=\mathbf{H}\left(\gamma-\frac{\alpha}{2}\right) \tag{5.52}$$

$$\mathbf{Q}\left(\alpha\right)\mathbf{H}\left(\gamma\right)=\mathbf{H}\left(\gamma\right)\mathbf{Q}\left(\gamma-\alpha\right) \tag{5.53}$$

$$\mathbf{H}\left(\gamma\right)\mathbf{Q}\left(\alpha\right)=\mathbf{Q}\left(\gamma-\alpha\right)\mathbf{H}\left(\gamma\right) \tag{5.54}$$

$$\tag{5.55}$$

The compensator design in Eq. (5.48) works well for the lidar receiver system because the HWP, as the last element, can be used to provide a linear rotation adjustment for alignment of incoming polarizations to the polarizer. For the transmitter, the compensator precedes the optical system. We would like to use the HWP to rotate the outgoing linear polarization. The relationships defined above in Eq. (5.50) can then be used with the inverse retarder definition in Eq. (5.49) to give the transmitter compensator design as follows:

$$M_{comp}=\mathbf{Q}\left(\varphi+\frac{\pi}{4}-\vartheta\right)\mathbf{Q}\left(\varphi+\frac{\pi}{4}-\frac{\Gamma}{2}-\vartheta\right)\mathbf{H}\left(\varphi+\frac{\pi-\Gamma}{4}-\frac{\vartheta}{2}\right) \tag{5.56}$$

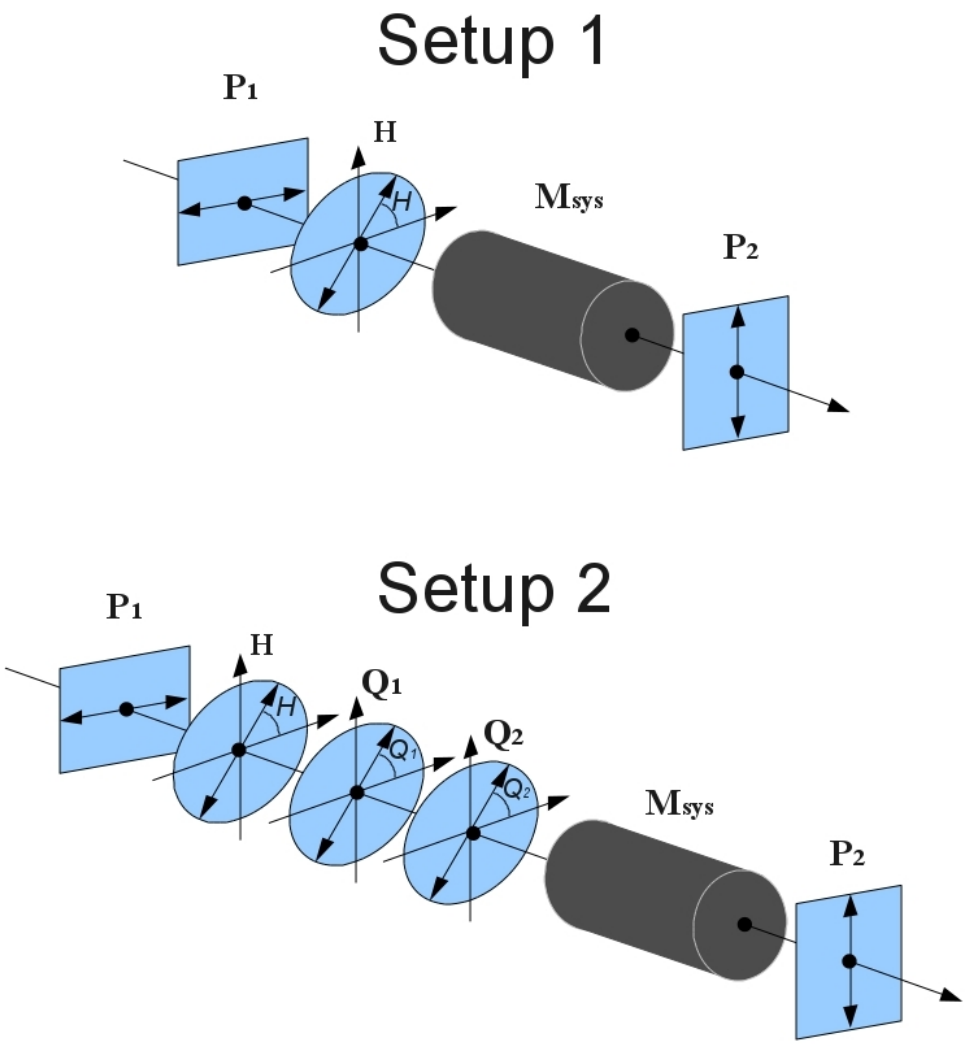

Figure 5.1: Optical setup for compensator optimization on the transmit side. Initially the two QWPs are omitted to find LiLo of the optical system. The QWPs should be mounted in such a way to rotate $\mathbf{Q}_1$ independently and $\mathbf{Q}_1$ and $\mathbf{Q}_2$ in unison.

5.2.1 Compensation Optimization Technique

While measuring the optical system Mueller matrix provides useful information about system polarization effects, the practice of measuring a Mueller matrix can be time consuming. Furthermore, compensator design from the measured matrix rarely results in precise alignment. For actual implementation, we require an optimization technique that can be employed in the field.

The procedure developed for compensator optimization here uses the setup described in Figure 5.1. Initially, a laser passes through a polarizer $\mathbf{P}_1$ (which remains fixed and is used to

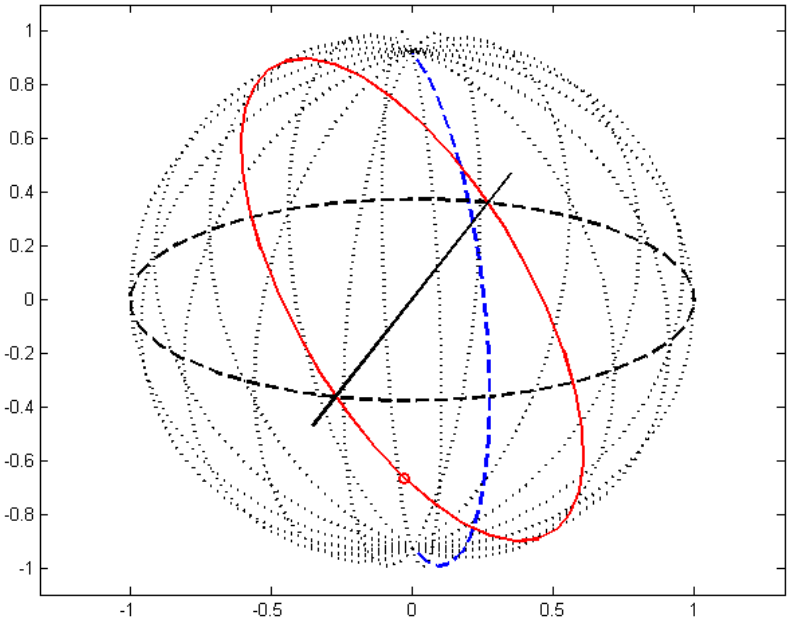

Figure 5.2: Poincarè Sphere for the output of optical system $\mathbf{M}_{sys}$. The red line indicates the how the equator (linear polarizations) is transformed by the system. The blue dashed meridian corresponds the S_1 horizontal direction (horizontal linear polarization is where the blue meridian meets the equator). The circle is the resulting output polarization for an input of horizontal linear polarization. The solid black line is the LiLo axis for $\mathbf{M}_{sys}$.

ensure the light is linearly polarized) and HWP to control the linear polarization angle. It then passes through the optical system, through a polarizer $\mathbf{P}_2$ and onto a detector. As a visual guide for this process, the resulting output polarizations from linearly polarized inputs after the HWP are shown on the output on the Poincarè Sphere. In Figure 5.2 the resulting output polarizations from the equator (linear inputs) are shown in red. The output polarization corresponding to linear horizontal input (where the blue meridian crosses the equator) is shown as a circle. In Figure 5.2 Setup 1 is used.

The first task requires that we find the linear input polarization that gives a linear output polarization (referred to here as LiLo) in the optical system. Note that LiLo is not necessarily the eigen polarization of the system, as the linear output may be rotated relative to the input polarization. To find LiLo we rotate the HWP and $\mathbf{P}_2$ to find the HWP angle that allows maximum

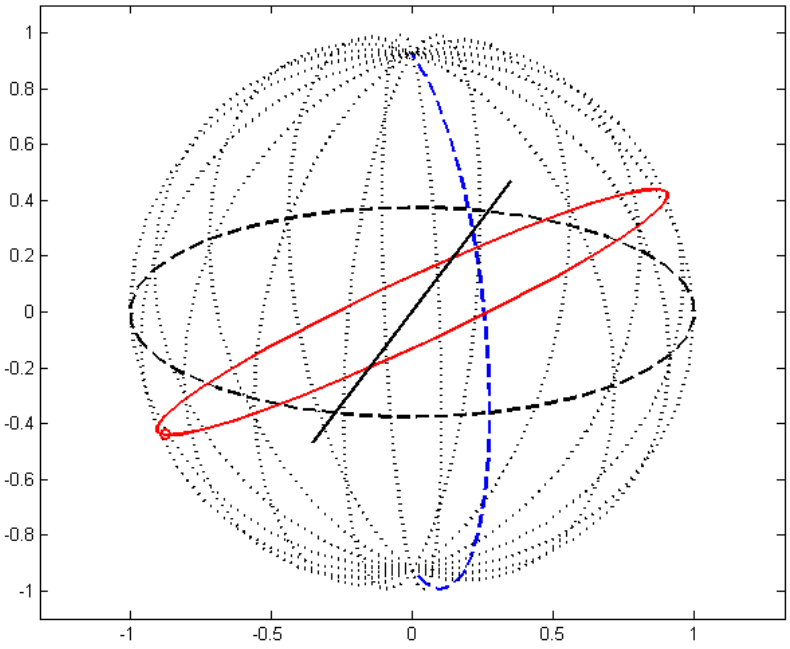

Figure 5.3: Poincarè Sphere for the output of the 2 QWP compensator and optical system $\mathbf{M}_{sys}$. The red line indicates the resulting output Stokes vectors of linear input polarizations. The solid black line is still the LiLo axis for $\mathbf{M}_{sys}$ but does not correspond to LiLo for the total system.

rejection by $\mathbf{P}_2$. On the Poincarè Sphere, this polarization is where the red output crosses the equator. It is marked by the black line in Figure 5.2.

Once LiLo is achieved, the two QWPs $\mathbf{Q}_1$ and $\mathbf{Q}_2$ are inserted into the system as shown in Setup 2 of 5.1. The compensator design uses two cage system mounts so that rotating the $\mathbf{Q}_2$ mount rotates both QWPs, but $\mathbf{Q}_1$ may be rotated independently in its mount. When the compensator is inserted into the optical system, the two QWPs should be configured so that their fast axes neither align (causing the compensator to act as a HWP) nor offset by 90° (causing their phase shifts to cancel). Once the QWPs are inserted, the total Mueller matrix changes. This is shown for randomized QWP angles in Figure 5.3. At this point, the previously determined LiLo axis of $\mathbf{M}_{sys}$ is not the same as the total system. To obtain a total system with the same LiLo axis as before, we must adjust the two QWPs so that their LiLo output polarization is the same as the

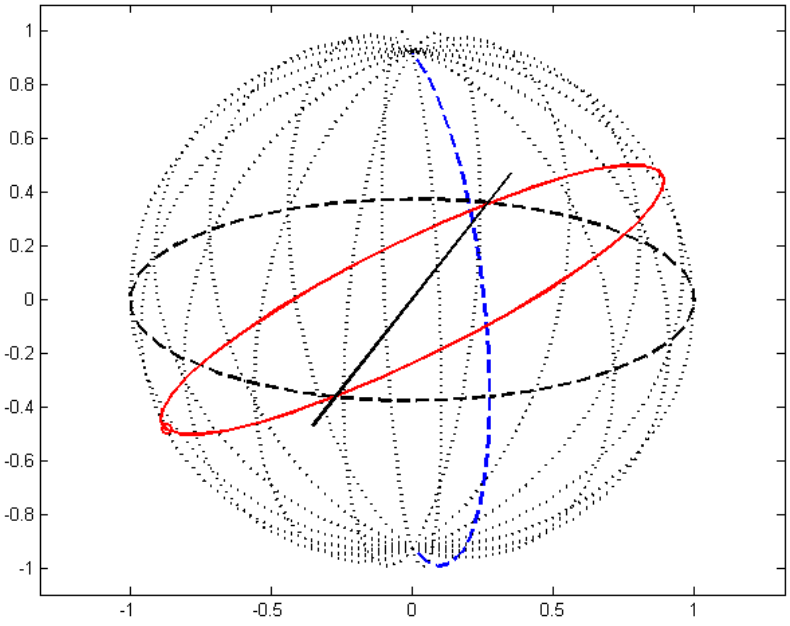

Figure 5.4: Poincarè Sphere for the output of the 2 QWP compensator and optical system $\mathbf{M}_{sys}$ after aligning the QWP rotation angles in unison. The red line indicates the resulting output Stokes vectors of linear input polarizations. The solid black line is now the LiLo axis for both $\mathbf{M}_{sys}$ the total system.

LiLo input on $\mathbf{M}_{sys}$. In Eq. (5.56) we see that the orientation of the linear wave plate is defined by the offset of the the two QWPs in the compensator. Thus we re-achieve LiLo by rotating $\mathbf{Q}_1$ and $\mathbf{Q}_2$ together, while adjusting the HWP to maximize rejection. This returns us to the same linear output polarization as in the previous step. The Poincarè Sphere is then shown for this configuration in Figure 5.4.

Once LiLo of the QWPs and system has been aligned, we want to use the QWPs to impose an equal and opposite phase shift. On the Poincarè Sphere, this rotates the red outputs back onto the equator. In Eq. (5.56) the argument of $\mathbf{Q}_1$ contains the phase shift term Γ, so we adjust this by rotating $\mathbf{Q}_1$. In practice, this results in the output polarization walking off LiLo, so initially, intensity through $\mathbf{P}_2$ should increase. As $\mathbf{Q}_1$ is rotated, $\mathbf{P}_2$ should continue to be adjusted to minimize the intensity on the detector. As the compensator gets close to optimized, the minimized

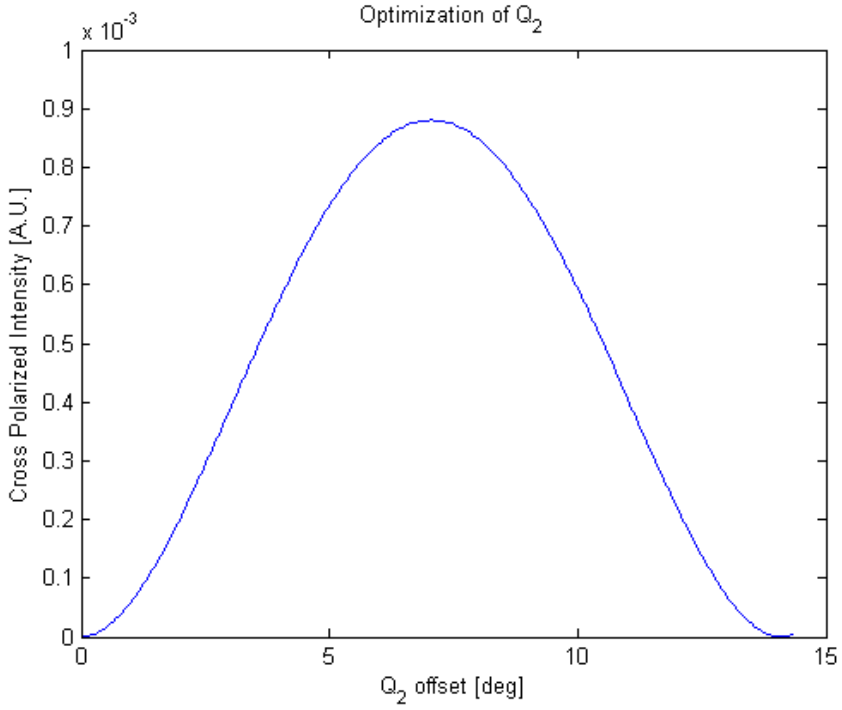

Figure 5.5: Minimum transmission through $\mathbf{P}_2$ as a function of $\mathbf{Q}_1$ rotation angle. Initially the cross polarized signal increases as the input polarization departs from LiLo, but when the phases of the compensator and optical system cancel enough, all linear input polarizations give linear output polarizations and the rejection by the polarizer is zero again.

signal through $\mathbf{P}_2$ will begin to decrease, resulting in the signal shown in Figure 5.5 for the simulated system. When the signal is zero, the compensator is optimized. This results in a Poincarè Sphere shown in 5.6 where the red output polarizations resulting from linear inputs now lie on the equator. Note that the circle corresponding to horizontal input polarization is not on the blue meridian. This means that there is still a linear rotation from the optical system that has not been canceled. However, the HWP can adjust for this rotational offset. After adjusting the HWP, any input polarization will now exit the total system without changing state.

In addition to making compensators easier to implement in the field this procedure can be used to characterize the system retarding effects. By reading off the orientations of the two QWPs

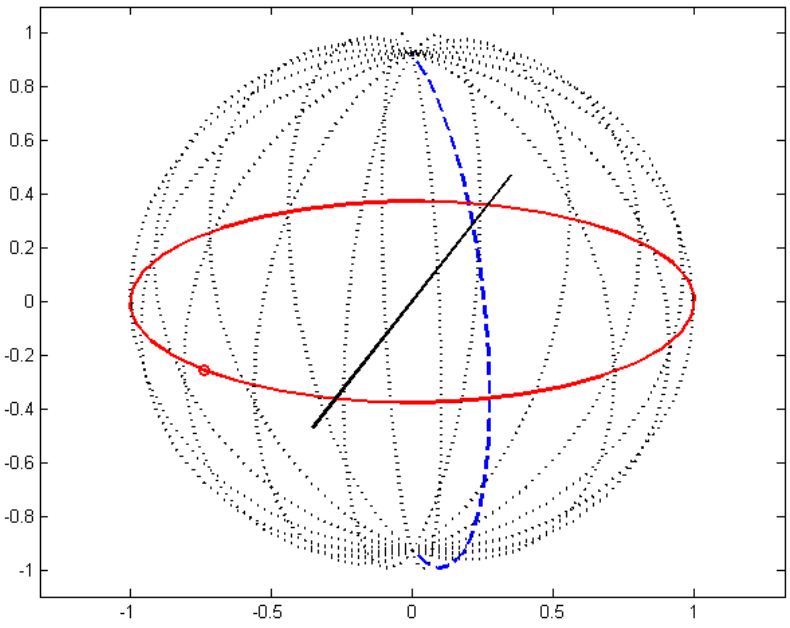

Figure 5.6: Poincarè Sphere for the output of the 2 QWP compensator and optical system $\mathbf{M}_{sys}$ after aligning $\mathbf{Q}_1$ rotation angle. The red line indicates the resulting output Stokes vectors of linear input polarizations. These outputs are now all linear polarizations (on the equator) and only modified in rotation angle.

and the HWP the system parameters can be determined using (5.56) and are given by

$$\Gamma = 2\left(Q_2 - Q_1\right), \tag{5.57}$$

$$\vartheta = 2\left(H - Q_1 - \frac{\Gamma}{4}\right), \tag{5.58}$$

$$\varphi = Q_2 + \vartheta - \frac{\pi}{4}, \tag{5.59}$$

where Q_1, Q_2 and H are the rotation angles of the first and second QWPs and the HWP in Setup 2 of Figure 5.1.

5.3 Instrument Error in Depolarization

Instrument effects of depolarization, diattenuation and retardance all have the potential to introduce error to depolarization measurements. Providing the analytic expressions for the impact

of all polarization effects on this measurement is impractical. Additional terms will arise with the addition of each polarization effect, making the expression difficult to interpret. It is generally more practical to evaluate a system numerically using the SVLE to provide a picture of polarization sensitives. For the purpose of illustrating sensitivity to polarization effects in depolarization measurements, we consider a receiver with a folding mirror that exhibits retardance.

Consider a conventional polarization lidar where a single linear polarization is transmitted and the parallel and perpendicular polarization channels are detected. The instrument description for the system is given in Chapter 4 by Eq. (4.1), (4.2) and (4.3). Let us assume that the scatterers under investigation are randomly oriented and axially symmetric so that the scattering matrix is given by (3.5) and that the lidar operates in a linear transmit polarization state.

After scattering, the degree of polarization (DOP) is scaled by a factor $(1-d)$ so that the Stokes vector has the normalized form

$$\vec{S}_{\mathbf{F}} = \begin{bmatrix} 1 \\ (1-d) \\ 0 \\ 0 \end{bmatrix}, \tag{5.60}$$

where the subscript $\mathbf{F}$ indicates this is the polarization state immediately after scattering in Eq. (2.1). The light is then collected and as it passes through the optical system, reflects off the mirror in question. A phase shift occurs between eigen polarizations of the mirror. In general, the incident linear polarization becomes elliptical. Also, the linear orientation angle will change. The mirror acts as a linear retarder of phase shift Γ_R with fast axis ϕ_R. After reflection, the initially linearly polarized light will have a circular polarization component given by the last element of the Stokes vector

$$S_3 = (1-d)\sin 2\phi_R \sin \Gamma_R. \tag{5.61}$$

Because both the S_1 and S_2 terms of the Stokes vector correspond to linear polarizations, there is always some coordinate frame q' related to the previous coordinate frame q through linear

rotation such that S_2' is zero. Thus we will describe the Stokes vector after reflection off the mirror in the frame q' which is given as

$$\vec{S'}_{\mathbf{m}} = \begin{bmatrix} 1 \\ (1-d)\cos\Gamma \\ 0 \\ (1-d)\sin\Gamma \end{bmatrix}, \tag{5.62}$$

where Γ is twice the polarization ellipticity angle of the polarization in the q' coordinate frame. Because of this change in coordinate frames, the parallel and perpendicular polarization measurements are made by a horizontal and vertical polarizer respectively so that

$$\begin{bmatrix} N_{||} \\ N_{\perp} \end{bmatrix} \propto \begin{bmatrix} 1+S_1' \\ 1-S_1' \end{bmatrix} = \begin{bmatrix} 1+(1-d)\cos\Gamma \\ 1-(1-d)\cos\Gamma \end{bmatrix}. \tag{5.63}$$

Absent of system effects, the depolarization of randomly oriented scatterers can be determined using only this two channel measurement and is given by [26]

$$d_M = \frac{2N_{\perp}}{N_{\perp}+N_{||}}, \tag{5.64}$$

where the subscript M indicates measured depolarization.

When we evaluate the results given in Eq. (5.63) we find the measured depolarization has an error dependency given by the ellipticity of the polarization after reflection off the mirror

$$d_M = 1 - \cos\Gamma + d\cos\Gamma. \tag{5.65}$$

In order to relate this error back to the polarization effects exhibited by the mirror, we equate the S_3 terms of the Stokes vector after reflecting off the mirror Eq. (5.61) and (5.62). This gives Γ as a function of the mirror polarization parameters.

$$\sin\Gamma = \sin 2\phi_R \sin\Gamma_R. \tag{5.66}$$

Depolarization estimates can clearly be skewed by polarization effects in the receiver. The fact that the mirror in this example transforms the linearly polarized state to elliptical, means there is no polarizer rotation angle that will fully reject or accept the polarized state. The circular polarization component appears to be unpolarized using this polarization technique.

5.3.1 Software Correction

Software correction of polarization effects in the lidar is an attractive solution since it is affordable and can be applied to old data. When the scattering medium is strictly depolarizing, this software post processing algorithm can be used to remove error from receiver depolarization, receiver retardance, polarization plane misalignment between transmitter and receiver, and partial polarization of the transmitted laser[32].

The optical path from transmitter to detector is given by the SVLE in Eq. (2.11) and the description of depolarization lidar operation in Chapter 4.

For our analysis, modification of polarization by atmospheric transmission will be ignored, and the transmitter is assumed to be properly designed or compensated to ensure the outgoing polarization state is linear. We also assume linear polarization is transmitted with a misalignment α to the parallel receiver channel with degree of polarization P_{TX} and thus write the transmitted Stokes vector

$$\vec{S}_{TX} = \begin{bmatrix} 1 \\ P_{TX}\cos 2\alpha \\ P_{TX}\sin 2\alpha \\ 0 \end{bmatrix}. \tag{5.67}$$

We will assume that all scatterers studied here are randomly oriented and axially symmetric so the backscattered light is partially polarized according to the single scattering matrix below[25].

$$\mathbf{F}(\pi, z) = \begin{bmatrix} 1 & 0 & 0 & 0 \\ 0 & 1-d_a(z) & 0 & 0 \\ 0 & 0 & d_a(z)-1 & 0 \\ 0 & 0 & 0 & 2d_a(z)-1 \end{bmatrix} \tag{5.68}$$

The subscript a denotes that this depolarization term is strictly the result of atmospheric scattering and the argument z indicates the altitude of the scattering event.

The measured depolarization, d_M may be calculated from the detected parallel and perpendicular polarization signals and is given in Eq. (5.64) [26] which is equal to d_a when $\mathbf{M_{RX}}$ is an

identity.

Here we assume the signals have been properly scaled to account for detector mismatch. The terms $N_\perp(z)$ and $N_\parallel(z)$ are the first elements of the perpendicular and parallel channel Stokes vectors, and thus are the received photon counts on the respective channels.

A single ray path through the receiver will accumulate phase shifts specific to its particular path. When the phases of all the optical paths add coherently, a net phase shift results and is described in the system as a retarder. When the phases of all paths add incoherently, they result in depolarization. Thus the system can then be described as a combination depolarizer $\mathbf{M}_\Delta$ with form given in Eq. (2.7) and retarder of form given in Eq. (2.4) which is described by its general eigen vector $\hat{R}$ and phase shift Γ_R.

$$\mathbf{M}_{RX} = \mathbf{M}_\Delta(d_1, d_2, d_3)\mathbf{M}_R(\hat{R}, \Gamma_R) \tag{5.69}$$

The arguments of the depolarization matrix d_1, d_2, d_3 are the depolarization terms for each Stokes vector component. Thus, the amount of depolarization imposed by the receiver may be polarization dependent.

By evaluating the Mueller matrices in Eq. (2.11) we find the received intensities of each channel can be written

$$\begin{aligned} N_\parallel(z) &= \tfrac{N_0(z)}{2}\left[1 + \epsilon(\hat{R}, \Gamma_R, P_{TX}, \alpha, d_1, d_2, d_3)\,(1 - d_a(z))\right] \\ N_\perp(z) &= \tfrac{N_0(z)}{2}\left[1 - \epsilon(\hat{R}, \Gamma_R, P_{TX}, \alpha, d_1, d_2, d_3)\,(1 - d_a(z))\right] \end{aligned} \tag{5.70}$$

where $N_0(z)$ is the total received backscattered intensity from altitude z and $\epsilon(\hat{R}, \Gamma_R, P_{TX}\alpha, d_1, d_2, d_3)$ is a single term accounting for all cross talk components discussed above except depolarization from atmospheric scattering, which has been separated out for analysis. For simplicity, the arguments of $\epsilon(\hat{R}, \Gamma_R, P_{TX}, \alpha, d_1, d_2, d_3)$ will be dropped in all subsequent reference to the term.

The measured depolarization can then be written using Eq. (5.64) and (5.70) and rearranged to solve for ϵ.

$$\epsilon = \frac{1 - d_M(z)}{1 - d_a(z)} \tag{5.71}$$

Here $d_M(z)$ is the depolarization directly calculated from Eq. (5.64), $d_a(z)$ is the total depolarization from atmospheric scattering and z is the altitude under analysis. Note that ϵ is not altitude dependent as it accounts only for system effects.

The coupling effects induced by the receiver may be determined through use of a calibration altitude where d_a is well known. A calibration altitude is chosen where we assume the scattering is entirely due to Rayleigh scatter, and thus have a known depolarization ($d = 0.00727$ on the central Cabannes line at 532 nm[11]). We solve for ϵ using Eq. (5.71).

We then rewrite Eq. (5.71) as shown below.

$$d_a(z) = 1 - \frac{1 - d_M(z)}{\epsilon} \tag{5.72}$$

Thus d_a may be determined directly from the received perpendicular and parallel polarization intensity data by using a calibration altitude to solve for ϵ.

Note that molecular depolarization used for calibration is dependent on the transmitted wavelength and bandwidth of the receiver. If rotational Raman lines are passed in the receiver, they will not only change the depolarization but also cause it to have some temperature dependence[9].

This software algorithm proves to be an effective tool for removing polarization system effects while still preserving atmospheric information. The depolarization data shown in Figure 5.7 is taken from a lidar with significant retarding and depolarizing effects. The depolarization is shown for a fixed altitude as a function of time. As time progresses, the polarization plane of operation is rotated, thus giving the $\cos^2\theta$ shape to the depolarization estimate. Near the end of the dataset, an ice cloud comes into view, resulting in depolarization. The software algorithm described here removes the system effects, but preserves the atmospheric depolarization data. By comparison, the commonly employed calibration constants method [10] appears to remove system effects, but because it improperly describes system polarization effects, the atmospheric cloud depolarization is significantly skewed.

An error analysis of the above algorithm was performed using propagation of error. The result of this error analysis is shown below. The uncertainty, $\sigma_{d_a}(z)$, in estimation of $d_a(z)$ is given

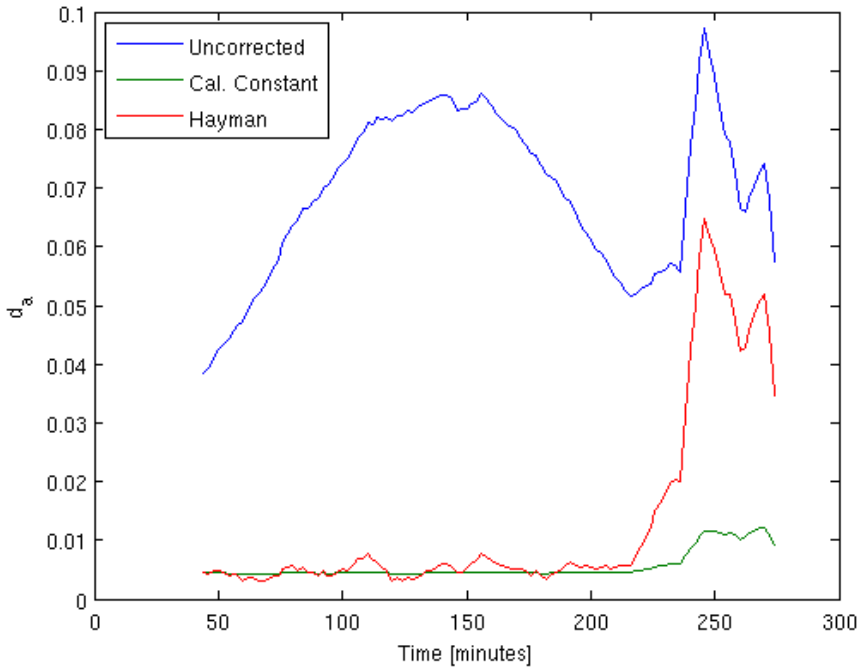

Figure 5.7: Estimated depolarization at a fixed altitude as a function of time by a lidar with substantial polarization effects using no software correction (blue), the software correction described here [32] (red) and calibration constants [10]. As time progresses the polarization plane of operation rotates, resulting in differing polarization effects. At the end of the data set a depolarizing ice cloud is present.

by

$$\begin{aligned}\sigma_{d_a}(z)^2 =& \frac{4\left(d_a(z_c)-1\right)^2}{\left(N_{\parallel}(z)+I\perp(z)\right)^2\left(N_{\parallel}(z_c)-I\perp(z_c)\right)^2} \\ &\times\left[\left(\sigma_{\perp}(z)^2N_{\parallel}(z)^2+\sigma_{\parallel}(z)^2N_{\perp}(z)^2\right)\left(\frac{N_{\parallel}(z_c)+N_{\perp}(z_c)}{N_{\parallel}(z)+N_{\perp}(z)}\right)^2\right. \\ &\left.+\left(\sigma_{\perp}(z_c)^2N_{\parallel}(z_c)^2+\sigma_{\parallel}(z_c)^2N_{\perp}(z_c)^2\right)\left(\frac{N_{\parallel}(z)-N_{\perp}(z)}{N_{\parallel}(z_c)-N_{\perp}(z_c)}\right)^2\right],\end{aligned} \tag{5.73}$$

where the term σ_{d_a} is the standard deviation of the derived depolarization from atmospheric scattering, z_c is the calibration altitude used to solve for ϵ, $\sigma_{\perp}(z)$ and $\sigma_{\parallel}(z)$ are the standard deviations of the respective polarization photon count measurements. Here uncertainty in the detected signals is assumed to be the result of shot noise obeying Poisson statistics, where each polarization channel

is uncorrelated.

5.4 Instrument Error in Diattenuation

The two diattenuation measurement techniques proposed in Chapter 4 provided different phase matrix measurement capabilities. Likewise, they each have different error susceptibilities to instrument effects, which we will cover here.

5.4.1 Parallel-45-Perpendicular

I developed and proposed the P45P technique for identifying oriented scatterers in Chapter 4 by resolving a non-zero diattenuation in the scattering matrix. Thus, of particular concern in this technique are polarization effects that may result in false positive identification of oriented ice crystals.

Here we analyze the impact on P45P for each independent polarization effect. When these effects compound in the receiver, the analytical expressions become intricate and complicated. At this point, simulations are run numerically to determine the system sensitivities.

To consider the effects of retardance on diattenuation measurements using P45P, let the receiver have the general form of a retarding Mueller matrix so that its eigen polarization is given by the following vector in Poincaré space

$$\hat{R}_{RX} = \begin{bmatrix} R_1 \\ R_2 \\ R_3 \end{bmatrix}. \tag{5.74}$$

where

$$R_1^2 + R_2^2 + R_3^2 = 1. \tag{5.75}$$

The retarder imposes a phase shift Γ_{RX} on the received light resulting in a rotation by the corresponding angle around $\hat{R}_{RX}$ in Poincaré space. Because we are concerned with false positives in identifying oriented scatterers, we let the scattering matrix represent randomly oriented scatterers

as given in Eq. (3.5). The measured diattenuation is then given by Eq. (4.17). When we evaluate the SVLE for this measurement technique with retarding effects in the receiver we obtain

$$D_q = (1-d)\left[R_1 R_2 \left(\cos\Gamma_{RX} - 1\right) - R_3 \sin\Gamma_{RX}\right]. \tag{5.76}$$

Thus retarding effects in the receiver can cause diattenuation measurements to shift off zero. If the entire profile shifts uniformly due to system polarization effects, it is unlikely to result in a false positive in identifying oriented scatterers. However, the dependence on atmospheric depolarization in Eq. (5.76) means that highly depolarizing scatterers would deviate from the overall shift in the profile. Thus retarding effects in the receiver can seriously impact confidence in the P45P measurement and it is important that these effects are avoided for the purpose of identifying oriented scatterers.

To analyze the effects of depolarization on P45P we allow the receiver depolarization to be polarization dependent, its matrix has the form

$$\mathbf{M_{\Delta RX}} = \begin{bmatrix} 1 & 0 & 0 & 0 \\ 0 & 1-d_{RX_1} & 0 & 0 \\ 0 & 0 & 1-d_{RX_2} & 0 \\ 0 & 0 & 0 & 1-d_{RX_3} \end{bmatrix}, \tag{5.77}$$

where d_{RX_1}, d_{RX_2}, and d_{RX_3} are the receiver depolarizations for horizontal/vertical, $\pm 45°$ and circular polarizations respectively. Independent of any other effects in the receiver and assuming the scatterer consists of randomly oriented particles, the measured diattenuation evaluates to zero. If we then allow the scattering matrix to assume the form of oriented scatterers given in Eq. (3.21), we see the receiver depolarization scales linear diattenuation measurements

$$D_q = \frac{(1-d_{RX_1})f_{12}}{f_{11}}. \tag{5.78}$$

Thus, if the depolarization of the receiver is already known, a correction can be applied to D_q to reduce its effect. More importantly, the presence of depolarization in the receiver will not result in false positives for oriented scatterers, because when scatterer diattenuation is zero, D_q remains zero independent of depolarization.

Now let the receiver exhibit diattenuation described by its diattenuation vector and Eq. (2.2)

$$\vec{D}_{RX} = \begin{bmatrix} D_1 \\ D_2 \\ D_3 \end{bmatrix}, \tag{5.79}$$

where the magnitude of diattenuation is given by

$$|\vec{D}_{RX}| = \sqrt{D_1^2 + D_2^2 + D_3^2}. \tag{5.80}$$

We can then evaluate the SVLE for P45P assuming the scattering medium consists of randomly oriented particles and obtain the measured diattenuation

$$D_q = D_1 \frac{D_2 \left(1 - \sqrt{1 - |\vec{D}_{RX}|^2}\right)(1-d) - |\vec{D}_{RX}|}{[1 - D_2(1-d)]\,|\vec{D}_{RX}|}. \tag{5.81}$$

It is not surprising that diattenuation in the receiver can result in false positives in detection of oriented scatterers. The overall effect will be a shift in the mean diattenuation profile. It is unlikely that this would be interpreted as a diattenuation signature. However, the dependence on depolarization in Eq. (5.81) means that depolarizing effects can cause the measured diattenuation to shift off the mean. As a result, depolarizating clouds could appear to be diattenuating due to their deviation from the profile mean. Thus, false positive detection of oriented scatterers could occur if substantial diattenuation exists in the receiver.

5.4.1.1 P45P Simulation of System Effects

While larger integration times, higher laser power and larger receiver apertures can be used to reduce shot noise, polarization effects in the lidar system dictate a fixed baseline in the instrument's polarization resolution. In Figures 4.4 and 4.5, even very high densities and concentrations of oriented scatterers are expected to produce diattenuation values of less than 0.3. Thus it is important that system error in this measurement ΔD_q is reduced well below this limit.

Consider a receiver with depolarization $d_{RX_1} = d_{RX_2} = d_{RX_3} = 0.05$ and diattenuation is linear with $|\vec{D}_{RX}| < 0.001$. These polarization effects in the receiver are evaluated using the

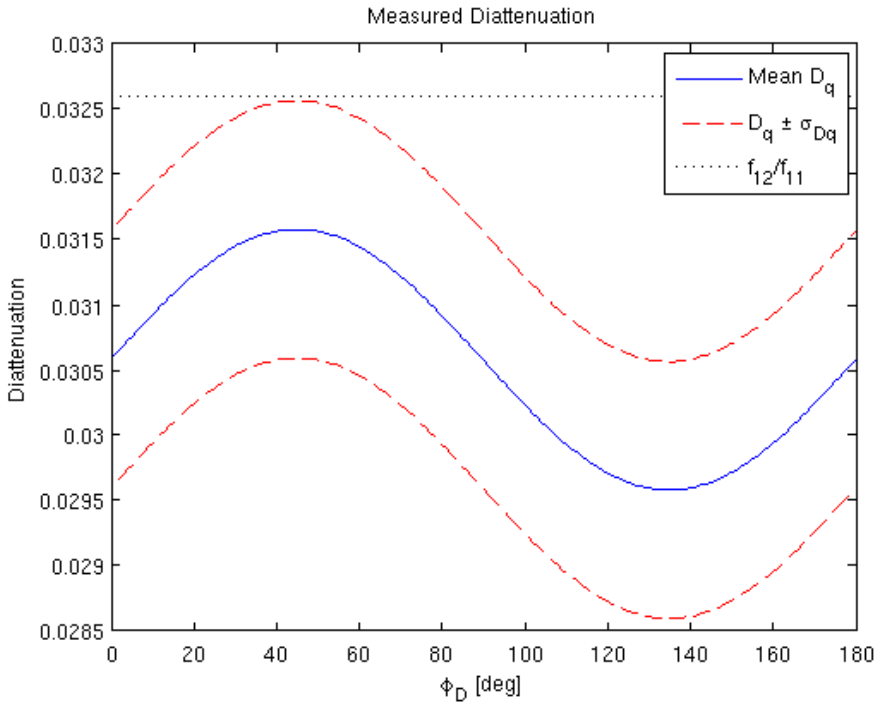

Figure 5.8: Simulated diattenuation measurement of cirrus cloud at an altitude of 10 km as a function of linear diattenuation angle in the receiver. Diattenuation uncertainty due to shot noise is contained between the red (dashed) lines and the black (dotted) line is the actual linear diattenuation of the scatterer. The receiver is assumed to demonstrate a depolarization of 0.05 and linear diattenuation of 0.001.

SVLE during interrogation of a cirrus cloud with $p_o = 0.12$ and $R_{BS} = 50$ at an optimal lidar tilt angle of 12°. The resulting measured diattenuation is plotted in Figure 5.8 as a function of linear diattenuation angle $\phi_D = \arctan\left(\frac{D_2}{D_1}\right)$. We also perform shot noise error calculations assuming the lidar has a telescope diameter of 35 cm, 20% instrument efficiency, 80 mW laser and 2 minute integration per polarization channel. The scatterers under interrogation are at an altitude of 10 km.

The results in the Figure 5.8 show the combination of depolarizing and diattenuating effects result in an instrument error of approximately $\Delta D_q = 0.003$ when the diattenuation of the scattering medium is near 0.03. Clearly if the angle ϕ_D is known, the known error may be less than 0.003.

Instrument effects can skew P45P diattenuation measurement accuracy in a variety of ways. As these polarization effects compound they become more complicated. Also the error introduced by

the instrument is generally a function of the scattering matrix under interrogation. This highlights the importance of understanding a full polarization design and analysis through the SVLE as polarization lidar becomes more advanced.

5.4.2 Alternating Cross Polarized

While P45P is sensitive to polarization effects in the receiver, ACP offers a more attractive alternative for lidar systems with retardance and depolarizing effects in the receiver. Rather than perform polarization analysis of the received light, ACP only detects the polarization dependence of the volume backscatter coefficient, which does not require a polarizer in the receiver.

If the lidar receiver demonstrates substantial retardance and depolarization but negligible diattenuation the Mueller matrix of the total optical path is given by

$$\mathbf{M}_{path} = \mathbf{M}_{\Delta}\mathbf{M}_{R}\mathbf{F}(\vec{k}_i, \vec{k}_s), \tag{5.82}$$

where $\mathbf{M}_{path}$ is the total Mueller matrix observed by the transmit light, $\mathbf{M}_{\Delta}$ is the depolarizing term of the receiver system, $\mathbf{M}_{R}$ is the retarding term of the receiver system, and $\mathbf{F}(\vec{k}_i, \vec{k}_s)$ is the scattering phase matrix which exhibits a combination of polarization effects including diattenuation and is described by Eq. (3.21). We assume the outgoing polarization is known to be linear. The phase matrix has the block description

$$\mathbf{F}(\vec{k}_i, \vec{k}_s) = \begin{bmatrix} 1 & \vec{D}_{sca}^{T} \\ \vec{P}_{sca} & \mathbf{m}_{sca} \end{bmatrix}, \tag{5.83}$$

where $\vec{P}$ is the polarizance, $\vec{D}$ is the diattenuation, $\mathbf{m}$ is an arbitrary 3x3 matrix and the subscript *sca* indicates the block element is solely a component of the scattering phase matrix. If we evaluate after substituting Eq. (5.83) into Eq. (5.82) the total path Mueller matrix has the form

$$\mathbf{M}_{path} = \begin{bmatrix} 1 & \vec{D}_{sca}^{T} \\ \vec{P} & \mathbf{m} \end{bmatrix}. \tag{5.84}$$

Both $\vec{P}$ and $\mathbf{m}$ have been contaminated by effects of the receiver optical system and drop the *sca* subscript, but because $\mathbf{F}(\vec{k}_i, \vec{k}_s)$ is the only matrix exhibiting diattenuation, $\vec{D}_{sca}$ is the original

diattenuation vector of the scattering phase matrix. Thus direct measurement of diattenuating terms can be done without system error contribution regardless of the magnitude of depolarization or retardance in the receiver.

ACP is still sensitive to diattenuating effects in the receiver. If we assume the receiver diattenuation is the general form given by the diattenuation vector in Eq. (5.79), the measured diattenuation calculated using Eq. (4.30) is given

$$D_{ACP} = \frac{f_{12} + D_1 f_{22}}{f_{11} + D_1 f_{12}}. \tag{5.85}$$

Thus ACP is only sensitive to the receiver diattenuation component along the transmitted polarizations.

The advantage of measuring diattenuation with ACP lies in its insensitivity to retarding and depolarizing effects in the receiver. Additionally, the two measured signals have identical intensities for randomly oriented scatterers, so this technique is less likely to produce false positives of oriented scatterers due to detector nonlinearity.

5.5 Instrument Error in Non-Polarization Lidar

The presence of diattenuation is a problem for lidar systems even when they do not measure polarization. Because diattenuation is polarization dependent system efficiency, different backscattered signals will experience different system attenuation depending on the scatterer's polarization properties.

Consider an instance where all atmospheric scatterers are randomly oriented and axially symmetric so their phase matrices take the form in (3.5). For a common backscatter lidar, there is no polarizer, so the projection matrix $\mathbf{O}$ simply becomes

$$\mathbf{O} = \begin{bmatrix} \eta & 0 & 0 & 0 \end{bmatrix} \tag{5.86}$$

where η is the detector efficiency. Assume the receiver exhibits diattenuating effects so that the

diattenuation vector is

$$\vec{D}_{RX} = |D_{RX}| \begin{bmatrix} \cos 2\phi_D \cos \Gamma_D \\ \sin 2\phi_D \cos \Gamma_D \\ \sin \Gamma_D \end{bmatrix}, \tag{5.87}$$

where the angle ϕ_D is the linear rotation angle of the diattenuation vector and Γ_D is twice the vector's ellipticity angle. For linear diattenuation vectors, Γ_D is zero or π and for circular diattenuation, $\Gamma_D = \pm\frac{\pi}{2}$.

The primary data product of backscatter lidar is the backscatter ratio. This is a useful quantity because it avoids the necessity to measure absolute return signals. Instead, the total return signal is normalized to the generally stable molecular return. The backscatter ratio is defined in Eq. (1.4) where it may be regarded as the ratio of the total signal counts to only the counts attributable to molecular scatterers.

If we evaluate the SVLE for the above scenario, allowing that the total depolarization of the medium d_T is generally different than the depolarization of the molecular scatterers d_m, the backscatter ratio, using Eq.(1.4) is measured

$$R_{BS}^{M} = \frac{1 + (1 - d_T)D_{\|}}{1 + (1 - d_m)D_{\|}} \frac{\beta^{tot}}{\beta^{mol}}, \tag{5.88}$$

where $D_{\|}$ is the diattenuation of the receiver along the transmit polarization. The measured backscatter ratio clearly has an error factor that is dependent on the depolarization of the medium under investigation.

This issue has been investigated by [43] using conventional polarization lidar theory, where it was concluded that folding mirrors and beamsplitters required polarization coatings to make the backscatter measurements polarization independent. However, we consider here a more affordable solution. For a transmitted polarization given in Eq. (4.12), the diattenuation term in Eq. (5.88) is given as

$$D_{\|} = |D_{RX}| \cos(2\phi_D - 2\phi_f) \cos(\Gamma_D - \Gamma_f). \tag{5.89}$$

If we linearly rotate the outgoing polarization so that $2\phi_D - 2\phi_f = \frac{\pi}{2}$ (S_{TX} is perpendicular to

the linear diattenuation component in the equatorial plane in the Poincaré Sphere), $D_{\|}$ becomes zero and $R_{BS}^{M} = R_{BS}$. Thus, the use of a half wave plate negates the need for costly polarization coatings on the lidar system optical components.

This example demonstrates the importance of considering polarization effects in lidar even when the lidar does not measure polarization. It also demonstrates how simple solutions are easily missed when using the incomplete polarization theory common to conventional polarization lidar analysis.

Chapter 6

Arctic Lidar Technology Facility

The Arctic Lidar Technology Facility (ARCLITE) lidar located in Kangerlussuaq, Greenland ($67.0°N, 309.1°E$) consists of two transmitting lasers at 532 nm. The receiver detects at three different wavelengths, but for this work, we will only address the 532 nm receiver channel.

The transmitter layout is shown in Figure 6.1 where the SpectraPhysics Laser (560 mJ/pulse at 30 Hz) is used for high altitude studies (25-90 km) and the BigSky lasers (50 mJ/pulse 15 Hz on each of the two orthogonal polarization modes) transmit alternating horizontal and vertical polarizations for study of the troposphere and stratosphere (0-35 km). The SpectraPhysics transmit path contains a motorized HWP to incrementally rotate the outgoing laser polarization, and alternatingly flip the polarization by 90° every minute. A polarization compensator consisting of two QWPs, as described in Section 5.2, immediately follows the HWP to cancel retarding effects in the SpectraPhysics transmitter path. A 5x Beam expander is used to achieve lower than 0.1 mrad divergence in the beam.

The BigSky lasers have a fixed HWP to set the outgoing linear polarization angles of the alternating cross polarized output. Immediately following the HWP is the compensator for this outgoing channel, then a 5x beam expander to reduce beam divergence. A neutral density filter wheel is inserted into the transmit path. Even at their lower powers, attenuation of the BigSky laser is often required to avoid detector nonlinearity from low altitude returns (below 10 km). A multimode optical fiber follows the last folding mirror in the BigSky path. Some residual optical power leaks through this mirror and is coupled into the fiber. The fiber is then fed into the receiver

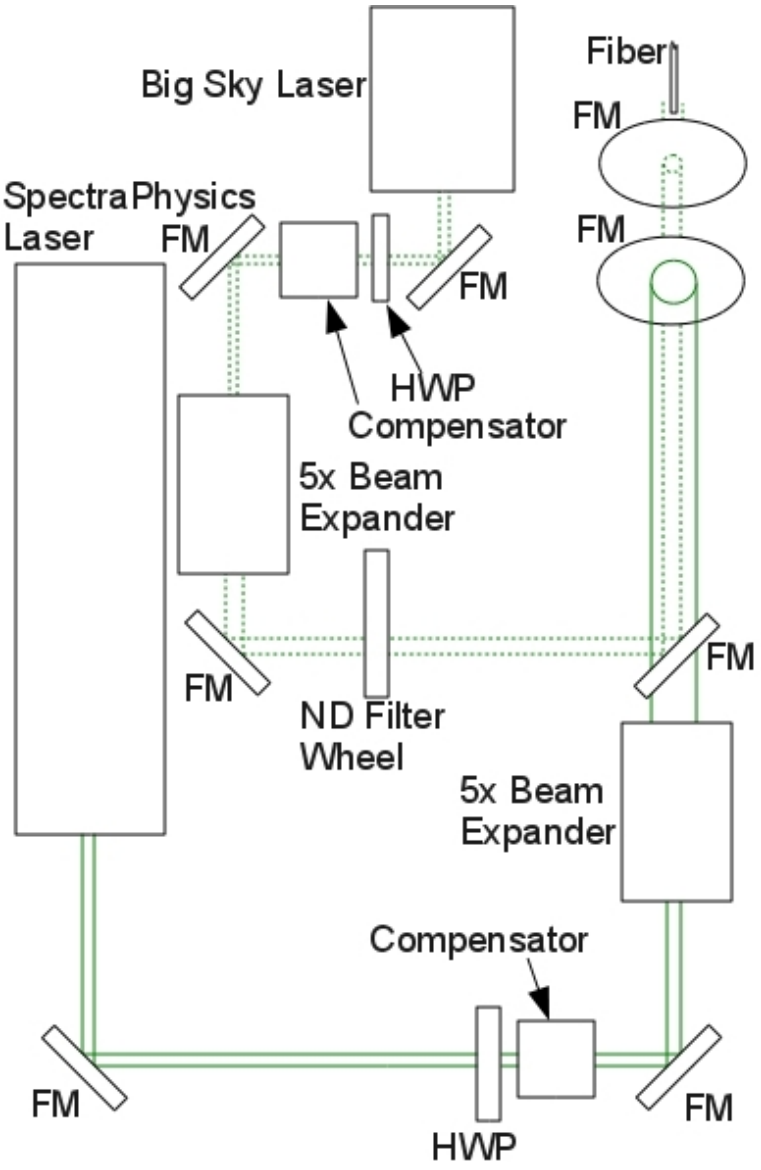

Figure 6.1: ARCLITE transmitter with the high powered SpectraPhysics laser (solid) and lower power cross polarized BigSky lasers (dashed). FM stands for folding mirror.

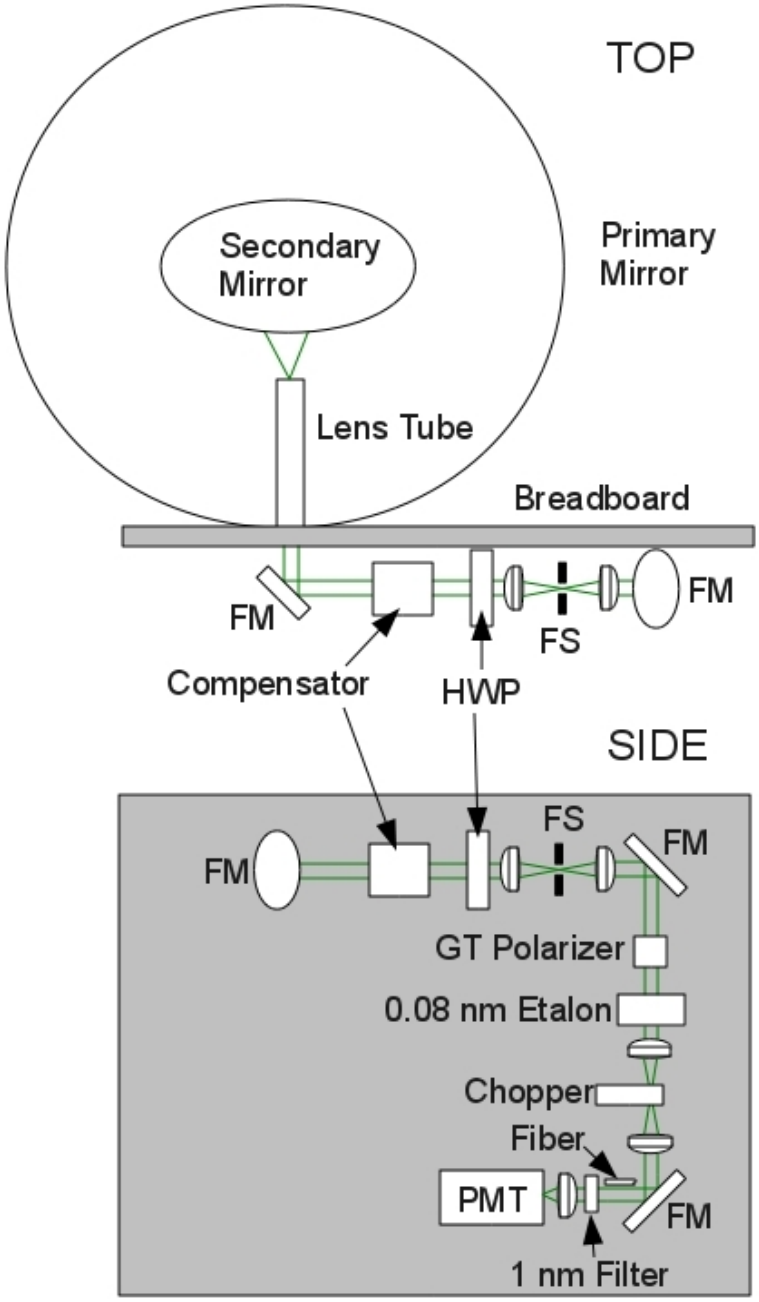

Figure 6.2: ARCLITE receiver with an 92 cm aperture Newtonian telescope filtering and polarization optics. FM stands for folding mirror and FS stands for field stop.

PMT to provide a time zero pulse for the BigSky lasers and a measure of relative transmit power between the two polarizations. This relative transmit power is then used as a correction factor when calculating polarization effects.

The receiver layout is shown in Figure 6.2 where all backscattered light is collected by a 92 cm aperture Newtonian telescope. This light is coupled into a lens tube to bring the light onto on optical breadboard. The receiver has a polarization compensator for canceling retarding effects and a motorized HWP for incrementally changing the received polarization. After a field stop, used to reduce solar background, the light is passed through a fixed Glan-Thompson polarizer. The light is then filtered through a Daystar 0.08 nm solid mica etalon (used only during daytime conditions to reduce solar background). A chopper is in place to block low altitude returns from the SpectraPhysics laser. These low altitude signals are strong enough to cause signal induced noise (afterpulsing) on the photomultiplier tube (PMT) if they are not blocked. The signal is finally passed through a 532 nm interference filter with a 0.5 nm bandwidth before being focused onto the PMT cathode. The fiber collecting leaked optical power from the BigSky laser in the transmitter is also fed near the PMT. Fiber alignment is not particularly important here. It is sufficiently misaligned so the signal on the PMT is within the linear dynamic range of the detector.

ARCLITE uses a single polarization detection channel with two possible transmit polarizations. The receiver motorized half wave plate is aligned for maximum rejection of partially polarized solar background by the Glan-Thompson polarizer. In the SpectraPhysics transmitter, the outgoing polarization plane is then aligned for maximum transmission through the receiver polarizer. This produces the parallel polarization measurement used in conventional polarization lidar. On the next dataset, the outgoing polarization is rotated by 90° by the motorized HWP in the transmitter for minimum transmission through the receiver polarizer, thus providing the perpendicular polarization measurement. Every minute the transmit half wave plate rotates the polarization by 90° to produce a sequence of parallel and perpendicular measurements. Although the perpendicular plane will be extinguished by the receiver Glan-Thompson, half of the depolarized signal will pass through with minimal background. Thus this method provides a measure of $N_{\perp}$ and $N_{||}$ (see Figure 6.3) and is equivalent to the two receiver channel method when $\mathbf{F}$ is diagonalized. This method provides an estimate of d with minimal solar background contamination in both polarization measurements. This polarization technique has achieved an improvement in the signal-to-noise ratio (SNR) by as

much as a factor of five during summer operations and has been in use for many years at the site [84].

As measurements are made throughout the day, the polarization plane of the receiver is adjusted by its rotating half-wave plate to track the sun and maintain rejection of the linearly polarized solar background component by the Glan-Thompson polarizer. The SpectraPhysics transmitted polarization also uses a rotating half-wave plate to maintain optimal transmission through the receiver. Consequently, when in sun tracking mode to reject polarized background, the system optics experience all planes of linear polarization throughout the course of the day. The need to use all linear polarizations result in variable polarization effects throughout the lidar run. Significant retardance and depolarization impact the instrument's ability to estimate depolarization.

The BigSky transmitter operates similar to the SpectraPhysics, but instead of using a motorized HWP, the laser pulses are alternated between two orthogonal polarizations. The outgoing polarizations can be rotated together by a fixed angle using the HWP at the laser output. However, this HWP is not motorized, so it does not track the receiver polarization plane in sun tracking mode. Though the BigSky polarization planes may not align to the receiver during daytime operation, software correction still allows depolarization estimates for BigSky laser returns [32].

6.1 Characterization and Mitigation of ARCLITE Polarization Effects

To characterize the ARCLITE receiver, the transmitter must first be compensated. Accurate knowledge of the outgoing polarization is essential to properly characterize the receiver during lidar operation. The transmitter exhibited relatively low polarization effects with no detected diattenuation or depolarization, and linear retardance of approximately 0.10 radians (the output for a linearly polarized input has a maximum S_3 circular Stokes term of 0.10). The transmitter layout for the high altitude SpectraPhysics Laser has two folding mirrors. The first mirror folds the beam path in the horizontal plane, while the second folds the beam vertically, out of the horizontal plane. Less some small misalignment, the s-polarization of one mirror becomes the p-polarization on the second, and any phase shift or diattenuating effect is applied equally to both modes. The residual

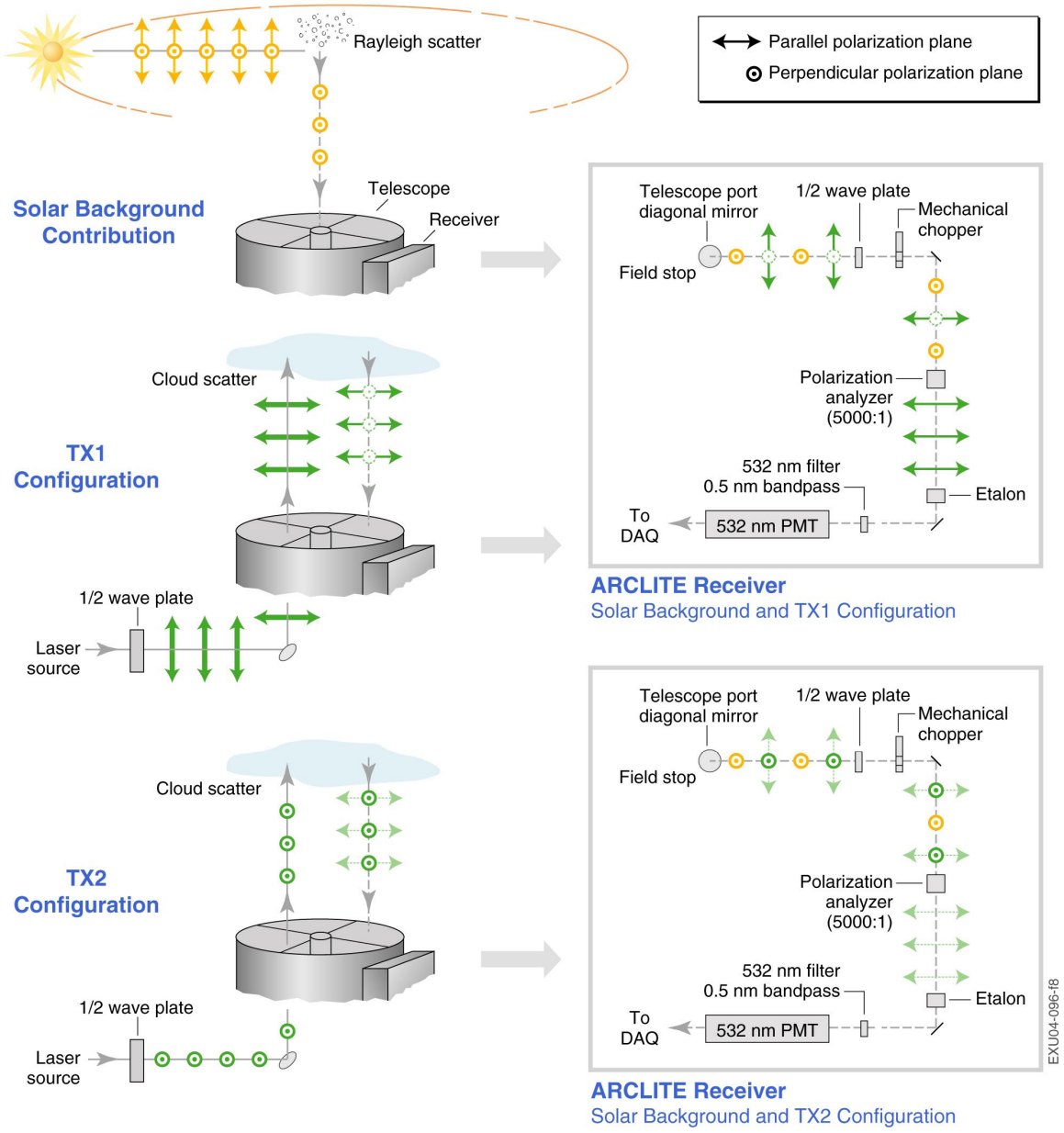

Figure 6.3: Polarization operation of ARCLITE. The half wave plate in the receiver is aligned to minimize solar background. The transmitter half wave plate is then aligned to the receiver polarization plane for parallel measurements, and orthogonal to the receiver for perpendicular measurements [33].

difference in phase between the two modes was eliminated using the compensator optimization technique described in Chapter 5.

The receiver in the ARCLITE system was then characterized according to the method described in Eq. (5.7) in Chapter 5. The half wave plate (HWP) in the transmitter is used to rotate the outgoing linear polarization to achieve horizontal, vertical and 45° polarizations. A quarter wave plate (QWP) is also added to the transmitter to obtain the required circular polarization. In the receiver, the fixed analyzer is removed from the system and a rotating analyzer is inserted prior to the motorized HWP, where the compensator will be installed. Also there is room to insert a QWP before the polarizer to measure the circular S_3 Stokes term. After the analyzer, retarding and depolarizing effects are not a concern. However, diattenuation will impact the efficiency of the different measured polarizations. The folding dichroic filter exhibits some diattenuation and its polarization preference is thus accounted for when measuring horizontal and vertical polarizations.

The polarization matrix of ARCLITE is then determined by measuring two profiles for each Stokes term, using altitudes above 25 km to avoid depolarizing aerosol contamination. The measured matrix for the ARCLITE receiver is within $-11.7dB$ of a realizable Mueller matrix. The normalized Cloude filtered receiver Mueller matrix is

$$\mathbf{M}_{RX} = \begin{bmatrix} 1 & -0.004 & -0.013 & -0.013 \\ -0.075 & 0.850 & -0.024 & 0.026 \\ -0.013 & 0.007 & -0.377 & 0.808 \\ -0.022 & 0.044 & -0.695 & -0.311 \end{bmatrix}, \tag{6.1}$$

and the error of each matrix term is dominated by shot noise and given as

$$\sigma_{Mrx} = \begin{bmatrix} 0.009 & 0.009 & 0.023 & 0.017 \\ 0.01 & 0.01 & 0.024 & 0.017 \\ 0.009 & 0.009 & 0.023 & 0.017 \\ 0.009 & 0.009 & 0.022 & 0.014 \end{bmatrix}. \tag{6.2}$$

In Eq. (6.1) and (6.2) we see the values in the top row are less than their corresponding uncertainty. Thus ARCLITE has low diattenuation that is not resolvable in this experiment. The

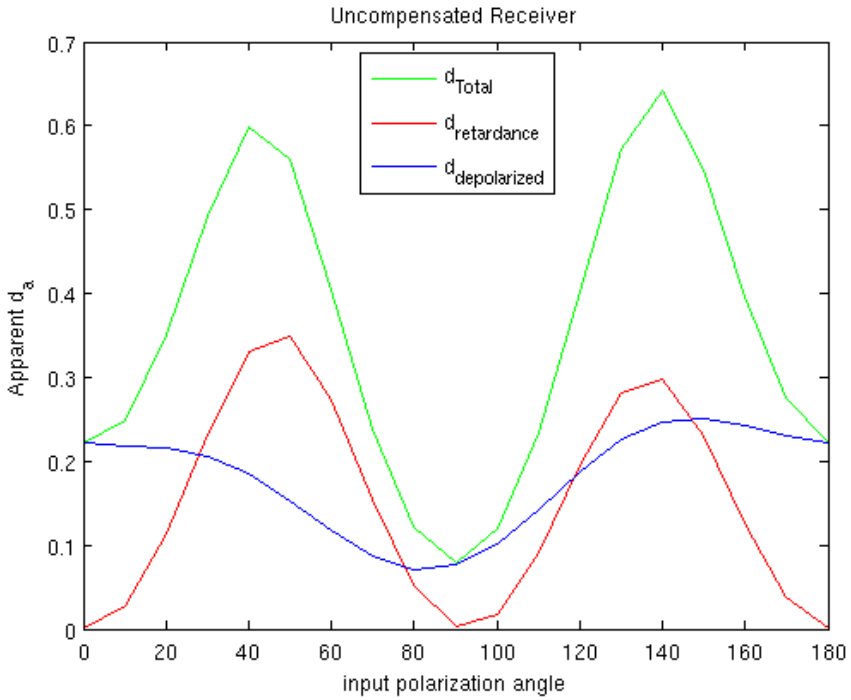

Figure 6.4: Apparent depolarization resulting from ARCLITE receiver system based on the Mueller matrix measured in operation shown in Eq. (6.1) (green). The effects are decomposed into those attributed to depolarization (blue) which is not correctable in hardware and retardance (red) which is correctable.

receiver matrix is then decomposed to determine the relative contributions to error in polarization measurements contributed by the depolarizing and retarding terms [42]. The error here is termed apparent depolarization. This is the measured depolarization due to system effects when the scattering medium is polarization preserving. The total and individual contributions of retarding and depolarizing terms to apparent depolarization are plotted as a function of linear input polarization angle in Figure 6.4. Retarding contributions to apparent depolarization can be canceled through installation of a compensator consisting of two QWP that impose an equal and opposite phase shift to that of the receiver system. However, depolarization cannot be canceled with hardware solutions. After installation of the compensator, the apparent depolarization of the system should track that contribution of the depolarizing matrix in the receiver.

Based on the decomposition of the receiver matrix, the angular positions of the QWPs in

the receiver can be determined to cancel the system retarding effects. In practice however, we use the optimization technique described in Chapter 5. The apparent depolarization of the system is estimated before and after installation of the compensator using signals from an altitude of strictly molecular scatterers. The results are shown in Figure 6.5. The apparent depolarization is a good qualitative fit to that predicted by the system Mueller matrix. However, we notice that the maximum in apparent depolarization without compensation is less than that predicted by the matrix simulation.

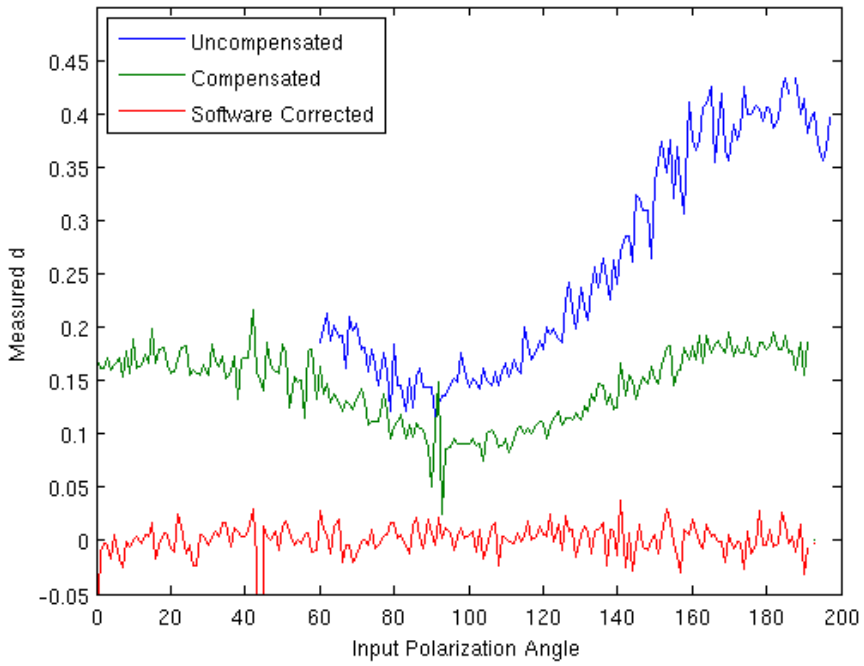

Figure 6.5: Apparent depolarization resulting from ARCLITE receiver system as measured in operation for an uncompensated receiver (blue), compensated receiver (green) and software corrected (red) [33].

In addition to reducing signal cross talk, the compensator in the receiver also improves polarized solar background rejection. Retarding effects cause linearly polarized solar background to be elliptical. Though the receiver HWP is aligned for maximum rejection of the background, it cannot fully reject the now elliptically polarized light. The compensator ensures that the linearly polarized light remains linearly polarized, and thus ARCLITE experiences lower background levels

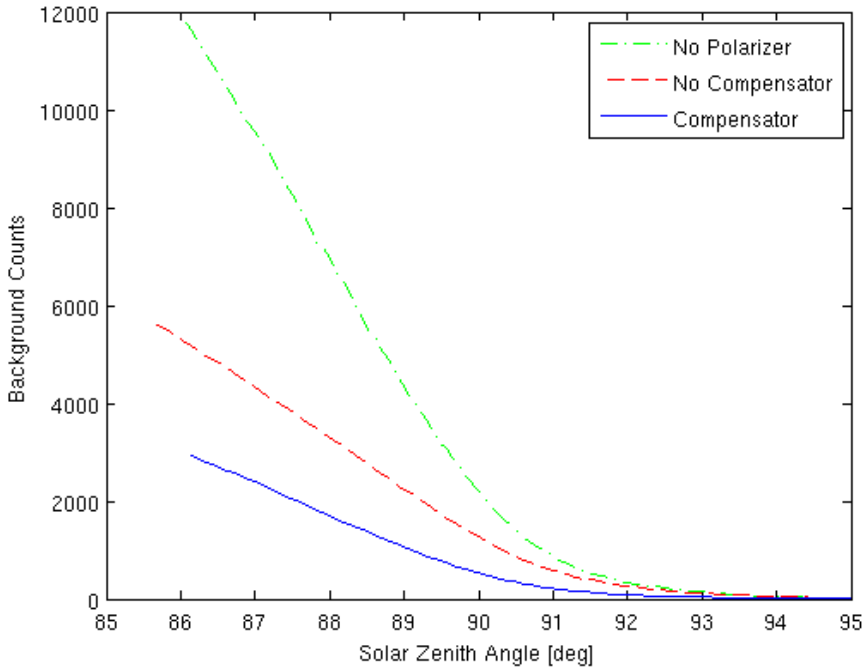

Figure 6.6: Solar background counts experienced by ARCLITE as a function of solar zenith angle (SZA) with no polarizer (green), with a polarizer (red) and with compensation and polarizer (blue). As SZA approaches 90°, the solar background from Rayleigh scattering increases in DOP, allowing better background rejection through polarization [33].

during daytime operation (see Figure 6.6).

After hardware compensation is implemented in ARCLITE, the remaining system effect is depolarization. If this system contribution is not reduced it will directly bias depolarization estimates. The software correction discussed in Chapter 5 [32] is applied to the recorded data to remove receiver system depolarization, residual receiver retardance, partial polarization of the transmit laser, and misalignment of the transmitter and receiver polarization planes. The Rayleigh backscatter signal at 35 km is used to determine the system bias error, ϵ. This software correction is applied to the compensated depolarization data in Figure 6.5. The combination of hardware and software compensation approaches the expected limit of Rayleigh depolarization allowing the ARCLITE lidar to make polarization measurements of aerosols and clouds from troposphere to the mesopause (80 km).

6.2 Polar Mesospheric Cloud Particle Shape

Polar mesospheric clouds (PMCs), also called noctilucent clouds (NLCs), are high altitude ice particles that form over the polar regions in the mesopause at a centroid altitude of 83 km. During the summer months, adiabatic cooling causes the mesopause to cool sufficiently for water to condense and freeze at these high altitudes[34], resulting in formation of these clouds.

PMCs have a strong influence on the mesopause environment by redistributing trace gases[90]. Depletion of mesosphere/lower thermosphere (MLT) metals has been observed in the presence of PMCs[59] and the reaction rates of this heterogeneous chemistry are driven by the surface area of the particles present[61].

Many properties of the PMCs have been established. They are made up of condensed water vapor[34]. Study of scattering brightness has established a volume equivalent standard radius of 50 nm for PMC particle sizes[85, 67, 89]. Probes into the particles sizes have are found to be relatively insensitive to variations in the asphericity of the particles[8] allowing the problem of particle shape and size to be decoupled.

Owing to the sub-micron size of PMC particles and the visible wavelengths used to probe them, Mie-Rayleigh scattering theory has predominantly been applied. However, the common practice of using Mie theory to analyze light scattered by PMCs makes the unfounded assumption that the particles are spherical. This has far-reaching implications for the interpretation of observations and modeling of the growth-sedimentation-sublimation aspects of PMCs. A non-spherical particle has a greater surface area-to-volume (mass) ratio than a spherical particle of the same linear dimension. In [64] it is suggested the settling speed of a mesospheric cloud particle will depend on its shape as well as its size. Slower falling non-spherical particles would experience more time in the region of supersaturation which may enhance its potential for growth. Also, the lesser volume of a non-spherical particle will require less water vapor to provide the same scattering cross-section as a spherical particle. This can have important implications on the growth of PMCs because the water vapor concentration in the mesosphere is limited to only a few parts per million. Recently, [63]

have demonstrated theoretically the utility of applying non-spherical PMC particles to improve the agreement between microphysical cloud models and space-based and ground-based observations. Furthermore, [23] has provided space-based spectral data suggesting PMC particles are not spherical. However, further observational evidence is needed to conclude whether the clouds are made of non-spherical particles.

Lidar observations can contribute to this work by observing the polarization effects of back scattered laser signals from PMCs. The ALOMAR RMR-Lidar has reported the only known depolarization measurement of a PMC occurrence [7] which suggests that PMC particles can be non-spherical. This measurement suggested needle like scatterers with axial ratios varying between 1/2 and 1/10. In addition to this discovery, it also became apparent that the structure of PMCs can vary both temporally and spatially. The peak in depolarization did not correspond to the peak in backscatter from the PMC suggesting that PMC particles change shape as they settle and eventually sublimate. PMC properties may vary depending on any number of conditions under which they are observed so the one depolarization observation is not sufficient to generalize PMC particle shape. Thus further, independent PMC depolarization measurements are needed. These lidar polarization measurements of PMCs enable a new view of PMC light scattering. However, it is expected that the depolarization will only be a few percent and will require sensitive measurements.

For polarization measurements of PMC backscatter, stringent requirements are placed on the lidar system to minimize any altering effects to the backscatter polarization. If polarization coupling in the lidar receiver is small compared to the expected depolarization by the scatterer, certain approximations may be applied to reduce contamination of polarization data due to system polarization effects [11, 1, 2]. However, the expected change in polarization due to PMC particles is only a few percent so system effects must be reduced to below 1% in order to give confidence in the estimated depolarization by PMC particles. This can be accomplished by applying sophisticated and expensive optical coatings on all reflective surfaces to preserve the incoming polarization - an approach used by the ALOMAR RMR-Lidar [Baumgarten, personal communication, 2010]. Here, the techniques from Chapter 5 are applied to ARCLITE and used to evaluate the instrument's

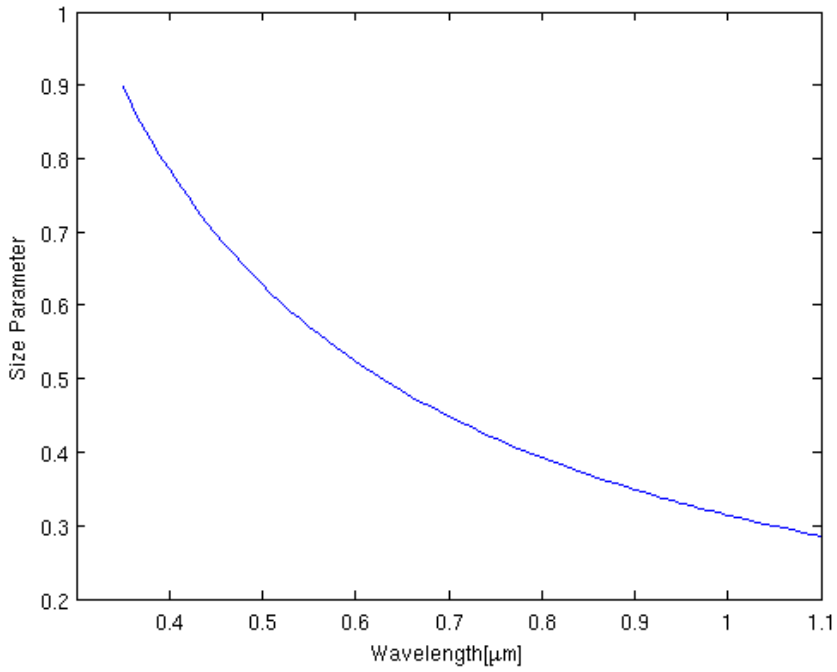

Figure 6.7: Size parameter of PMC particles with an average radius of 50 nm for incident wavelengths in the optical spectrum.

ability to study and estimate PMC depolarization.

The size parameter of a particle is defined

$$x = \frac{2\pi a}{\lambda} \tag{6.3}$$

where a is the particle radius and λ is the incident wavelength. For a PMC particle of average radius 50 nm[7] and optical wavelengths incident, this size parameter is on the edge of the Rayleigh/Mie region (see Figure 6.7). This means that backscatter is relatively weak compared to some aerosols and exhibits a frequency dependence.

Study of PMC depolarization is difficult due to the high altitude of the clouds and small particle size relative to optical wavelengths. Thus returns are often shot noise limited. These clouds only form during the summer months at high latitudes, so that solar background is constant and persistent. As a result, signal to noise becomes a critical component in lidar system design. Invariably, the designer must have definite numbers to trade possible expense with detection capability,

as well as performance of other optical components.

6.2.1 PMC Particle Simulation

The two parameters under analysis in this report are the depolarization d and the scattering cross section C_{sca} for PMCs. T-matrix FORTRAN code is publicly available on the web[1] which utilizes the theory described in [49, 52] to produce the orientationally averaged T-matrix, scattering cross section, and phase matrix of a rotationally symmetric randomly oriented scatterer [51].

The PMC particles are assumed to have an average radius of 50 nm. In the case of aspherical particles, this radius defines the size of an equivalent volume sphere. The scattering cross section of PMC particles is determined to be relatively invariant with asphericity when the particle is characterized in terms of volume equivalent spheres[6].

PMC particles are reported to be "needle like" and may be analyzed either as prolate finite cylinders or prolate spheroids with axial ratios in the range of 1/2-1/10 [7]. An axial ratio of 1/6 is chosen for this analysis. The particles are assumed to be randomly oriented due to the effects of Brownian motion [13]. The values for the index of refraction of ice are taken from [91].

Table 6.1: PMC Scattering Input Simulation Parameters

Volume Equivalent Radius	50 nm
Particle Geometry	Prolate Spheroid
Axial Ratio	1/6
Index of Refraction	see [91]
Incident Wavelength	350-1100 nm
Scattering Angle	π

The T-matrix code is run with the particle parameters described in Table 6.1 for incident wavelengths 350 nm to 1100 nm.

At optical wavelengths, PMC particles are on the edge of the Mie/Rayleigh boundary (see Figure 6.7). Thus it should come as little surprise that their scattering cross sections increase as the incident wavelength decreases (see Figure 6.8). We also find that depolarization increases with

[1] http://www.giss.nasa.gov/∼crmim

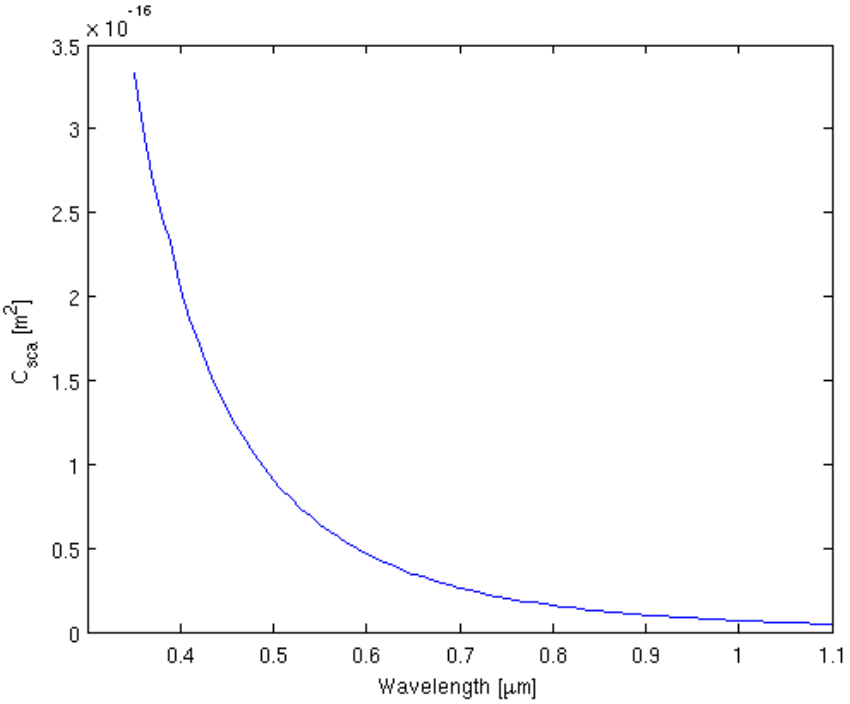

Figure 6.8: Scattering cross section of randomly oriented PMC particles at various wavelengths simulated using publicly available T-Matrix code [51, 52].

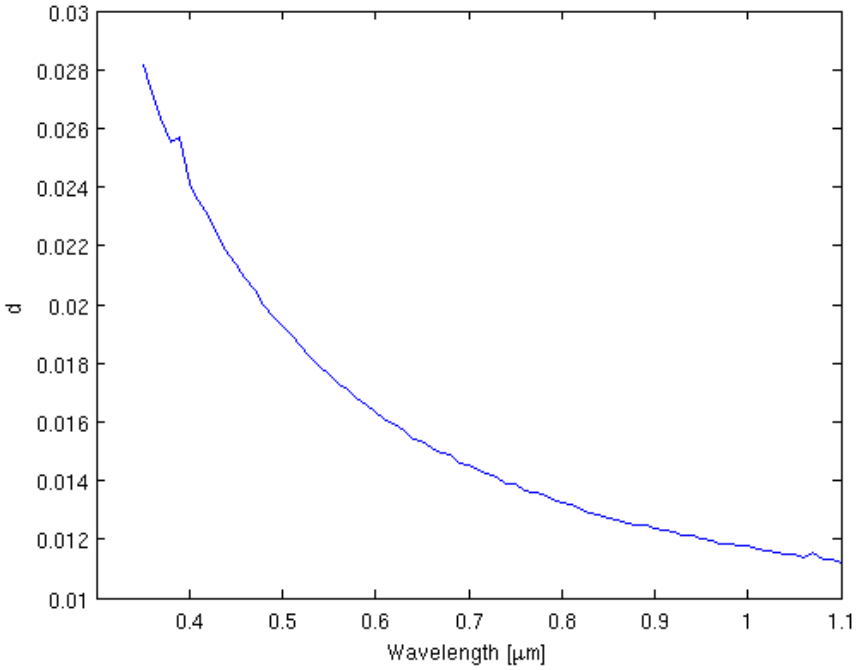

Figure 6.9: Depolarization of randomly oriented PMC particles using Mishchenko's FORTRAN T-Matrix code [51, 52] at different incident wavelengths.

decreasing wavelength (see Figure 6.9). As aspheric features on the particles become larger relative to the wavelength, we would expect their effects to be more pronounced.

6.2.2 Lidar Observations

PMC experiments were performed with the ARCLITE system using polarization calibration methods discussed in Chapter 5, during the summer months of 2009. The data presented here corresponds to a particular PMC event that occurred on July 26, 2009.

6.2.2.1 System Polarization Calibration

During this experiment, hardware and software compensation were applied to the data. The perpendicular and parallel lidar signals were integrated temporally for 150 minutes, spatially for 1.1 km, and background subtracted before performing the depolarization analysis. In the first step of the analysis the bias error is estimated using Rayleigh signals from 30-40km. The depolarization is calculated for each 1.1 km range-resolution increment and illustrated in Figure 6.10.

As no aerosols are present in the middle atmosphere, the estimate of d should have a value near 0.0088 owing to a Rayleigh depolarization ratio of $\delta = 0.0044$ which results from the receiver bandwidth being limited by a 532 nm interference filter with a 0.5 nm passband [9]. Because the lidar receiver bandwidth is wide enough to pass some rotational Raman lines in the molecular spectrum, this depolarization is slightly larger than that reported for the central Cabannes line ($d = 0.00727$ at 532 nm [11]). The noise with increasing altitude is due to increasing statistical uncertainty in signal. The error estimate $\sigma_d(z)$ reflects the shot-noise dominance in the signal, with exponential increase in uncertainty with altitude. This verifies the compensation methods shown here eliminate system biases to produce a nearly bias-free, well below 1%, estimate of depolarization. This is important in PMC studies as it is expected the clouds will produce single-digit percentages of depolarization.

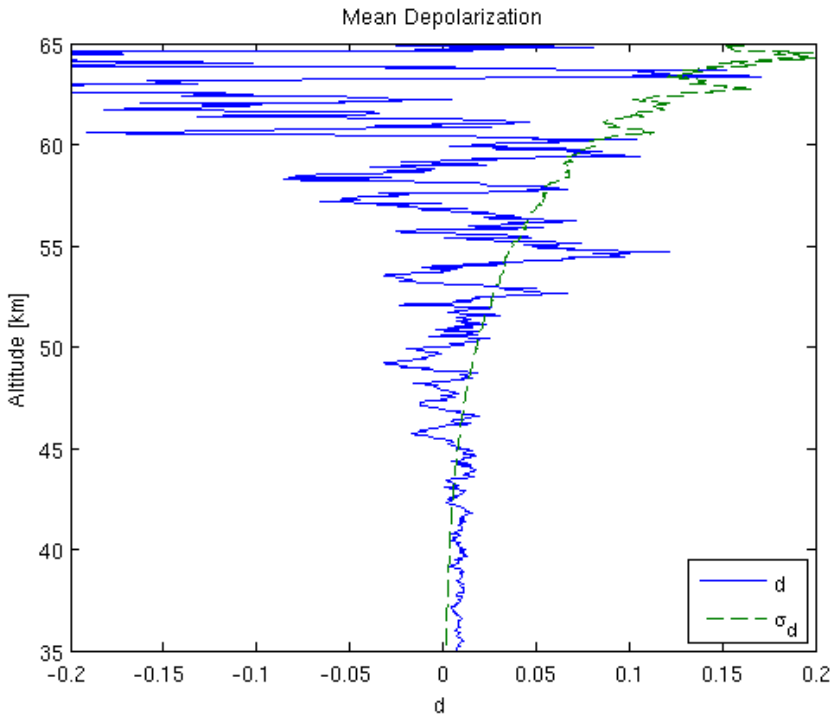

Figure 6.10: A vertical profile of the depolarization estimate from Rayleigh scattering (solid) with the computed error (dashed).

6.2.2.2 PMC Depolarization Measurements

The depolarization analysis is now applied to the lidar data for the same day as Figure 6.10 but at PMC altitudes. This PMC is relatively strong, with a Rayleigh backscatter equivalent altitude of 59 km. The depolarization estimate and profile are illustrated in Figure 6.11. The PMC was detected and integrated for 150 minutes (3:04-5:34 AM GMT, SZA 93.4°-90.2°) and the observation has an altitude resolution of 336 m. The average total backscatter profile is illustrated by the red, dashed line in Figure 6.11. The estimate of d is on the threshold of those expected for non-spherical PMCs but of significant uncertainty. Upon careful implementation and evaluation to remove systematic biases, the error in d is now dominated by statistical uncertainty associated with limited signal counts and elevated background counts. A further improvement in SNR by a factor of ten would suppress the statistical uncertainty to below 1% and enable non-spherical estimates to be more definitive. The reader should be aware that due to the long integration times associated with PMC depolarization measurements, the particles sampled may vary substantially in size, shape, and altitude. Thus any conclusions drawn from these integrated PMC polarization measurements apply to the cloud only in a long term average sense.

6.2.3 Error and Resolution

Due to low signal levels in terrestrial based PMC studies, shot noise dominates depolarization uncertainty. In such a case, the random arrival of photons within a specific time bin is governed by a Poisson distribution [93] so the probability of recording N counts is given by

$$p(N;\alpha) = \frac{\alpha^N e^{-\alpha}}{N!}, \tag{6.4}$$

where α is the mean photon counts recorded. The variance of the photon counts is equal to the number of the counts.

$$\sigma_N^2 = N \tag{6.5}$$

Since depolarization of the PMC is calculated using Eq. (4.4), error in the depolarization

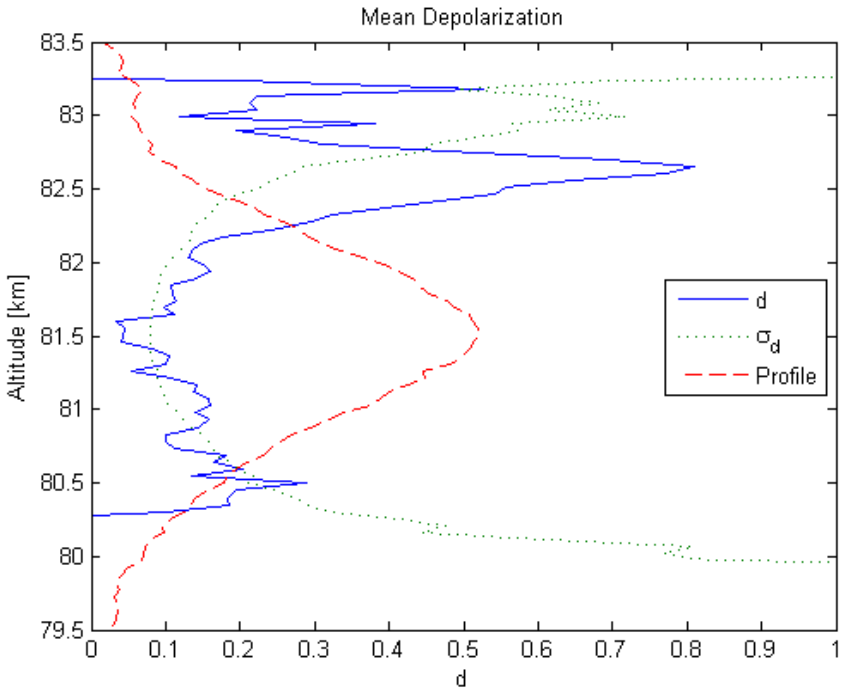

Figure 6.11: A PMC observation by the ARCLITE lidar July 26, 2009. The depolarization measurement is shown in blue (solid), uncertainty in green (dotted), and relative backscatter profile in red (dashed).

estimate can be calculated by propagation of error [68].

$$\sigma_d^2 = \sigma_{N_{||}}^2 \left(\frac{\partial d}{\partial N_{||}}\right)^2 + \sigma_{N_\perp}^2 \left(\frac{\partial d}{\partial N_\perp}\right)^2 \tag{6.6}$$

Using the definition of d in Eq. (4.4) and the definition of variance for a Poisson random variables, Eq. (6.6) may be written

$$\sigma_d^2 = \frac{4N_{||}N_\perp}{\left(N_{||} + N_\perp\right)^3} \tag{6.7}$$

where $N_{||}$ and $N_\perp$ are the parallel and perpendicular channel received photon counts respectively. This equations provides an easy means of determining the error in depolarization estimates from a specific PMC data sample, but we can also look at how it relates to the scattering and design parameters. Substituting the measurements described by Eq. (4.1), (4.2) and (4.3) into Eq. (6.7) yields depolarization variance as a function of the total received photons and depolarization

$$\sigma_d^2 = \frac{N_{RX}}{2}\left(d - \frac{d^2}{2}\right) \tag{6.8}$$

where N_{RX} is the sum of received photons on both polarization channels. We then define the depolarization resolution as

$$R_d = \frac{d}{\sigma_d} \tag{6.9}$$

which defines our ability to resolve depolarization, and therefore resolve the asphericity of the PMC particles. Large values of R_d are desirable for determining the asphericity of PMC particles. Substituting Eq. (6.8) into Eq. (6.9) gives the depolarization resolution as a function of the received photons and depolarization.

$$R_d = d\sqrt{\frac{N_{RX}}{2\left(d - \frac{d^2}{2}\right)}} \tag{6.10}$$

which for small d may be written

$$R_d \approx \sqrt{\frac{N_{RX}d}{2}} \tag{6.11}$$

Thus it becomes apparent that achieving low error in depolarization estimates requires large signal. Also, larger depolarization provides higher resolution. To measure a depolarization of 0.01 with a minimum resolution of $R_d = 10$ requires at least 2×10^5 photons.

From Eq. (2.1) the total received photons are proportional to the total transmitted photons N_L, receiver aperture area A, and scattering cross section $C_{sca}(\lambda)$ which is a function of wavelength. We can also write the total transmitted photons as a function of the laser pulse energy

$$N_L = \frac{E_p \lambda}{hc} r \Delta t \tag{6.12}$$

where E_p is the energy in each laser pulse, λ is the transmit wavelength, h is Planck's constant, c is the speed of light, r is the laser pulse repetition rate, and Δt is the detection integration time which is an integer multiple of the repetition period. Thus we may write a proportionality relationship between the depolarization resolution, fundamental system design parameters and the wavelength dependent scattering characteristics of the PMC.

$$R_d \propto \sqrt{E_p r \Delta t A \lambda d(\lambda) C_{sca}(\lambda)} \tag{6.13}$$

When the product of $d(\lambda)$ and $C_{sca}(\lambda)$ decrease, the laser power, integration time, laser repetition rate or some combination of the three must increase to maintain the same depolarization resolution. The design parameters of the instrument are held constant and this proportionality is plotted as a function of wavelength in Figure 6.12, where the values have been normalized to a transmission wavelength of $1.1\mu m$. Thus, when operating at $1.1\mu m$, design parameters must be improved by a factor of 7.6 to achieve the same depolarization resolution at $0.35\mu m$.

In the case of a Nd:YAG laser, the fundamental wavelength is $1.064\mu m$. Since the square of the relative depolarization resolution is proportional to the pulse energy, we determine the second harmonic generation at $0.532\mu m$ must have a conversion efficiency of greater than 9% to produce depolarization resolution better than that achieved by operation at the fundamental. Additionally, to achieve comparable results by going to the third harmonic at $0.355\mu m$, the total conversion efficiency must be better than 2%. It is clear that higher harmonics will likely produce better depolarization results than the fundamental.

For the purpose of achieving a measurable depolarization from PMCs, we have considered using the third harmonic of the Nd:YAG laser at 355 nm. Using Figure 6.12 it is clear that the

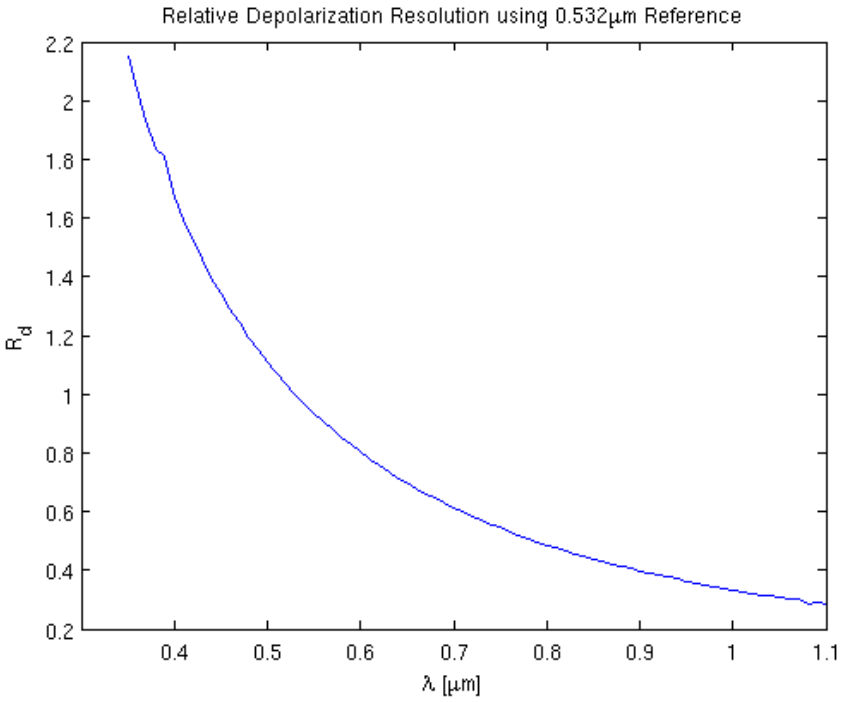

Figure 6.12: Relative depolarization resolution for lidar systems operating in or near the visible. The resolution has been normalized to the value at $0.532\mu m$.

depolarization resolution would improve by roughly a factor of 2. Assuming filter transmission and detector efficiencies are comparable between the two wavelengths, the conversion efficiency to 355 nm must be better than 50% from the 532 nm second harmonic to achieve depolarization resolution equal to our present second harmonic configuration. When we consider that solar background will also likely be larger at this shorter wavelength due to increasing molecular Rayleigh scattering, it is unlikely that a ground based system such as ARCLITE will benefit substantially in the area of PMC depolarization by operating a 355 nm channel. Instead, ARCLITE will most likely see the greatest improvement in PMC depolarization resolution through increased system optical efficiency, higher detector quantum efficiency, and improved spectral filtering for background reduction.

Note that in this analysis, background noise terms have been omitted. These terms will serve to increase the shot noise term, while making no contribution to signal, further decreasing depolarization resolution. Such background terms can become significant drivers in PMC analysis since the clouds form in the summer months over the polar regions where sunlight conditions persist during the entire day. These terms should also be considered in lidar design. Background noise parameters would depend on receiver field of view, bandwidth and aperture size along with several other natural considerations such as solar spectrum, Fraunhofer lines and Rayleigh scattering cross sections of the molecular atmosphere.

6.3 Tropospheric and Stratospheric Aerosols

The improvements to the ARCLITE lidar's polarization retrieval capabilities have bettered the lidar's research capabilities for tropospheric and stratospheric aerosols. In early January, 2011, several successive lidar runs occurred when a PSC was observed. Figures 6.13 and 6.14 show time resolved log backscatter counts and software corrected depolarization using the BigSky lasers. The total integrated depolarization profile is also shown in Figure 6.15. The PSC has a clear depolarization signature at approximately 25 km suggesting, on January 7, this is a Type Ib PSC.

In addition to the PSC, there is a layer of tropospheric aerosol that is faintly visible in the depolarization profile in Figure 6.14. The integrated profile in Figure 6.15 shows the layer has a

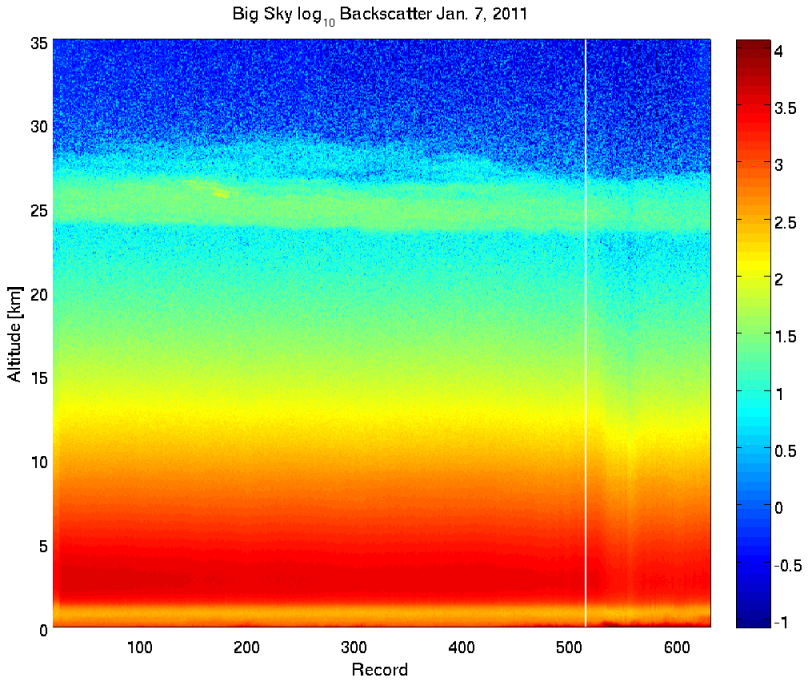

Figure 6.13: Log backscatter photon counts on January 7, 2011 as a function of time. The PSC is clearly visible throughout the data set at 25 km. Each record is one minute long.

peak depolarization of approximately 0.03. This serves as demonstration that the ARCLITE lidar is capable of resolving small depolarizations when sufficient signal is available. Thus with greater backscattered signal, PMC depolarization should be resolvable.

A PSC is also observed in another lidar run on January 6. Included in the data set are also cirrus clouds and tropospheric aerosols. The time resolved log backscatter counts and software corrected depolarization are shown in Figures 6.16 and 6.17. In this data set, the PSC is not substantially depolarizing, but continues to persist in the backscatter count data.

A thin layer of tropospheric aerosol is only visible in the depolarization profile between 5 and 6 km through the run. This helps illustrate the utility of depolarization measurements, which may register the presence of aerosols not easily observed using backscatter.

An isolated cirrus cloud is weakly resolvable at 10 km in the backscatter profile near record 250. The depolarization profile registers a depolarization of 1. We believe the high depolarization

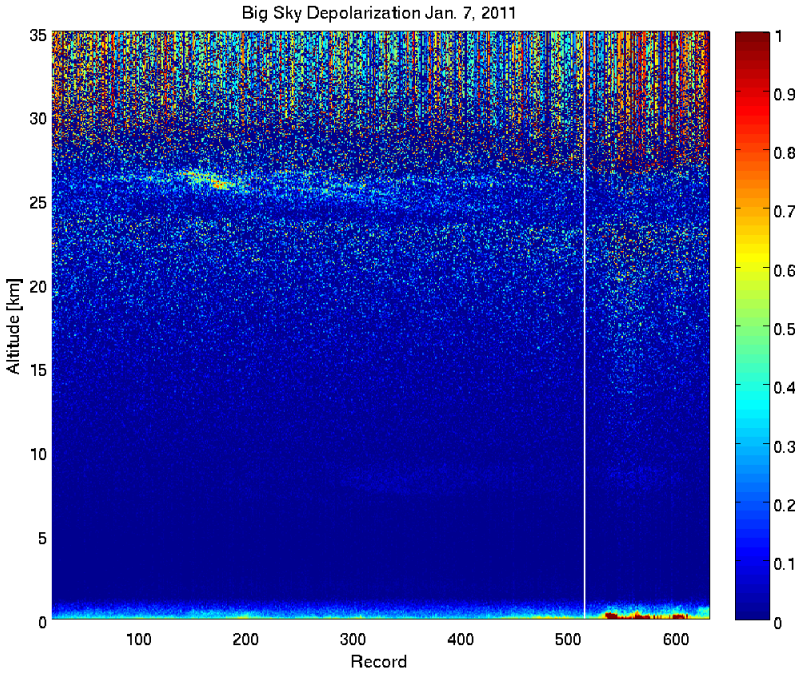

Figure 6.14: Depolarization on January 7, 2011 as a function of time. While the cloud backscatter intensity is relatively uniform, it has occasional streaks of substantial depolarization. Also, an aerosol layer can be seen in this profile between 5 and 10 km starting near record 300.

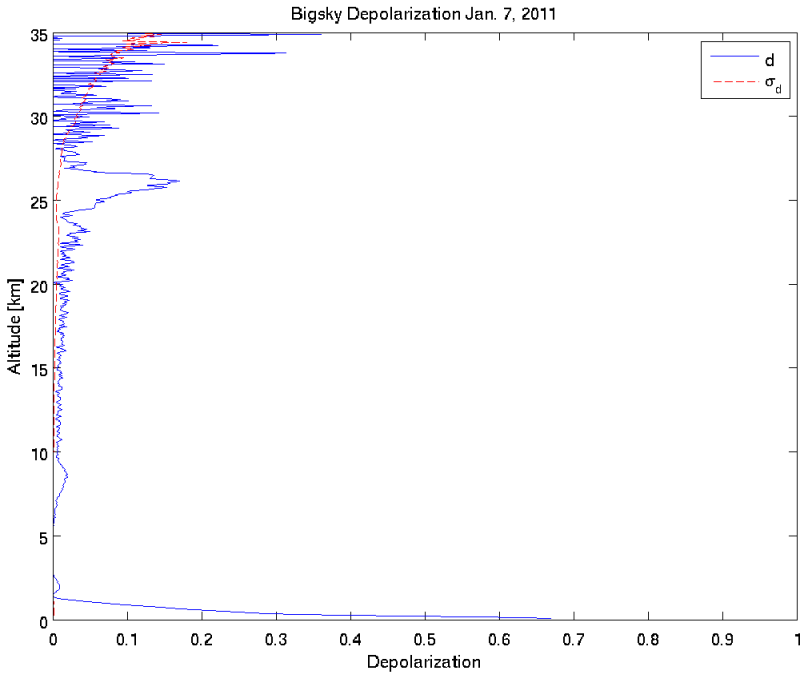

Figure 6.15: Integrated depolarization of PSC observed on January 7, 2011. The streaks of depolarization observed in Figure 6.14 result in a substantial depolarizing signature in the cloud. The tropospheric aerosol layer is clearly visible in this profile, demonstrating the level of polarization sensitivity of this instrument after correction of polarization effects.

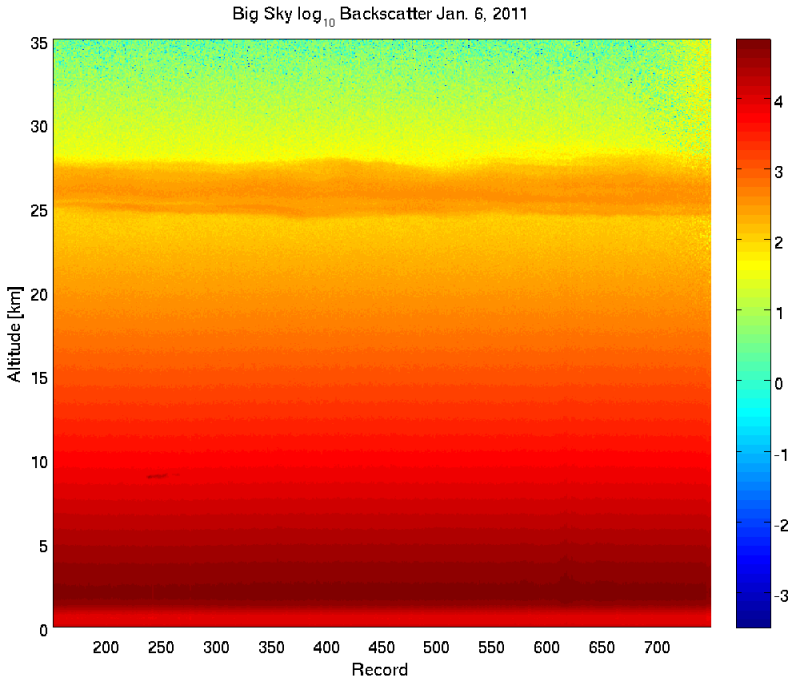

Figure 6.16: Backscatter profile of a PSC, cirrus cloud and tropospheric aerosol observed on January 6, 2011. The PSC persists at approximately 25 km while a cirrus cloud is only briefly visible at 10 km near record 250. The aerosol layer near 5 km cannot be seen in the backscatter profile.

is attributable to substantial detector nonlinearity. The lidar return from this cloud is likely due to specular reflections from oriented ice crystals. Though the actual return light should have little or no depolarization, detector saturation causes the calculated depolarization to approach 1.

Diattenuation data was also recorded for the PSC on January 4, 2011 using ACP. The BigSky lasers already transmit cross polarization laser pulses so this modification only requires that we remove the polarizer in the receiver. The resulting data is shown in Figures 6.18 and 6.19. Since the lidar is zenith pointing we observe no diattenuating signatures. However, this shows that diattenuation profiles can be measured without false positives using ACP on ARCLITE. Future experiments with ARCLITE may involve tilting the lidar off zenith to look for oriented scatterers.

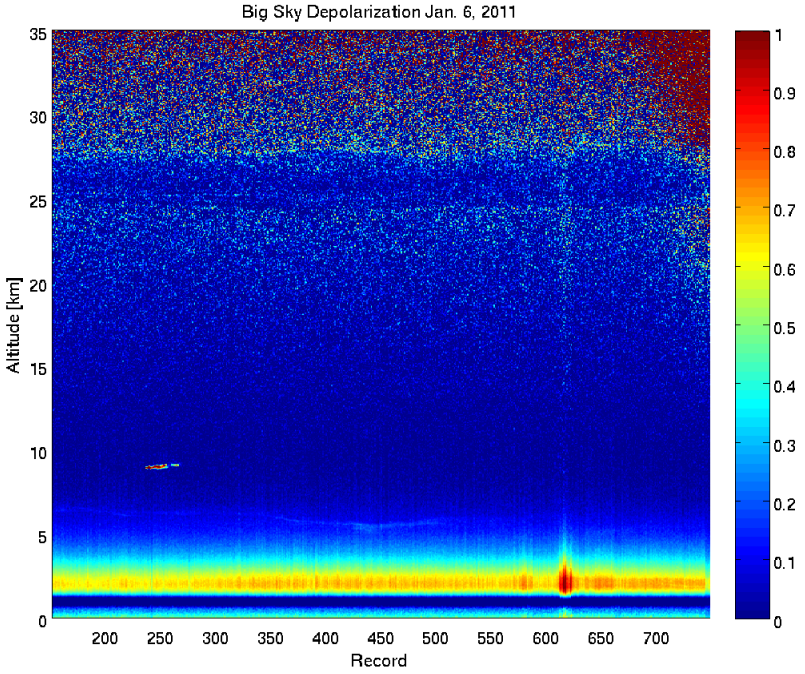

Figure 6.17: Depolarization profile of a PSC (25-27 km throughout the dataset), cirrus cloud (9 km near Record 250) and tropospheric aerosol (6-7 km, most apparent between records 350 and 500) observed on January 6, 2011. The PSC has little or no depolarizing signature while the cirrus cloud appears to be completely depolarizing. We believe this is the result of very detector saturation due to specular reflections from oriented scatterers. The aerosol layer is much easier to see in depolarization than backscatter.

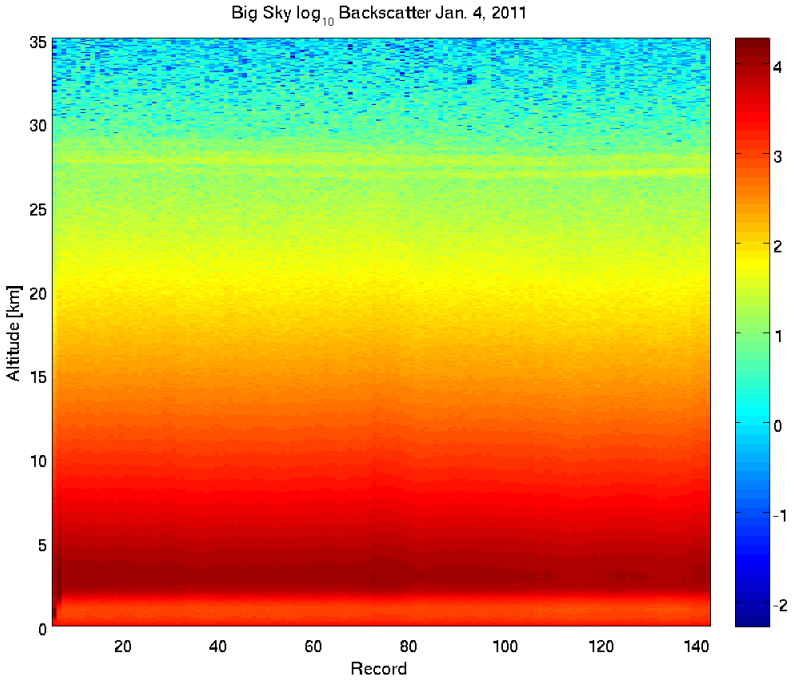

Figure 6.18: Backscatter profile of a PSC observed on January 4, 2011 during diattenuation measurements using ACP.

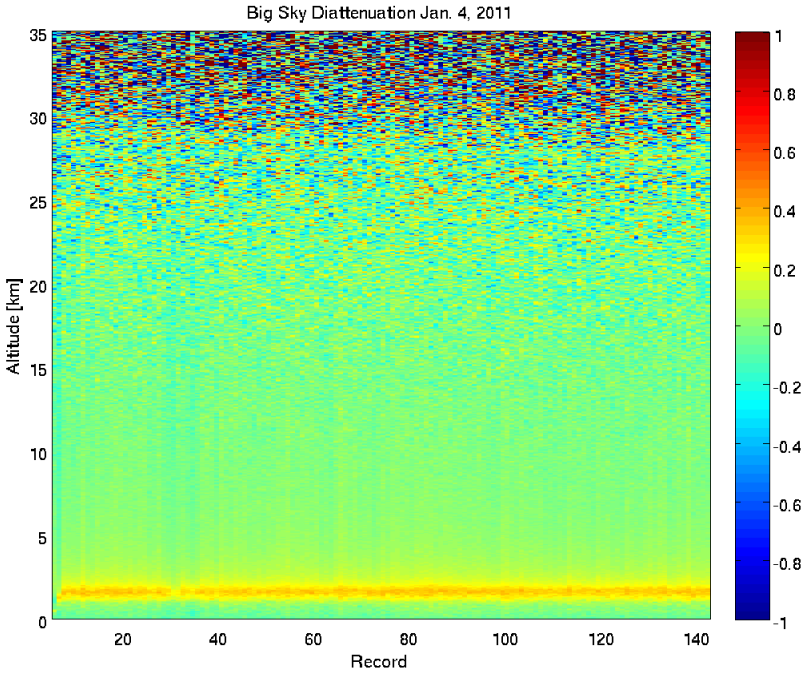

Figure 6.19: Diattenuation profile of a PSC observed on January 4, 2011. The profile was measured using ACP and demonstrates the expected zero diattenuation for a zenith pointing lidar.

Chapter 7

Cloud Aerosol and Backscatter Lidar

As part of the Integrated Characterization of Energy, Clouds, Atmospheric State, and Precipitation over Summit (ICECAPS) program a decommissioned NOAA lidar was redesigned and deployed to Summit Camp, Greenland ($72.6°N, 38.5°W$) in spring of 2010. The lidar was named the Cloud Aerosol and Backscatter Lidar (CAPABL) and has a primary objective to identify tropospheric cloud phase above the camp. Two secondary goals were also added, to interrogate of stratospheric aerosols and identify oriented ice crystals. Because the mission's primary objective requires conventional polarization lidar operation, CAPABL needed to offer all the standard capabilities of conventional polarization lidar. Thus the P45P polarization technique was an ideal solution, providing depolarization measurements with the additional diattenuation data product for detection of oriented scatterers.

CAPABL is a refurbished version of NOAA's Depolarization and Backscatter Unattended Lidar (DABUL). All hardware modifications were identified and implemented within a six month time frame and largely confined, with the exception of the purchase of a liquid crystal variable wave plate, to existing DABUL components.

7.1 System Layout

The CAPABL lidar system uses a frequency doubled diode pumped Nd:YLF operating at 523.5 nm from its predecessor system. The laser is first passed through a HWP and polarizer with 1000:1 extinction to ensure maximum power and linearly polarized output (see Figure 7.1). Because

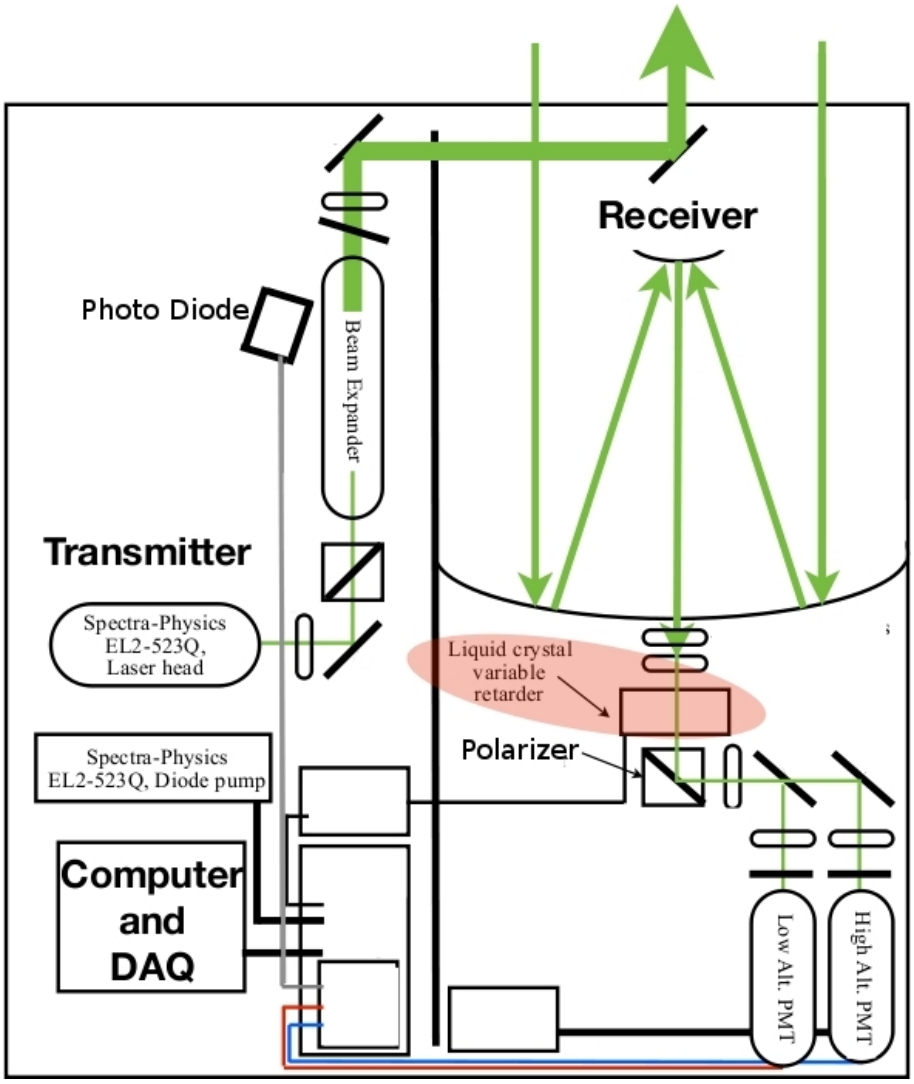

Figure 7.1: Layout of CAPABL transmitter and receiver. The lidar transmits a single linear polarization, then using a QWP and variable retarder, detects linear polarizations parallel, 45° and perpendicular to the transmit polarization.

the transmitter uses several mirrors and budgetary and time constraints prevented the acquisition of additional QWPs to build a compensator, the linear polarization is aligned to LiLo (the linear input polarization that produces a linear output polarization) of the transmitter. This defines the polarization basis of the system operation. After the polarizer, the laser is beam expanded by 80 times for low divergence. The beam is then sampled by a photodiode to time stamp the laser pulse transmission time. Finally two folding mirrors align the transmitted beam to the receiver secondary. This allows for a full overlap with the receiver field-of-view (FOV) at low altitudes (below 100 m) for tropospheric boundary layer studies.

The receiver uses an F/14.3 Dall-Kirkham telescope with 508 cm focal length and 35.6 cm aperture to minimize polarization effects (see Table 7.1 for full system specifications). This telescope uses a spherical primary and elliptical secondary mirror in a Cassigrain configuration which results in high coma. In lidar we only intend to collect on axis light, so this coma does not present an issue. The collected light is then collimated by a 30 mm lens and passed through a horizontally oriented QWP with a Meadowlark liquid crystal variable retarder oriented at 45° and a horizontal polarizer. The combination of these polarization elements act as a rotating analyzer. After the polarizer, 10% of the signal is passed to the low altitude PMT with low gain to avoid saturation from high intensity signals below 1 km in altitude. The remaining 90% of the signal is passed to the high gain channel for upper tropospheric and lower stratospheric data collection.

The overall lidar control and data acquisition is run by a Labview program on a PC with internet connection. The lidar, in its present configuration can be remotely controlled, only requiring an operator for hardware maintenance and modifications.

7.1.1 Polarization Operation

CAPABL uses a Meadowlark liquid crystal variable retarder (VWP) in the receiver to perform the three polarization measurements necessary for the P45P technique. The VWP is aligned to 45°

Table 7.1: CAPABL System Specifications

Wavelength	523.5 nm
Laser Pulse Energy	40 μJ
Laser Repetition Freq.	2 kHz
Laser Pulse Length	10 ns
Telescope Type	Ag Coated Dall-Kirkham
Telescope Focal Length	508 cm
Telescope Aperture	35.6 cm
Telescope F/#	14.3
Field of View	$< 0.3\ \mu rad$

so its Mueller matrix is

$$\mathbf{V}(\Gamma_{wp}, 45^\circ) = \begin{bmatrix} 1 & 0 & 0 & 0 \\ 0 & \cos\Gamma_{wp} & 0 & \sin\Gamma_{wp} \\ 0 & 0 & 1 & 0 \\ 0 & -\sin\Gamma_{wp} & 0 & \cos\Gamma_{wp} \end{bmatrix}, \tag{7.1}$$

where Γ is the voltage controlled phase shift of the VWP. The VWP in series with the horizontal polarizer allows the polarizer to select any polarization along the horizontal meridian of the Poincarè sphere by adjusting Γ. However, we wish to have the polarizer select any polarization component along the equator to act as a linear polarizer. To accomplish this, we must transform all linear polarization components on the equator to the meridian passing through horizontal polarization. This can be achieved by placing a horizontal QWP in front of the VWP and polarizer. The polarization analyzer Mueller matrix is then given as follows:

$$\mathbf{A}\left(\frac{\Gamma_{wp}}{2}\right) = \mathbf{P}(0)\mathbf{V}(\Gamma_{wp}, 45^\circ)\mathbf{Q}(0) = \frac{1}{2}\begin{bmatrix} 1 & \cos\Gamma_{wp} & \sin\Gamma_{wp} & 0 \\ 1 & \cos\Gamma_{wp} & \sin\Gamma_{wp} & 0 \\ 0 & 0 & 0 & 0 \\ 0 & 0 & 0 & 0 \end{bmatrix}, \tag{7.2}$$

where $\mathbf{P}(\theta)$ is a polarizer oriented at angle θ, $\mathbf{V}(\Gamma_{wp}, \theta)$ is a VWP of phase shift Γ and orientation θ and $\mathbf{Q}(\theta)$ is a QWP of orientation θ. The total analyzer matrix in Eq. (7.2) is qualitatively different from a rotated linear polarizer only in the fact that its polarizance is always horizontal.

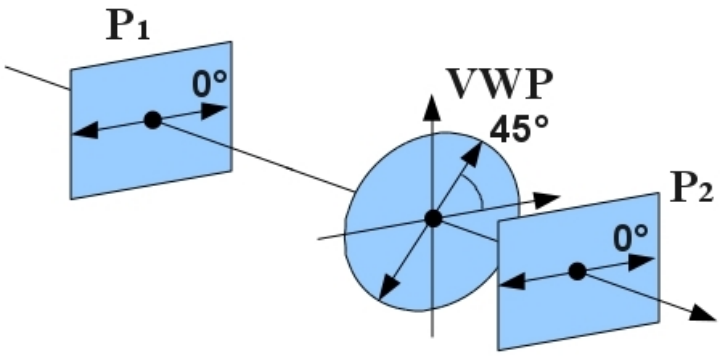

Figure 7.2: Initial schematic of optics for analyzer optimization. First polarizers P_1 and P_2 must be aligned to be horizontal relative to the VWP that defines 45°.

The diattenuation (polarization transmission efficiency) of the analyzer matrix is a function of the VWP phase shift Γ_{wp} so that the transmitted efficiency is identical to that of a linear polarizer at angle $\frac{\Gamma_{wp}}{2}$. However, the polarization after the analyzer will always be linear horizontal. This single exiting polarization is desirable, because it means optical components following the polarizer will always see the same polarization allowing us to ignore polarization effects after the analyzer.

7.1.1.1 Analyzer Optics Optimization

It is important that we are able to properly align all the components in CAPABL's polarization analyzer to obtain the high polarization accuracy required for diattenuation measurements of oriented scatterers. For this purpose, an alignment procedure was developed for the polarizer, VWP and QWP that make up the polarization analyzer.

The VWP has no capability to rotate in its mount, so its orientation defines 45° in the analyzer setup. All other components must be aligned to it. To start, the configuration shown in Figure 7.2 is used where an arbitrarily polarized laser is passed through a polarizer P_1, the VWP and then a second polarizer P_2 after which the laser light is detected. Both polarizers are roughly aligned to pass horizontally polarized light. In this configuration, P1 is not a permanent part of the setup and will be removed after optimization takes place. The Mueller matrix description of

the setup in Figure 7.2 is

$$I_{det}(\theta_1, \Gamma_{wp}, \theta_2) = \vec{o}\mathbf{P}(\theta_2)\mathbf{V}(\Gamma_{wp}, 45^\circ)\mathbf{P}(\theta_1)\vec{S}_{in}, \tag{7.3}$$

where $I_{det}(\theta_1, \Gamma, \theta_2)$ is the received intensity on the detector which is a function of polarizer angles θ_1 and θ_2 and the VWP phase shift Γ. The output column vector denotes that only intensity is measured

$$\vec{o} = \begin{bmatrix} 1 & 0 & 0 & 0 \end{bmatrix}, \tag{7.4}$$

and $\vec{S}_{in}$ is the input Stokes vector of the laser light. For simplicity, we will assume the input laser light is unpolarized and of intensity 1. Evaluating Eq. (7.3) we find the detected intensity is given by

$$I_{det}(\theta_1, \Gamma_{wp}, \theta_2) = \frac{1}{4}\left(1 + \cos\Gamma_{wp}\cos 2\theta_1 \cos 2\theta_2 + \sin 2\theta_1 \sin 2\theta_2\right). \tag{7.5}$$

A relatively simple Labview program is written to modulate the phase shift Γ_{wp} on the VWP so that it passes through all values from 0 to π. In Eq. (7.5) we see that the maximum and minimum detected intensities of this modulation will correspond to $\Gamma = 0$ and $\Gamma = \pi$ respectively. Recalling that the polarizers are set near horizontal, the maximum intensity is

$$I_{det}(\theta_1, 0, \theta_2) = \frac{1}{2}\cos^2\left(\theta_1 - \theta_2\right), \tag{7.6}$$

and the minimum is

$$I_{det}(\theta_1, \pi, \theta_2) = \frac{1}{2}\sin^2\left(\theta_1 + \theta_2\right). \tag{7.7}$$

If we measure the peak-to-peak intensity as a function of polarizer angle, it is given by

$$I_{pp}(\theta_1, \theta_2) = I_{det}(\theta_1, 0, \theta_2) - I_{det}(\theta_1, \pi, \theta_2) = \frac{1}{2}\cos 2\theta_1 \cos 2\theta_2. \tag{7.8}$$

Thus, each polarizer may be independently set to horizontal (rotation angle of 0°) by maximizing the peak-to-peak intensity. The peak-to-peak intensity should be maximized by rotating P_2 for proper alignment of the optic in the analyzer. The polarizer P_1 should also be aligned to horizontal through the same procedure to ensure proper alignment of the QWP in the next step.

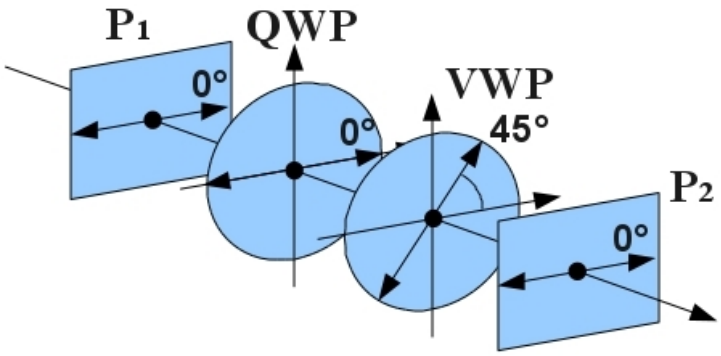

Figure 7.3: Final schematic of optics for analyzer optimization. With P_1 and P_2 horizontal, the QWP is added and aligned to horizontal. After optimization is complete P_1 is removed.

We now insert the QWP between P_1 and the VWP as shown in Figure 7.3 so that its fast axis is roughly horizontal. Through the previous steps, the orientations of the two polarizers have already been set to 0° and the detected intensity is now

$$I_{det}(\Gamma_{wp}, \theta_q) = \vec{o}\mathbf{P}(0^\circ)\mathbf{V}(\Gamma_{wp}, 45^\circ)\mathbf{Q}(\theta_q)\mathbf{P}(0^\circ)\vec{S}_{in} \tag{7.9}$$

where the orientation of the QWP fast axis is θ_q. Eq. (7.9) then simplifies to

$$I_{det}(\Gamma_{wp}, \theta_q) = \frac{1}{4}\left(1 + \cos\Gamma_{wp}\cos^2 2\theta_q - \sin\Gamma_{wp}\sin 2\theta_q\right). \tag{7.10}$$

We continue to modulate the phase of the VWP and the maximum detected intensity will either correspond to $(\Gamma = 0, \theta_q = 0)$ or $\left(\Gamma = -\frac{\pi}{2}, \theta_q = 45^\circ\right)$. Because the QWP was inserted near horizontal, the closest maximum in intensity corresponds to a horizontal fast axis. This means there should not be a significant phase shift in the modulated intensity when optimizing the QWP. The incorrect maximum would result in a phase shift of $\frac{\pi}{2}$.

If the alignment angle of the QWP is not known when it is inserted into the setup, it is possible to determine this by observing the change in intensity maximum as a function of QWP rotation. Acceptable orientations exist at $\theta_q = m45^\circ$ where m is an even integer including zero. Undesirable orientations exist where m is an odd integer. If a maximum in intensity is found, the QWP can be rotated by 90°. If this rotation does not cause a π phase shift in the intensity waveform, the correct (even) m was chosen. If this rotation causes a π phase shift in the modulated

intensity waveform, wrong (odd) m was chosen.

Once the QWP in the analyzer is aligned to horizontal, the polarizer P_1 is removed. The remaining optics make up the polarization analyzer as described before.

This optical configuration can also be used when m is odd to determine the fast axis of a QWP. If we know the fast axis is either aligned to $45°$ or $-45°$, the cosine term in Eq. (7.9) becomes zero. If the fast axis is aligned to $45°$, the detected intensity will modulate π out of phase with the VWP phase shift. However, if the fast axis is aligned to $-45°$, the intensity will modulate in phase with the VWP phase shift.

7.2 VWP Control

The Meadowlark Variable Retarder imposes a voltage controlled phase shift between polarization modes. However the exact phase shift drifts as a function of wavelength and temperature. CAPABL is contained in a temperature controlled room at Summit. However, some temperature drift does occur in the room. A sensitivity analysis of diattenuation measurements for a relative phase shift error of $\Delta\Gamma_{wp}$ is performed. For a depolarizing medium, the received photon counts as a function of phase shift on the VWP are given by

$$N_{RX}(\Gamma_{wp}) = \frac{N_0}{2}\left[1 + (d-1)\cos\Gamma_{wp}\right], \tag{7.11}$$

where d is the medium depolarization for axially symmetric randomly oriented scatterers given by the scattering matrix in Eq. (3.5) and Γ_{wp} is the phase shift of the VWP. The objective of diattenuation measurements with CAPABL is to identify oriented scatterers. Thus, the primary concern is avoiding false positives in the presence of strictly randomly oriented scatterers.

Let error in VWP retardance due to temperature changes be approximately the same for all measurements. Because the room where CAPABL operates is heated through standard HVAC systems, this error is generally small. The received photon counts for a target phase shift Γ_{wp} and phase shift error $\Delta\Gamma_{wp}$ is expanded to first order

$$N_{RX}(\Gamma_{wp}) \approx \frac{N_0}{2}\left[1 + (d-1)\cos\Gamma_{wp}\right] - \frac{N_0}{2}(1-d)(\sin\Gamma_{wp})\Delta\Gamma_{wp}. \tag{7.12}$$

In the above equation, the second term corresponds to error in the detected photon counts. The first order error sensitivity of the perpendicular and parallel measurements at $\Gamma_{wp} = 0$ and $\Gamma_{wp} = \pi$ are zero. Also, if we evaluate the higher order expansion terms, they will always be equal and opposite. Since the two terms are summed in diattenuation calculations, their error terms will cancel. Thus, diattenuation measurements are relatively insensitive to VWP phase error in the perpendicular and parallel channels. Instead of employing active feedback, we can periodically recalibrate the VWP voltage settings and still maintain accurate measurements.

The 45° polarization measurement is made at $\Gamma_{wp} = \frac{\pi}{2}$ where Eq. (7.12) has maximum sensitivity to $\Delta\Gamma_{wp}$. If we evaluate the measured diattenuation using Eq. (7.12) we find

$$D_q = (1 - d)\Delta\Gamma_{wp}. \tag{7.13}$$

Because we are only considering randomly oriented scatterers here, D_q is strictly related to error. Thus, non-diattenuating scatterers can be used to determine the phase error of the VWP. This error, in turn, can be used in a feedback loop to control the VWP voltage for 45° polarization measurements.

To avoid costly additions to CAPABL's hardware, we close the feedback loop for VWP control in the control software using part of the lidar profile. However, to make precise corrections to the VWP voltage, the shot noise uncertainty must be low. Low altitude signals are used to close the feedback loop, where signals are strong and therefore have high SNR. To obtain a diattenuation uncertainty less than 0.01, however, we still must integrate the profiles in the feedback loop. Longer integration has the effect of reducing the control bandwidth. Phase shift drift caused by temperature fluctuations are expected to be slow, so system bandwidth is only a concern with regard to settling time when first closing the loop.

The total feedback control loop is shown in Figure 7.4. The input control signal is zero, because for non-diattenuating scatterers, we want to drive the detected diattenuation to zero. The control loop gain H is a constant determined through control system design. It includes conversion from VWP phase error to VWP voltage error, as well as the necessary gain for maximum

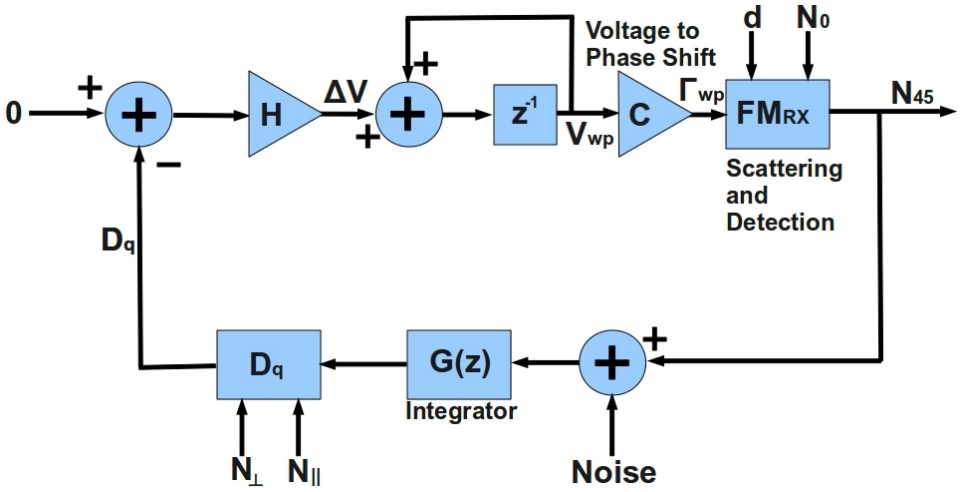

Figure 7.4: Block diagram of VWP feedback control for the 45° polarization measurement. More integration in $G(z)$ reduces uncertainty in the error estimate, but also slows down the feedback loop. The loop controls the measured diattenuation of the closed loop altitude to zero.

convergence speed while maintaining stability. The calculated correction is added to the previous VWP voltage. The new VWP voltage is applied to the 45° polarization measurement, denoted by C which converts VWP voltage back to phase shift. This VWP setting is used to detect the diattenuation of the atmospheric phase matrix $\mathbf{F}$ and receiver matrix $\mathbf{M_{RX}}$. Note that the result of this scattering problem is dependent on number of photons entering the receiver N_0, depolarization of the scatterer d and the VWP phase Γ_{wp}. From this Mueller matrix calculation, the N_{45} photon counts are determined. Since this scattering problem is well defined, the function can be simplified to

$$N_{45} = \frac{N_0}{2}\left[1 - (1-d)(\Gamma_{wp} - \frac{\pi}{2})\right], \tag{7.14}$$

where $\frac{\pi}{2}$ is the ideal phase shift for the 45° polarization measurement.

The resulting N_{45} signal is then fed into the integrator $G(z)$ which is designed to reduce shot noise uncertainty in the calculated error signal and is given by

$$G(z) = \frac{1}{K+1}\sum_{k=0}^{K} z^{-k}, \tag{7.15}$$

where K is the total number of integrations needed to sufficiently suppress shot noise. The last block, calculates the scatterer diattenuation using the measured polarization channel photon counts

at the feedback altitude.

The total transfer function from measured photon counts N_{45} to measured diattenuation is given by

$$\frac{D_q(z)}{N_{45}(z)} = \frac{(G(z)-1)(z-1)}{z-1+zH(1-d)G(z)C}. \tag{7.16}$$

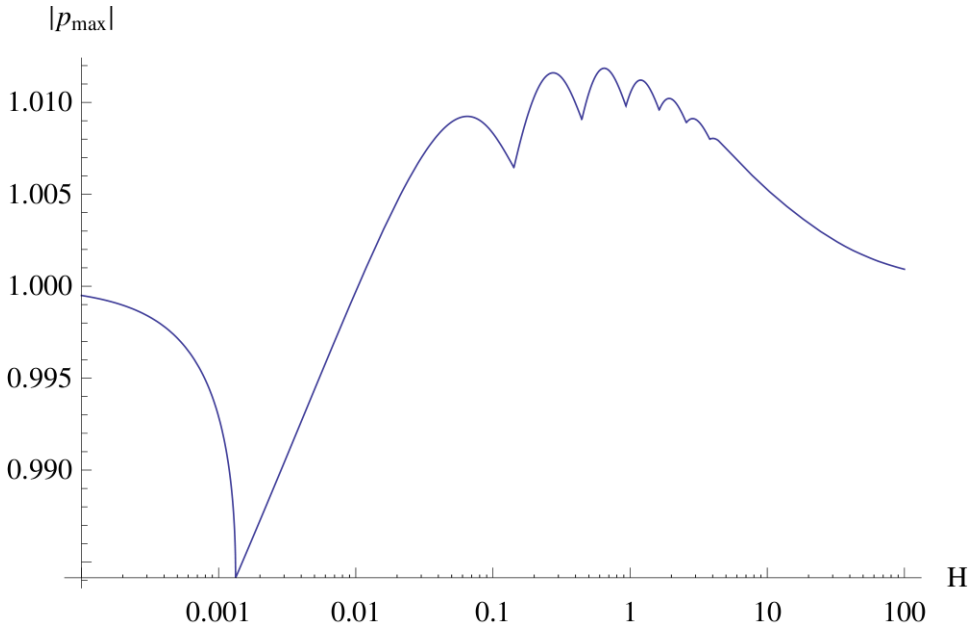

Figure 7.5: Largest pole magnitude of CAPABL feedback transfer function as a function of loop gain H. For this analysis the integrator $G(z)$ performs 100 integrations. For the VWP control loop to be stable, the magnitude of all poles must be less than one.

The poles of this transfer function determine the stability of the system. A discrete time system is stable when all poles are inside the unit circle. Thus we first choose the number of integrations in $G(z)$ to obtain a sufficiently low diattenuation resolution for the system. We then select H so that all poles are in the unit circle. Figure 7.5 shows the maximum magnitude pole in Eq. (7.16) for $K = 100$ integrations. In this case, the feedback loop is stable for feedback gain less than 0.007. However, the rate at which the VWP reaches steady state is determined by the slowest pole which converges as

$$\Delta\Gamma_{wp}[n] = |p_{max}|^n, \tag{7.17}$$

where n is the discrete time step and p_{max} is the pole with the largest amplitude. As the largest

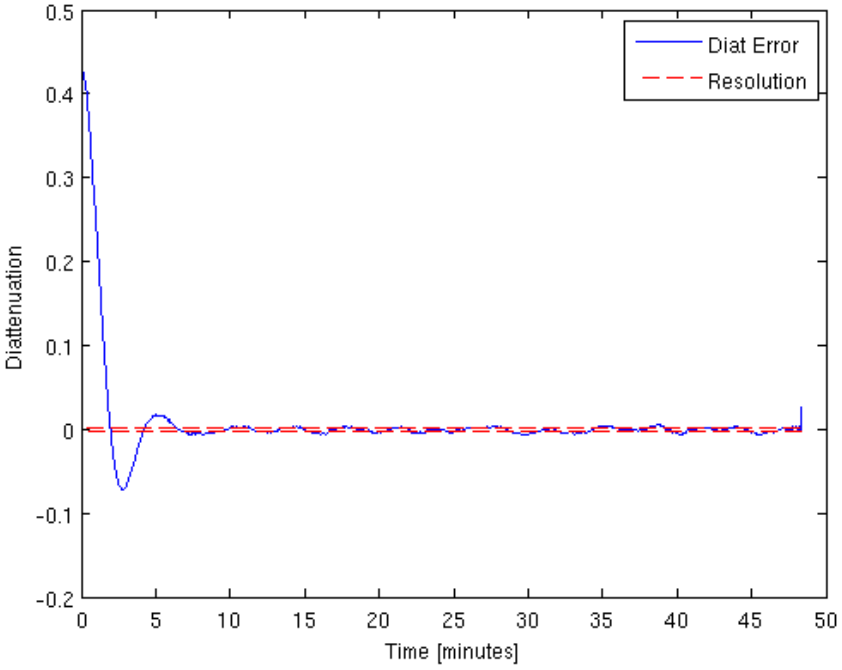

Figure 7.6: Diattenuation error of CAPABL determined by calculating diattenuation of the feedback altitude where the scattering matrix diattenuation is assumed to be zero. The feedback loop is closed at time zero where the error begins to fall. After 10 minutes the error stabilizes to less than the shot noise limited diattenuation resolution at the feedback altitude (red dashed lines) of ± 0.0015. This defines the diattenuation measurement accuracy of the system.

pole approaches 1, the rate of convergence will become infinite. For this reason, when $K = 100$ we want to choose $H = 0.002$ where the rate of convergence is maximum (the magnitude of the largest pole is minimized).

CAPABL was run with a 100 dataset integrator ($K = 100$) using scattering data from 0.1 to 0.7 km to close the feedback loop. Each dataset integrated 1000 shots from the 2kHz laser. The gain was set to $H = 0.004$ and the diattenuation of the feedback altitudes was observed. The result is shown in Figure 7.6. The starting VWP voltage for the 45° polarization measurement was significantly off the desired phase shift, resulting in an erroneous diattenuation measurement larger than 0.4. With the feedback loop active, the diattenuation converges toward zero, dropping below the resolvable diattenuation of the feedback loop after approximately 10 minutes. The diattenuation of the feedback altitude then remains at zero for the remainder of the run.

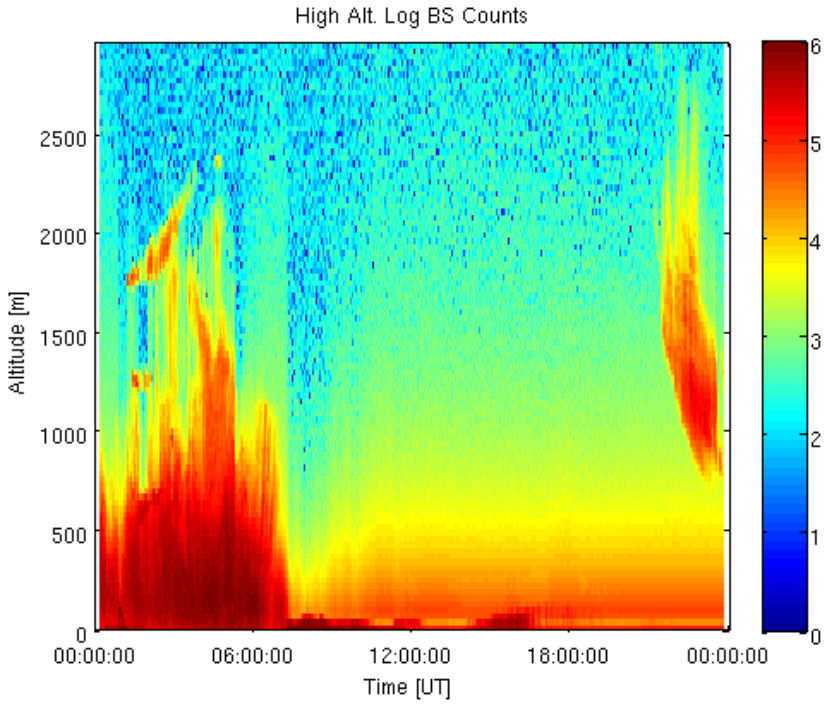

Figure 7.7: Total log backscatter detected by the CAPABL high altitude channel on June 14, 2010.

7.3 Preliminary Data

CAPABLE has run nearly continuously since May 2010, collecting polarization data using the P45P technique outlined in Chapter 4. For the first year of operation, the lidar is pointing near zenith (2° off zenith). In this configuration, horizontally oriented ice crystals do not exhibit diattenuation. Because horizontally oriented ice crystals are the only oriented scatterer events known to be regularly observed, it is regarded as unlikely that any data should show diattenuation signatures from oriented scatterers when the lidar is in this configuration. This expectation is used as a diagnostic to understand potential false positives in oriented scatterer detection.

Detector nonlinearity has been identified as the most significant contributor to error in CAPABL's diattenuation measurements. If the parallel measurement has lower photon count gain due to detector nonlinearity than the 45° or perpendicular measurements, diattenuation estimates will be biased. For diattenuation to be measured as zero, N_{45} must be exactly half of the total received power. Thus when the parallel channel reports less than the actual number of received photons,

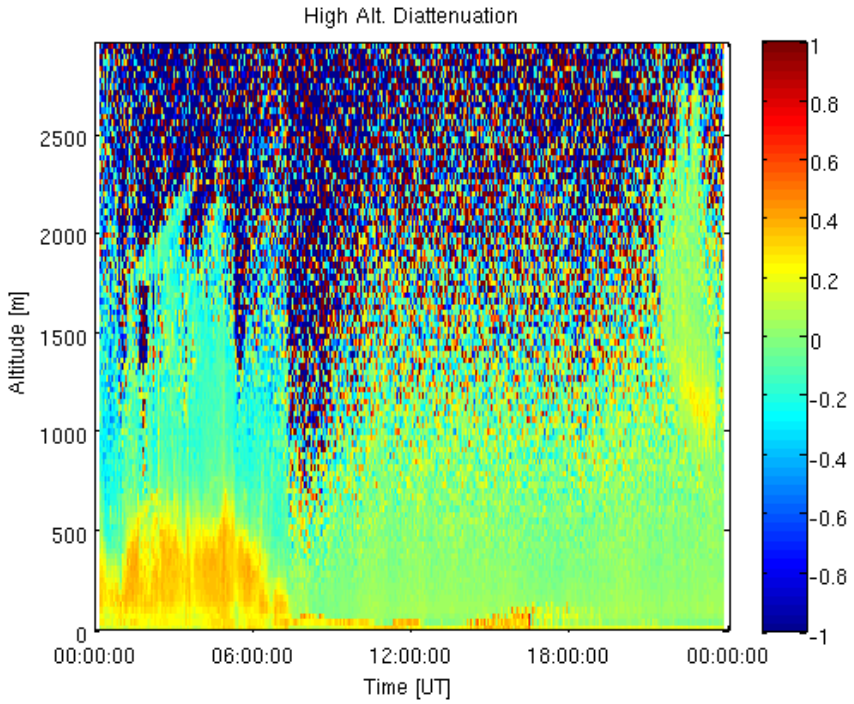

Figure 7.8: Diattenuation detected by the CAPABL high altitude on June 14, 2010. Detector nonlinearities result in false positives for oriented scatterers.

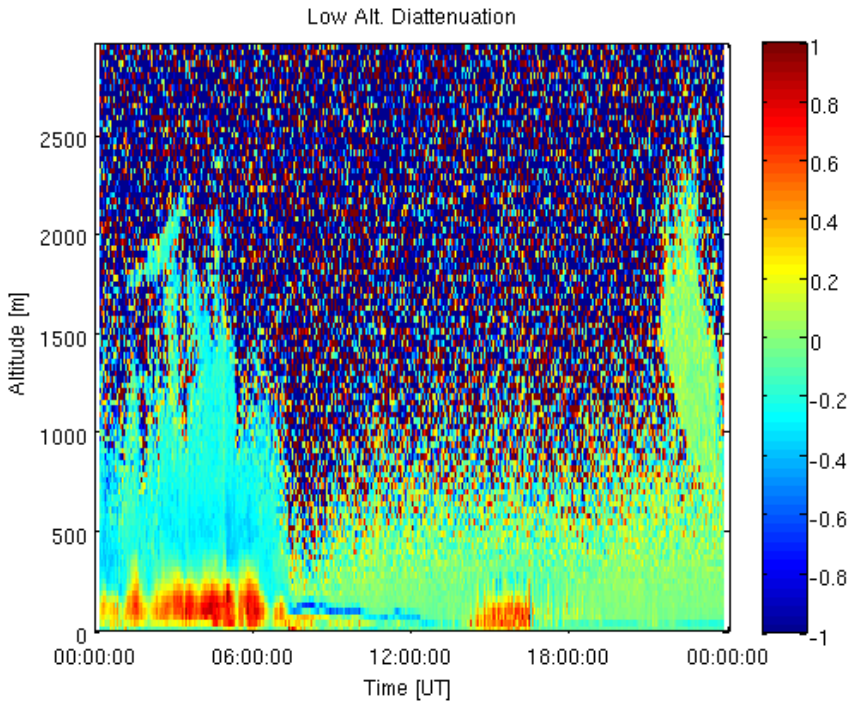

Figure 7.9: Diattenuation detected by the CAPABL low altitude on June 14, 2010. Note the non-zero diattenuation signature of the cloud near the end of the data set in Figure 7.8 is observed as zero on this lower gain channel.

the measured diattenuation shifts positive. Figures 7.7 and 7.8 show the log backscatter and diattenuation profiles of the high altitude data channel taken on June 14, 2010. Between times 20:00 and 0:00 UT a cloud descends from 2000 to 1000 m. The cloud appears to exhibit a significant diattenuation of approximately 0.2. We also analyze the corresponding low altitude data where the diattenuation profile is shown in Figure 7.9. Due to the reduced efficiency on the the low altitude channel, the detector stays linear for higher backscatter signals. Here we clearly see that the cloud exhibits no diattenuating effects. Nonlinearity does however occur in the low altitude channel from returns below 200 m between 00:00 and 06:00 UT. Thus detector nonlinearity presents an issue for false positives in detection of oriented scatterers. To test our confidence in cloud data, we check the corresponding photon count rate of diattenuating signals to determine if they are within the linear range of the detectors. Also, we check for consistency in diattenuation calculations from the lower and upper altitude detection channels.

A second issue relating to detector nonlinearity arises when low altitude fogs and aerosols are present. These events result in very high backscatter levels at low altitudes as well as high extinction, so backscatter data cannot be retrieved above the fog. In these cases, saturation effects corrupt the feedback signal of the VWP controller. When this happens, the feedback loop controls the profile to cancel the apparent positive diattenuation induced by detector nonlinearity. This effect is most easily seen in Figure 7.9 though the high altitude channel is also subject to this effect. The mean diattenuation profile is shifted by -0.2 due to a saturated feedback loop signal between 00:00 and 06:00 UT. We have attempted to turn off the feedback loop when low altitude clouds that may corrupt the feedback signal are present. However, drift in the VWP phase shift can occur and it is difficult to support findings of oriented scatterers under these conditions. For this reason, diattenuation data is generally ignored when the feedback signals are corrupted by strongly backscattering clouds.

On July 10, 2010, there was substantial cloud cover and precipitation over Summit Camp. The backscatter, diattenuation and linear polarization ratio measurements performed by CAPABL are shown in Figures 7.10, 7.12 and 7.11. Because CAPABL can determine if scatterers are oriented,

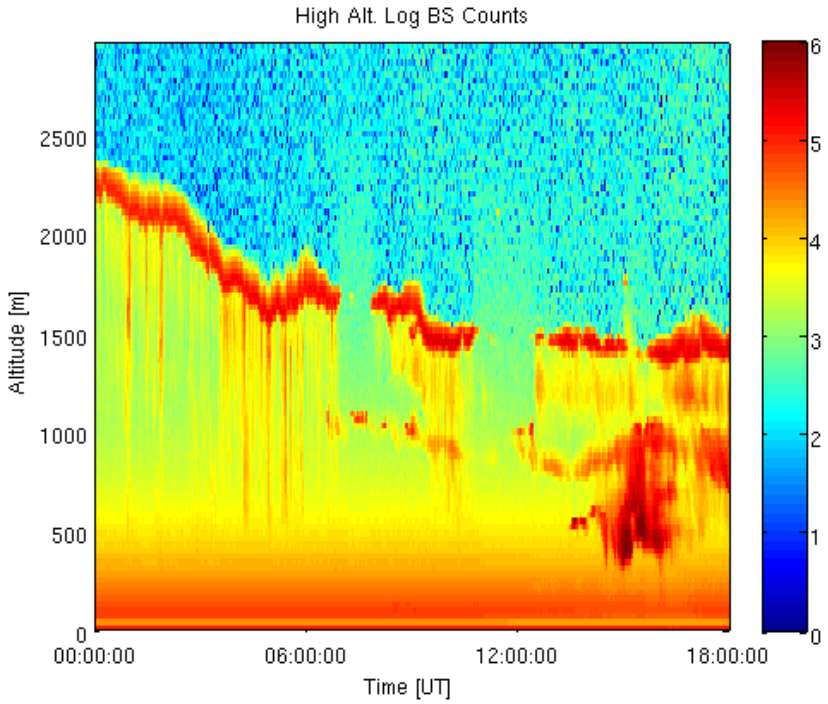

Figure 7.10: Log backscatter profile recorded by CAPABL on July 10, 2010. Clouds are present throughout the day with frequent precipitation.

we can accurately determine the meaning of the parallel and perpendicular signals. Thus, we have a built in check for when it is appropriate to report data as d or the f_{33} matrix element. Since no diattenuation signature is found in the July 10 data, depolarization is reported.

During this dataset collection, the VWP feedback loop is turned off when low altitude clouds are present. This is why diattenuation data drifts off zero between 15:00 and 16:00 UT. This drift does not affect the depolarization estimate since the perpendicular and parallel measurements are not controlled by the feedback loop.

The depolarization data from CAPABL indicates that the clouds above the lidar consist of liquid water due to their low depolarization. However, before 7:00 UT the precipitation below the clouds is strongly depolarizing. It appears that the precipitate is freezing as it falls, then melting back to liquid water below 500 m where it ceases to depolarize. After 7:00 UT, the depolarization signature of the precipitation decreases substantially, suggesting that it remains in liquid phase

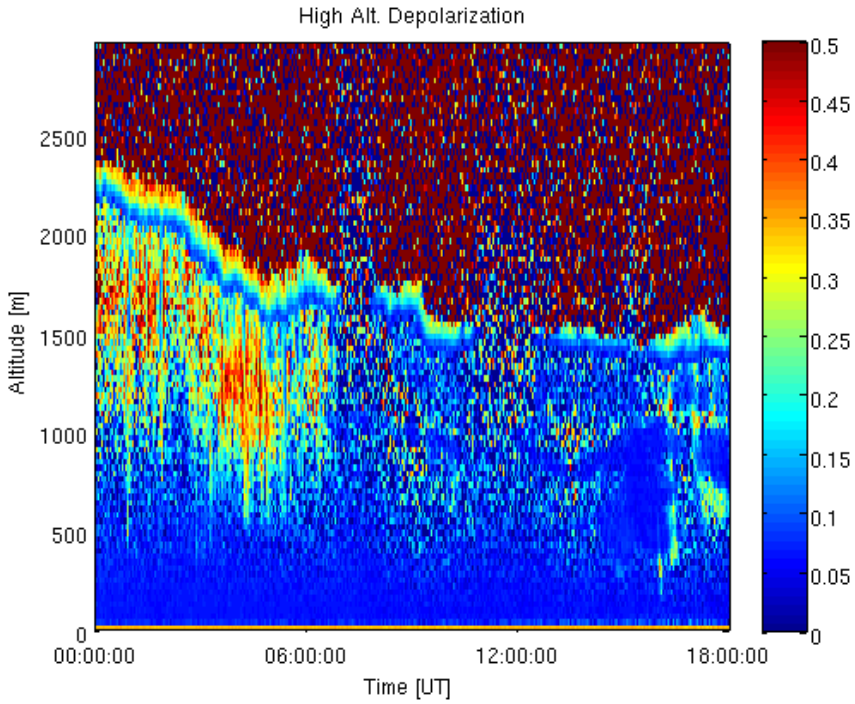

Figure 7.11: Depolarization profile recorded by CAPABL on July 10, 2010. While the clouds are not depolarizing, some precipitation is. This suggests the precipitation may be freezing as it falls.

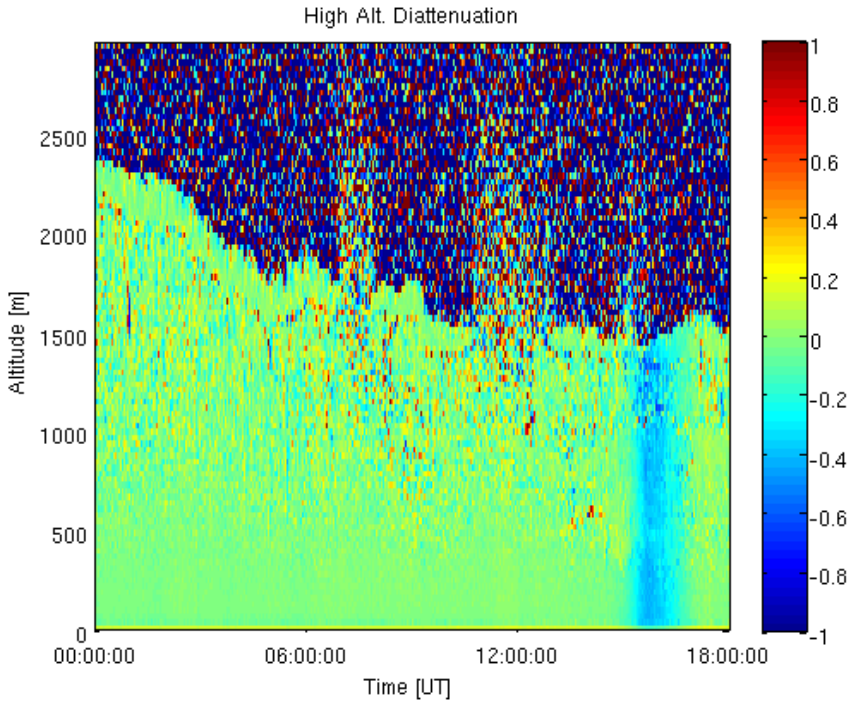

Figure 7.12: Diattenuation profile recorded by CAPABL on July 10, 2010. Because the diattenuation signatures of the clouds are zero, we can reliably assume their scattering matrices are depolarizing. Between approximately 16:00 and 17:00 UT the feedback loop for the VWP is turned off due to low altitude cloud presence.

throughout its fall.

7.4 Detection of Horizontally Oriented Ice Crystals

Over the course of the past year, we have been able to establish the necessary conditions to reliably measure diattenuation with CAPABL, ensuring confidence that detection of a non-zero diattenuation signature is attributable to oriented scatterers. On April 23, 2011, CAPABL was tilted 11° off zenith and a HWP was added to above the last steering mirror in the transmitter. The selected tilt angle coincides with the maximum diattenuation resolution determined by the system simulation using P45P in Chapter 4. The HWP was used to rotate the outgoing linear polarization angle to $\phi_f = \frac{\pi}{4}$.

After tilting the lidar, we were able to identify several non-oriented scattering occurrences. Depolarizing clouds and precipitation and non-depolarizing clouds were observed without diattenuation signatures (see Figure 7.13). However, on several days in early May we also observed events not previously seen when the lidar was pointing along zenith.

On May 7, 2011, CAPABL observed a diattenuation signature that appeared to coincide with a cloud at an altitude of 500 m (see Figures 7.14 and 7.15 for time integrated backscatter and diattenuation and $1-f'_{33}$ profiles respectively). During that same time, a higher altitude cloud with no diattenuation, low depolarization and stronger backscatter (presumably a liquid water cloud) was observed at an altitude of 700 m. Also, persistent depolarizing ice precipitation was observed by the instrument below this 700 m cloud. The occurrence of ice precipitation from liquid clouds has been observed by CAPABL many times above Summit including the data shown in Figures 7.10, 7.12 and 7.11 from July 10, 2010 in the previous section.

At 500 m, corresponding to the diattenuating cloud layer, $1 - f'_{33}$ distinctively approaches 0 which suggests a decrease in depolarization ($f'_{33} = d - 1$ in the presence of nondiattenuating scatterers) and low retardance. There are two facts supporting that the cloud diattenuation is not caused by the detector nonlinearity previously responsible for false diattenuation signatures. First, the depolarization calculations contain the stronger parallel signal in the denominator. If

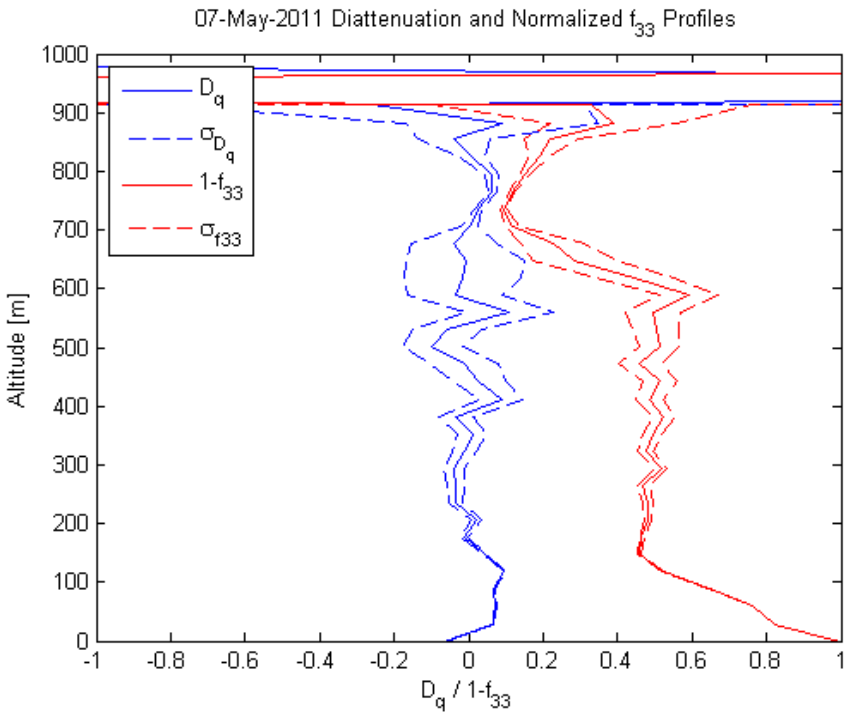

Figure 7.13: Collected polarization data of a nondepolarizing cloud at an altitude of 700 m with depolarizing precipitation below it. No diattenuation signatures are recorded for cloud or precipitation.

detector nonlinearity is occurring, this would cause the denominator to be smaller than its actual value and result in increased depolarization and $1 - f'_{33}$ estimates. The fact that the $1 - f'_{33}$ profile approaches 0 where diattenuation is observed presents a circumstantial argument in favor of actual atmospheric diattenuation because this behavior is counter to that expected due to detector nonlinearity. Second, we observe some detector nonlinearity in the diattenuation profiles below 200 m and the cloud at 700 m. Both have photon count arrival rates higher than that observed in the cloud at 500 m but neither produces a diattenuation signature as large as that observed at 500 m. Thus it is unlikely that detector nonlinearity is responsible for the diattenuation signature observed at 500 m on May 7. The profiles described and shown here where integrated between the times of 18:40 and 18:53 UT.

Unfortunately, the low altitude channel has not been operating properly since tilting the lidar instrument, so we cannot compare diattenuation measurements from the two channels to further validate this measurement.

This early data suggests that CAPABL can detect horizontally oriented ice crystals using their unique polarization signatures. A successful campaign detecting oriented scatterers may have broad implications. Diattenuation measurement enables lidar systems to detect oriented scatterers within the same dynamic range as other aerosols. This may make collection of data on oriented scatterers more prevalent and finally allow for comprehensive climatological studies on this subject.

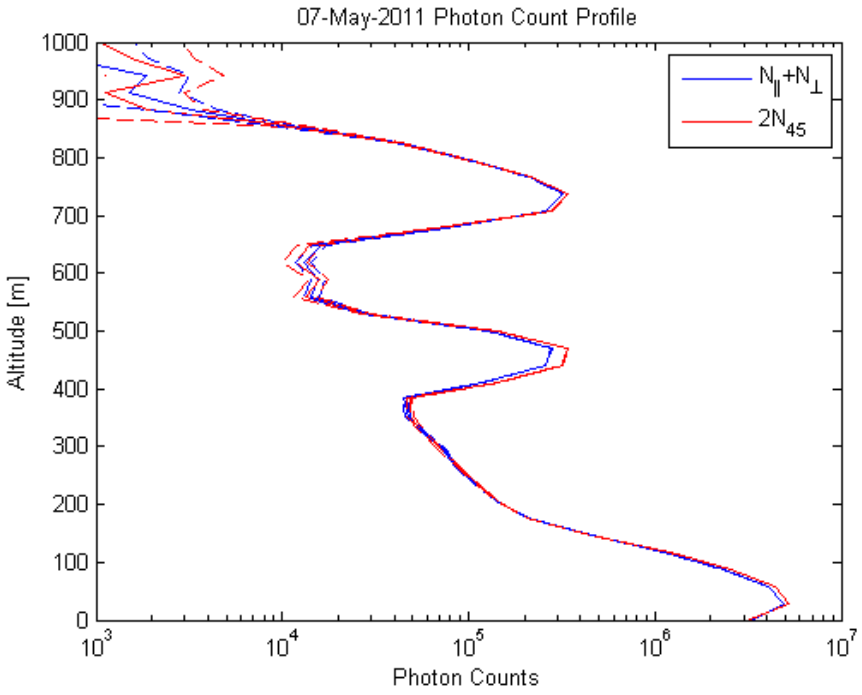

Figure 7.14: Backscatter profiles from May 7, 2011 integrated from 18:40-18:53 UT. The backscatter profiles are presented as the sum of the perpendicular and parallel channels, which is the total backscattered photons, and 2× the 45° channel. If no diattenuation is present, the two profiles should be equal. Also included is the shot noise error of the measurements. Two clouds are observed at 500 and 700 m with precipitation below 700 m. The cloud at 700 m has no diattenuation signature and low depolarization suggesting it is composed of liquid water. The precipitation below the cloud has no diattenuation signature but is strongly depolarizing suggesting it is ice precipitation. The second cloud at 500 m has a strong diattenuation signature and low $1 - f'_{33}$, suggesting it may be composed of oriented ice crystals. Note that the cloud at 700 m has slightly higher backscatter than that at 500 m and the low altitude returns at 190 m are approximately an order of magnitude greater than the diattenuating cloud. If detector nonlinearity were responsible for the signature at 500 m, the measured diattenuation at the layers of higher signal should be even greater.

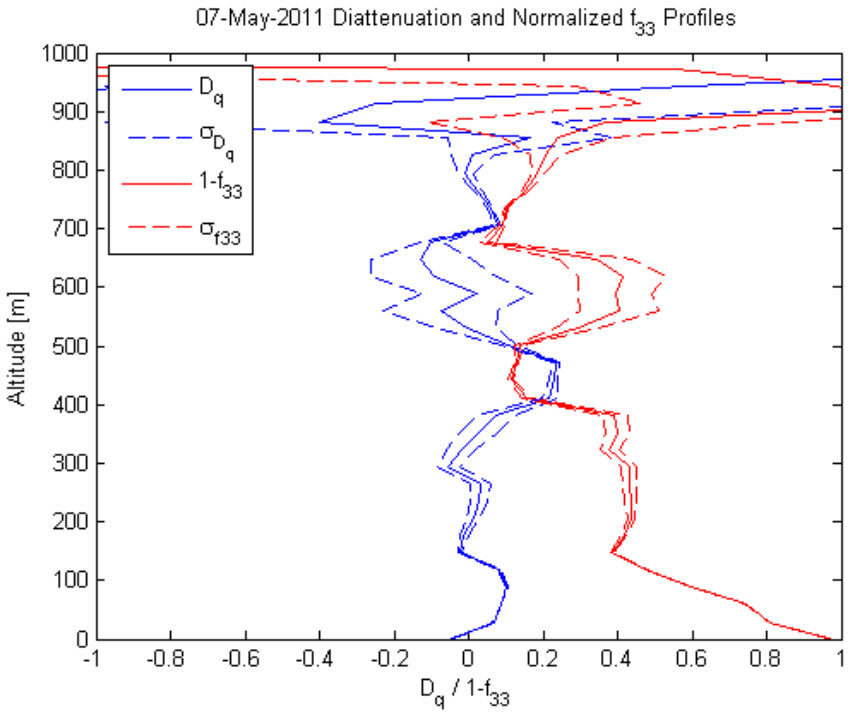

Figure 7.15: Diattenuation and normalized $1 - f'_{33}$ profiles from May 7, 2011 integrated from 18:40-18:53 UT (same data as in 7.14). When no diattenuation is observed, $1 - f'_{33} = d$, thus giving depolarization except where the diattenuating cloud is present. Note the reduction in $1 - f'_{33}$ observed at approximately the same altitude as the diattenuation signature.

Chapter 8

Conclusion

In my graduate work I have shown that a Mueller matrix approach to polarization lidar provides a comprehensive description of all terms along the optical path and improved clarity for the measured polarization quantities. While the scalar equations often used to describe polarization lidar cannot fully account for polarization effects in the optical system, a Mueller matrix approach allows for a complete understanding of how system retardance, diattenuation and depolarization impact polarization and backscatter measurements. Thus through Mueller analysis, error contributions of these optical system effects can often be mitigated or avoided.

Current polarization lidar theory assumes the lidar measures only perpendicular and parallel polarizations relative to the original transmit polarizations. This this limits the development of new measurement techniques that may be better suited to a particular sensing objective, such as identification of horizontally oriented ice crystals.

It is not clear how conventional polarization scattering descriptions $\beta_\perp$ and $\beta_\parallel$ relate to scattering theory which uses a sixteen element phase matrix for polarization descriptions. As a result, the data product commonly used to describe polarization results, the polarization ratio δ, is not uniquely related to the phase matrix of an arbitrary scatterer. When scatterers are randomly oriented and axially symmetric, we can fairly easily assume the scattering matrix form. However, in some cases, such as oriented ice crystals, it is unclear what matrix terms are contributing to the measured polarization ratio. In such a case, the data product is a function of the incident polarization. This means that two lidars interrogating the same scattering volume could measure

different polarization ratios if they do not use the same polarizations.

As part of my graduate work I have developed the Stokes Vector Lidar Equation (SVLE), which is a fully general polarimetric description of polarization lidar. Through this theoretical development I have been able to perform a full error analysis on all polarization sensing techniques used in this work. This general approach to polarization error has helped us identify particular cases of atmospheric scattering that may be problematic for our instruments. It also allows us to ensure that data is recorded to properly check the instrument performance. In CAPABL, we record the data used by the feedback loop to control the variable wave plate. This allows us to check the polarization performance of the instrument, rather than blindly assume all recorded data is accurate.

Using the SVLE, I also developed error mitigation techniques. I developed a general technique for canceling retardance in an optical system using a compensator consisting of two quarter wave plates (QWP). However, implementation of this technique often proved to be time consuming because the full system Mueller matrix had to be measured to correctly configure the compensator. I was able to make implementation of compensation significantly easier by developing a laboratory technique to set the QWP angles in the compensator without ever measuring the optical system Mueller matrix. That compensation optimization technique was subsequently used to cancel retardance in ARCLITE's transmitter and receiver.

Though I was able to cancel ARCLITE's retarding effects, depolarization in the receiver still presented a significant problem for polarization measurements. However, again aided by the SVLE, I was able to develop a software correction technique that drastically improved the accuracy of ARCLITE's polarization measurements. This software correction was able to remove a number of polarization effects from ARCLITE's measurements including retardance in the receiver, depolarization in the transmitter and receiver, and misalignment of the transmitter and receiver polarization planes. While this software correction is confined only to scattering cases where the volume consists of randomly oriented axially symmetric particles, we find this is generally the case for ARCLITE measurements.

The scattering matrix of oriented ice crystals do not conform to the same simple form exhibited by their randomly oriented counter parts. Never-the-less, almost every polarization measurement performed on oriented scatterers is that of the polarization ratio, which offers little distinction between randomly oriented and oriented ice crystals. Using the SVLE, I was able to incorporate full scattering descriptions of oriented ice crystals and give full consideration to how we can use polarization to identify them. The distinguishing characteristic in oriented scattering matrices is the presence of nonzero off diagonal terms. To identify these terms however, it became quite obvious that a different kind of polarization lidar would be needed. By applying the SVLE to this scattering problem, I designed a new polarization measurement for the diattenuating properties of the scatterer.

To perform this measurement I developed two techniques. The Parallel-45-Perpendicular (P45P) technique was used in CAPABL and allowed the instrument to still measure the conventional parallel and perpendicular polarizations. However the addition of a 45° polarization measurement also allows the lidar to measure the (1,2) diattenuation element of the scattering matrix.

The Alternating Cross Polarized (ACP) technique measures only the (1,2) element of the scattering matrix. However it has the benefit of being insensitive to retarding and depolarizing effects in the lidar receiver, because it does not use an analyzer. Thus the ACP technique disproves a common misconception that polarization lidar must have a polarizer in the receiver.

Through application of polarization effect mitigation, I applied ARCLITE's high altitude sensing capabilities to the problem of polar mesospheric cloud (PMC) particle shape through depolarization measurements. Unfortunately, even with ARCLITE's substantial transmit power and receiver aperture, the signal-to-noise on all PMC detections was not sufficient to resolve the PMC depolarization. However I was able to contribute further analysis to the necessary modifications for ARCLITE to achieve this objective.

Since its deployment the Cloud Aerosol Polarization and Backscatter Lidar (CAPABL) has been tested for possible issues in oriented scatterer detection. To assess the possible contributers to false positives, CAPABL collected data while pointed only 2° off zenith for a year. In this mode

of operation, horizontally oriented ice crystals (presumably the most common form of oriented ice crystals) would not produce diattenuation signatures. Thus all instances of nonzero diattenuation were investigated to determine their cause. These cases allowed us to either implement solutions to prevent incorrect measurements or ignore instances where CAPABL does not have established accuracy. On April 23, 2011, CAPABL was tilted 11° off zenith to begin a campaign to look for oriented ice crystals. In early May, a number of promising profiles were observed.

Since until now, this diattenuation measurement has never performed, we did not previously know if the selected tilt angle would be sufficient for detecting horizontally oriented ice crystals. Also, given the possibility that oriented ice crystals are diluted by randomly oriented crystals, we did not know if the instrument would have sufficient resolution to detect any diattenuating signatures at any tilt angle. The diattenuation profiles measured by CAPABL in May appear to vindicate this approach to detecting oriented ice crystals. This may help to establish the Stokes Vector Lidar Equation as a theoretical standard for polarization lidar, by demonstrating the power of full polarization optical theory when applied to atmospheric remote sensing.

Bibliography

[1] H. Adachi. Calibration method for the lidar-observed stratospheric depolarization ratio in the presence of liquid aerosol particles. Appl. Opt., 40:6587–6595, 2001.

[2] J. M. Alvarez. Calibration technique for polarization-sensitive lidars. J. Atmos. Ocean. Technol., 23:683–699, 2006.

[3] A. Ansmann, M. Riebesell, and C. Weitkamp. Measurement of atmospheric aerosol extinction profiles with a raman lidar. Opt. Lett., 15:746–748, 1990.

[4] V. Bagini et al. The simon-mukunda polarization gadget. Eur. J. Phys., 17:279–284, 1996.

[5] Y. Balin, B. V. Kaul, G. Kokhanenko, and D. M. Winker. Application of circularly polarized laser radiation for sensing of crystal clouds. Opt. Express, 17(8):6849–6859, 2009.

[6] G. Baumgarten, J. Fiedler, and G. von Cossart. The size of noctilucent cloud particles above alomar (69n,16e): Optical modeling and method description. Adv. in Space Res., 40:772–784, 2007.

[7] G. Baumgarten, K.H. Fricke, and G. von Cossart. Investigation of the shape of noctilucent cloud particles by polarization lidar technique. Geophys. Res. Lett., 29(13):1–4, 2002.

[8] G. Baumgarten and G.E. Thomas. The importance of ice particle shape on uv measurements of polar mesospheric clouds: Sbuv/2 observations. J. Atmos. Sol. Terr. Phys., 68(1):78–84, 2006.

[9] A. Behrendt and T. Nakamura. Calculation of the calibration constant of polarization lidar and its dependency on atmospheric temperature. Opt. Express, 10:805–817, 2002.

[10] G. Beyerle, M. R. Gross, D. A. Haner, N. T. Kjome, I. S. McDermid, T. J. McGee, J. M. Rosen, H. J. Schäfer, and O. Schrems. A lidar and backscatter sonde measurement campaign at table mountain during february–march 1997: Observations of cirrus clouds. J. Atmos. Sci., 58:1275–1287, 2001.

[11] J. Biele et al. Polarization lidar: Corrections of instrumental effects. Opt. Express, 7:427–435, 2000.

[12] L. C. Bissonette. Multiple-scattering lidar equation. Appl. Opt., 35(33):6449–6465, 1996.

[13] C.F. Bohren and D.R. Huffman. Absorption and Scattering of Light by Small Particles. Wiley, 1983.

[14] M. Borne and E. Wolf. Principles of Optics. University, 6th edition, 1999.

[15] B. D. Cameron, M. J. Raković, M. Mehrübeoglu, G. W. Kattawar, S. Rastegar, L. V. Wang, and G. L. Coté. Measurement and calculation of the two-dimensional backscattering mueller matrix of a turbid medium. Opt. Lett., 23(7):485–487, 1998.

[16] A. I. Carswell and S. R. Pal. Polarization anisotropy in lidar multiple scattering from clouds. Appl. Opt., 19:4123, 1980.

[17] H. Chepfer, G. Brogniez, and Y. Fourquart. Cirrus clouds' microphysical properties deduced from polder observations. J. Quant. Spectroc. and Rad. Transfer, 60:375–390, 1998.

[18] R. A. Chipman. Mechanics of polarization ray tracing. Optical Engineering, 34:1636–1645, 1995.

[19] R. A. Chipman. Polarimetry, volume II of Handbook of Optics, chapter 22. McGraw-Hill, 1995.

[20] X. Chu and G. C. Papen. Laser Remote Sensing, chapter 5. Taylor & Francis, 2005.

[21] J. H. Churnside, J. J. Wilson, and V. V. Tatarskii. Lidar profiles of fish schools. Appl. Opt., 36(24):6011–6020, 1997.

[22] S.R. Cloude and E. Pottier. A review of target decomposition theorems in radar polarimetry. IEEE Trans. Geosci. Remote Sens., 34(2):498–518, 1996.

[23] M. N. Eremenko et al. Shape and composition of pmc particles derived from satellite remote sensing measurements. Geophys Res. Lett., 32:L16S06, 2005.

[24] D. W. Fahey et al. In situ measurements of total reactive nitrogen, total water, and aerosols in a polar stratospheric cloud in the antarctic. Geophys. Res. Lett., 94:11299–11316, 1989.

[25] C. J. Flynn, A. Mendoza, Y. Zheng, and S. Mathur. Novel polarization-sensitive micropulse lidar measurement technique. Opt. Express, 15:2785–2790, 2007.

[26] G. Gimmestad. Reexamination of depolarization in lidar measurements. Appl. Opt., 47:3795–3802, 2008.

[27] D. H. Goldstein. Polarized Light. Marcel Dekker, Inc., second edition, 2003.

[28] J. W. Goodman. Introduction to Fourier Optics. Roberts & Company Publishers, third edition, 2005.

[29] W. B. Grant. Differential absorption and raman lidar for water-vapor profile measurements: a review. Opt. Eng., 30:40–48, 1991.

[30] C. J. Grund and E. W. Eloranta. The university of wisconsin high spectral resolution lidar. Optical Engineering, 30:6–12, 1991.

[31] M. Del Gusta, E. Vallar, O. Riviere, F. Castagnoli, V. Venturi, and M. Morandi. Use of polarimetric lidar for the study of oriented ice plates in clouds. Appl. Opt., 45(20):4878–4887, 2006.

[32] M. Hayman and J.P. Thayer. Explicit description of polarization coupling in lidar applications. Opt. Lett., 34(5):611–613, 2009.

[33] M. Hayman and J.P. Thayer. Lidar polarization measurements of pmcs. J. Atmos. Sol. Terr. Phys., 2010.

[34] M. Hervig, R.E. Thompson, M. McHugh, L.L. Gordley, J.M. Russel III, and M.E. Summers. First confirmation that water ice is the primary component of polar mesospheric clouds. Geophys. Res. Lett., 28(6):971–974, 2001.

[35] W. H. Hunt, D. M. Winker, M. A. Vaughan, K. A. Powell, P. L. Lucker, and C. Weimer. Caplipso lidar description and performance assessment. J. Atmos. Oceanic Technol., 26:1214–1228, 2009.

[36] R. B. Husar, J. M. Prospero, and L. L. Stowe. Characterization of tropospheric aerosols over the oceans with the noaa advanced very high resolution radiometer optical thickness operational product. J. Geophys. Res., 102:16889–16909, 1997.

[37] K. Isono, M. Komabayasi, and A. Ono. The nature and origin of ice nuclei in the atmosphere. J. Meteorol. Soc. Japan, 37:211–233, 1959.

[38] B. V. Kaul. Lidar equation for the case of sensing optically anisotropic media. In EUROPTO Conference on Satellite Remonte Sensing of Clouds and the Atmosphere, volume 3495 of SPIE, pages 332–339, September 1998.

[39] B. V. Kaul, I. V. Samokhvalov, and S. N. Volkov. Investigating particle orientation in cirrus clouds by measuring backscattering phase matrices with lidar. Appl. Opt., 43:6620–6628, 2004.

[40] J. D. Klett. Lidar inversion with variable backscatter/extinction ratios. Appl. Opt., 24(11):1638–1643, 1985.

[41] Q. Liu and F. Weng. A microwave polarimetric two-stream radiative transfer model. J. Atmos. Sci., 59:2396–2402, 2002.

[42] S. Y. Lu and R. A. Chipman. Interpretation of mueller matrices based on polar decomposition. J. Opt. Soc. Am. A, 13(5):1106–1113, 1996.

[43] I. Mattis, M. Tesche, M. Grein, V. Freudenthaler, and D. Müller. Systematic error of lidar profiles caused by a polarization-dependent receiver transmission: quantification and error correction scheme. Appl. Opt., 48(14):2742–2751, 2009.

[44] G. G. Matvienko, I. V. Samokhvalov, and B. V. Kaul. Research of the cirrus structure with a polarization lidar: parameters of particle orientation in crystal clouds. In Remote Sensing of Clouds and the Atmosphere, volume 5571 of SPIE, 2004.

[45] S. D. Mayor, S. M. Spuler, and B. M. Morley. Scanning eye-safe depolarization lidar at 1.54 microns and potential usefulness in bioaerosol plume detection. In Lidar Remote Sensing for Environmental Monitoring IV, SPIE, 2005.

[46] M. J. McGill, D. L. Hlavka, W. D. Hart, J. D. Spinhirne, V. S. Scott, and B. Schmid. The cloud physics lidar: Instrument description and initial measurement results. Appl. Opt., 41:3725–3734, 2002.

[47] R. M. Measures. Laser Remote Sensing Fundamentals and Applications. Wiley & Sons, Inc., 1984.

[48] T. P. Miller and T. J. Casadevall. Volcanic ash hazards to aviation, pages 915–930. Ecyclopedia of Volcanoes. Elsevier, 2000.

[49] M.I. Mishchenko. Light scattering by randomly oriented axially symmetric particles. J. Opt. Soc. Am. A, 8(6):871–882, 1991.

[50] M.I. Mishchenko and J.W. Hovenier. Depolarization of light backscattered by randomly oriented nonspherical particles. Opt. Lett., 20:1356–1358, 1995.

[51] M.I. Mishchenko and L.D. Travis. Capabilities and limitations of a current fortran implementation of the t-matrix method for randomly oriented, rotationally symetric scatterers. J. Quant. Spectrosc. Radiat. Transfer, 60:309–324, 1998.

[52] M.I. Mishchenko, L.D. Travis, and A. Macke. Light Scattering by Nonspherical Particles, chapter 6, pages 147–172. Academic, 2000.

[53] S. Mitchell, J. P. Thayer, and M. Hayman. Polarization lidar for shallow water depth measurement. Appl. Opt., 49(36):6995–7000, 2010.

[54] V. Noel and H. Chepfer. Study of ice crystal orientation in cirrus clouds based on satellite polarized radiance measurements. J. Atmos. Sci., 61:2073–2081, 2004.

[55] V. Noel and H. Chepfer. A global view of horizontally oriented crystals in ice clouds from cloud-aerosol lidar and infrared pathfinder satellite observation (calipso). J. Geophys. Res., 115, 2010.

[56] V. Noel and K. Sassen. Study of planar ice crystal orientations in ice clouds from scanning polarization lidar observations. J. Appl. Meteor., 44:653–664, 2005.

[57] O. Okada, J. Heintzenberg, K. Kai, and Y. Qin. Shape of atmospheric mineral particles collected in three chinese arid-regions. Geophys Res. Lett., 28:3123–3126, 2001.

[58] S. R. Pal and A. I. Carswell. Polarization anisotropy in lidar multiple scattering from atmospheric clouds. Appl. Opt., 24(21):3464–3471, 1985.

[59] J.M. Plane, B.J. Murray, X. Chu, and C.S. Gardner. Removal of meteoric iorn on polar mesospheric clouds. Science, 304:426–428, 2004.

[60] L. R. Poole et al. Lidar observations of arctic polar stratospheric clouds. Geophys. Res. Lett., 15:867–870, 1988.

[61] S. Raizada, M. Rapp, F.-J. Lübken, J. Höffner, M. Zecha, and J.M. Plane. The effect of ice particles on the mesospheric potassium laer at spitsbergen ($78°n$). J. Geophys. Res., 112, 2007.

[62] M. J. Raković and G. W. Kattawar. Theoretical analysis of polarization patterns from incoherent backscattering of light. Appl. Opt., 37(15):3333–3338, 1998.

[63] M. Rapp et al. Spectral properties of mesospheric ice clouds: Evidence for nonspherical particles. J. Geophys. Res., 112, 2007.

[64] G. C. Reid. Ice clouds at the summer polar mesopause. Atmos. Sci., 25:523–535, 1975.

[65] G. Roy, L. Bissonette, C. Bastille, and G. Vallée. Retrieval of droplet-size density distribution from multiple-field-of-view cross-polarized lidar signals: theory and experimental validation. Appl. Opt., 38(24):5202–5211, 1999.

[66] F Roy-Brehonnet and B. Jeune. Utilization of mueller matrix formalism to obtain optical targets depolarization and polarization properties. Prog. Quant. Electr, 21(2):109–151, 1997.

[67] D. Rusch, G.E. Thomas, and E.J. Jensen. Particle size distributions in polar mesospheric clouds derived from solar mesosphere explorer measurements. J. Geophys. Res., 96(D7):12933–12929, 1991.

[68] P. B. Russell, T.J. Swissler, and M. P. McCormick. Methodology for error analysis and simulation of lidar aerosol measurements. Appl. Opt., 18:3783–3797, 1979.

[69] K. Sassen. Polarization diversity lidar retums from virga and precipitation: Anomalies and the bright band analogy. J. Appl. Meteor., 15:292–300, 1976.

[70] K. Sassen. The polarization lidar technique for cloud research: a review and current assessment. Bull. Am. Meteorol. Soc., 72:1848–1866, 1991.

[71] K. Sassen. Lidar: Range-Resolved Optical Remote Sensing of the Atmosphere, chapter Polarization in Lidar, pages 19–42. Springer, 2005.

[72] K. Sassen and S. Benson. A midlatitude cirrus cloud climatology from the facility for atmospheric remote sensing. part ii: Microphysical properties derived from lidar depolarization. J. Atmos. Sci., 58:2103–2111, 2001.

[73] K. Sassen, P. J. DeMott, J. M. Prospero, and M. R. Poellot. Saharan dust storms and indirect aerosol effects on clouds: Crystal-face results. Geophys Res. Lett., 30(12), 2003.

[74] K. Sassen, Z. Jiang, P. Webley, K. Dean, and P. Cobb. Volcanic ash plume identification using polarization lidar: Augustine eruption, alaska. Geophys. Res. Lett., 34, 2007.

[75] L. Sauvage, H. Chepfer, V. Trouillet, P. H. Flamant, G. Brogniez, J. Pelon, and F. Albers. Remote sensing of cirrus radiative parameters during eucrex94. case study of 17 april 1994. part i: Observations. Mon. Wea. Rev., 127:486–503, 1999.

[76] R. M. Schotland, K. Sassen, and R. J. Stone. Observations by lidar of linear depolarization ratios by hydrometeors. J. Appl. Meteor., 10:1011–1017, 1971.

[77] N. L. Seldomridge, J. A. Shaw, and K. S. Repasky. Dual-polarization lidar using a liquid crystal variable retarder. Optical Engineering, 45(10), 2006.

[78] J. A. Shaw, N. L. Seldomridge, D. L. Dunkle, P. W. Nugent, L. H. Spangler, J. J. Bromenshenk, C. B. Henderson, J. H. Churnside, and J. J. Wilson. Polarization lidar measurements of honey bees in flight for locating land mines. Opt. Express, 13(15):5853–5863, 2005.

[79] C. Y She and J. R. Yu. Simultaneous threefrequency na lidar measurements of radial wind and temperature in the mesopause region. Geophys Res. Lett., 21(17):1771–1774, 1994.

[80] S. T. Shipley, D. H. Tracy, E. W. Eloranta, J. T. Trauger, J. T. Sroga, F. L. Roesler, and J. A. Weinman. A high spectral resolution lidar to measure optical scattering properties of atmospheric aerosols, part i: Instrumentation and theory. Appl. Opt., 23:3716–3724, 1983.

[81] R. Simon. Nondepolarizing systems and degree of polarization. Opt. Comm., 77:349–354, 1990.

[82] R. Simon and N. Mukunda. Minimal three-component su(2) gadget for polarization optics. Phys. Lett. A, 143:165–169, 1990.

[83] Y. Takano and K. N. Liou. Solar radiative transfer in cirrus clouds. part i: Single-scattering and optical properties of hexagonal ice crystals. J. Atmos. Sci., 46:3–19, 1989.

[84] J. P. Thayer et al. Gravity-wave influences on arctic mesospheric clouds as determined by a rayleigh lidar at sondrestrom, greenland. J. Geophys. Res., 108:8449, 2003.

[85] G.E. Thomas and C.P. McKay. On the mean particle size and water content of the polar mesospheric clouds. Planet. Space Sci., 33:1209–1224, 1985.

[86] O. B. Toon, E. V. Browell, S. Kinne, and J. Jordan. An analysis of lidar observations of polar stratospheric clouds. Geophys. Res. Lett., 17(4):393–396, 1990.

[87] H.C. van de Hulst. Light Scattering by Small Particles. Wiley, 1981.

[88] D.A. Varshalovich, A.N. Moskalev, and V.K. Khersonskii. Quantum Theory of Angular Momentum. World Scientific, 1988.

[89] G. von Cossart, J. Fiedler, and U. von Zahn. Size distributions of nlc particles as determined from 3-color observations of nlc by ground-based lidar. Geophys. Res. Lett., 26(11):1513–1516, 1999.

[90] U. von Zahn and U. Berger. Persistent ice cloud in the midsumer upper mesosphere at high latitudes: Three-dimensional modeling and cloud interactions with ambient water vapor. J. Geophys. Res., 108(D8):8451, 2003.

[91] S.G. Warren. Optical constants of ice from the ultraviolet to the microwave. Appl. Opt., 23(8):1206–1225, 1984.

[92] P. Yang and K.N. Liou. Geometric-optics-integral-equation method for light scattering by nonspherical ice crystals. Appl. Opt., 35(33):6568–6584, 1996.

[93] A. Yariv and P. Yeh. Photonics: Optical Electronics in Modern Communications. Oxford, 2007.

Appendix A

T-Matrix Function Definitions

Function definitions of for VWSF in T-matrix calculations[52]:

$$\mathbf{M}_{mn}(k\mathbf{R}) = (-1)^m d_n h_n^{(1)}(kR)\mathbf{C}_{mn}(\vartheta)\exp(im\varphi) \tag{A.1}$$

$$\mathbf{N}_{mn}(k\mathbf{R}) = (-1)^m d_n \left\{ \frac{n(n+1)}{kR} h_n^{(1)}(kR)\mathbf{P}_{mn}(\vartheta) + \frac{1}{kR}\left[kRh_n^{(1)}(kR)\right]' \mathbf{B}_{mn}(\vartheta) \right\} \exp(im\varphi) \tag{A.2}$$

$$\mathbf{B}_{mn}(\vartheta) = \boldsymbol{\vartheta}\frac{d}{d\vartheta} d_{0m}^n(\vartheta) + \boldsymbol{\varphi}\frac{im}{sin\vartheta} d_{0m}^n(\vartheta) \tag{A.3}$$

$$\mathbf{C}_{mn}(\vartheta) = \boldsymbol{\vartheta}\frac{im}{\sin\vartheta} d_{0m}^n(\vartheta) - \boldsymbol{\varphi}\frac{d}{d\vartheta} d_{0m}^n(\vartheta) \tag{A.4}$$

$$\mathbf{P}_{mn}(\vartheta) = \mathbf{R}\frac{d_{0m}^n(\vartheta)}{R} \tag{A.5}$$

$$d_n = \left[\frac{2n+1}{4\pi n(n+1)}\right]. \tag{A.6}$$

$h_n^{(1)}$ is the spherical Hankel function.

$\mathbf{R}$ is the coordinate of observation in the particle coordinate frame.

R is the distance from the origin in the particle coordinate frame.

k is the incident wave number.

ϑ is the zenith angle of observation in the particle coordinate frame.

$\boldsymbol{\vartheta}$ is zenith angle unit vector.

φ is the azmuthal angle of observation in the particle coordinate frame.

$\boldsymbol{\varphi}$ is the azmuthal angle unit vector.

Wigner d amd D functions definitions[88].

$$\begin{aligned} d^n_{lm}(\vartheta) &= A^n_{lm}(1-\cos\vartheta)^{(l-m)/2}(1+\cos\vartheta)^{-(l+m)/2} \\ &\times \frac{d^{n-m}}{(d\cos\vartheta)^{n-m}}[(1-\cos\vartheta)^{n-l}(1+\cos\vartheta)^{n+l}] \end{aligned} \tag{A.7}$$

$$A^n_{lm} = \frac{(-1)^{n-m}}{2^n}\left[\frac{(n+m)!}{(n-l)!(n+1)!(n-m)!}\right]^{1/2} \tag{A.8}$$

$$D^n_{m'm}(\alpha,\beta,\gamma) = \exp(-im'\alpha)d^n_{m'm}(\beta)\exp(-im\gamma). \tag{A.9}$$